Intracellular mechanisms of fungal space searching in microenvironments

Marie Held[a], Ondřej Kašpar[b,c], Clive Edwards[d], and Dan V. Nicolau[a,b,1]

[a]Department of Electrical Engineering and Electronics, University of Liverpool, L69 3GJ Liverpool, United Kingdom; [b]Department of Bioengineering, Faculty of Engineering, McGill University, Montreal, QC H3A 0C3, Canada; [c]Department of Chemical Engineering, University of Chemistry and Technology, Prague, Prague 166 28, Czech Republic; and [d]School of Biological Sciences, University of Liverpool, L69 7ZB Liverpool, United Kingdom

Edited by David A. Weitz, Harvard University, Cambridge, MA, and approved May 21, 2019 (received for review September 21, 2018)

Filamentous fungi that colonize microenvironments, such as animal or plant tissue or soil, must find optimal paths through their habitat, but the biological basis for negotiating growth in constrained environments is unknown. We used time-lapse live-cell imaging of *Neurospora crassa* in microfluidic environments to show how constraining geometries determine the intracellular processes responsible for fungal growth. We found that, if a hypha made contact with obstacles at acute angles, the Spitzenkörper (an assembly of vesicles) moved from the center of the apical dome closer to the obstacle, thus functioning as an internal gyroscope, which preserved the information regarding the initial growth direction. Additionally, the off-axis trajectory of the Spitzenkörper was tracked by microtubules exhibiting "cutting corner" patterns. By contrast, if a hypha made contact with an obstacle at near-orthogonal incidence, the directional memory was lost, due to the temporary collapse of the Spitzenkörper–microtubule system, followed by the formation of two "daughter" hyphae growing in opposite directions along the contour of the obstacle. Finally, a hypha passing a lateral opening in constraining channels continued to grow unperturbed, but a daughter hypha gradually branched into the opening and formed its own Spitzenkörper–microtubule system. These observations suggest that the Spitzenkörper–microtubule system is responsible for efficient space partitioning in microenvironments, but, in its absence during constraint-induced apical splitting and lateral branching, the directional memory is lost, and growth is driven solely by the isotropic turgor pressure. These results further our understanding of fungal growth in microenvironments relevant to environmental, industrial, and medical applications.

fungal growth | Spitzenkörper | microtubules | live-cell imaging | microfluidics

Filamentous fungi dwell in geometrically, mechanically, and materially heterogeneous habitats, such as animal or plant tissue (1, 2), decaying wood, leaf litter, and soil (3, 4). The ecological ubiquity of filamentous fungi stems, to a large extent, from their remarkable ability to invade, search for nutrients, and thrive within these microenvironments. Because filaments (hyphae) can grow for relatively long distances (millimeters) through media containing no, or low, levels of nutrients, fungal space-searching strategies need to operate independently of chemotaxis (5, 6).

Extensive studies have described the fundamental growth behavior of fungi: For example, hyphal directional growth (7–11), regular branching (12–14), and negative autotropism (15, 16). However, these studies have been performed on flat agar surfaces, in contrast to the 3D, geometrically constrained habitats filamentous fungi naturally encounter.

Advanced fluorescence microscopy studies of fungal growth on nonconstraining open surfaces have revealed several intracellular processes that are essential for hyphal extension and branching (9, 17, 18). First, the positioning of the Spitzenkörper at the hyphal apex correlates with the direction of apical growth and overall cell polarization (19–24). Second, cytoskeleton dynamics (involving microtubules, actin, and motor proteins) mediate the directional, long-distance transport of secretory vesicles from the body of the fungus toward the hyphal apex, carrying materials for building the hyphal cell wall. Whereas microtubule dynamics in fungal growth have been extensively studied (25–30), our understanding of the role of actin filaments is less developed and more recent (31–36). Third, the dynamic process of constructing hyphal walls results in an increase in stiffness from the apex to the base of hyphae (25, 28, 30, 37–40). Finally, concentration gradients of osmolytes (e.g., ions, sugars, and alcohols) (41) along the hypha and between the hyphal cytoplasm and the outside environment produce considerable turgor pressure, which provides a distributed internal driving force for fungal growth that is manifested primarily at the hyphal tip and which enables the fungus to penetrate soft obstacles (17, 42–47).

Microfluidics devices, which have been used to study the behavior of individual bacterial (48–50), mammalian (51, 52), and plant cells (53, 54), and recently fungi (55–57), can be designed to mimic micrometer-sized, naturally constraining habitats. Furthermore, the material of choice for these devices, poly(dimethylsiloxane) (PDMS) (58), is transparent, allowing visualization by microscopy (52, 59), and is permeable to O_2, allowing in vitro studies in more realistic conditions.

Using advanced microfluidics technology, our previous studies (60–62) with the fungi *Pycnoporus cinnabarinus* and *Neurospora crassa* demonstrated differences in behavior in constraining geometries compared with that on flat surfaces; in particular, fungi grown in a geometrically constrained environment had up to 10 times lower apical extension rates and distances between branches. Translation of the fungal space-searching process into a mathematical formalism (60, 63) revealed that this strategy is analogous to a "master program"

Significance

Many filamentous fungi colonizing animal or plant tissue, waste matter, or soil must find optimal paths through the constraining geometries of their microenvironment. Imaging of live fungal growth in custom-built microfluidics structures revealed the intracellular mechanisms responsible for this remarkable efficiency. In meandering channels, the Spitzenkörper (an assembly of vesicles at the filament tip) acted like a natural gyroscope, conserving the directional memory of growth, while the fungal cytoskeleton organized along the shortest growth path. However, if an obstacle could not be negotiated, the directional memory was lost due to the disappearance of the Spitzenkörper gyroscope. This study can impact diverse environmental, industrial, and medical applications, from fungal pathogenicity in plants and animals to biology-inspired computation.

Author contributions: M.H. and D.V.N. designed research; M.H. and D.V.N. performed research; C.E. contributed new reagents/analytic tools; M.H., O.K., C.E., and D.V.N. analyzed data; and M.H. and D.V.N. wrote the paper.

The authors declare no conflict of interest.

This article is a PNAS Direct Submission.

[1]To whom correspondence may be addressed. Email: dan.nicolau@mcgill.ca.

This article contains supporting information online at www.pnas.org/lookup/suppl/doi:10.1073/pnas.1816423116/-/DCSupplemental.

Published online June 18, 2019.

with two "slave subroutines": Directional memory, whereby individual hyphae return to their initial direction of growth after passing an obstacle that forced them to deviate from their course; and obstacle-induced branching, whereby branching occurs only if the hypha encounters an obstacle that totally blocks its growth. "Running" this program results in a significantly deeper exploration of the available space for growth than other possible alternatives (60, 61): That is, turning off either directional memory, obstacle-induced branching, or both subroutines. It was also shown that the fungal space-searching program can find exits in confining mazes quicker than some mathematical algorithms (63). However, these empirical studies do not offer insights into the "hard-wired" intracellular mechanisms underlying the strategy adopted by fungi for efficient searching of their constraining environment.

The roles of the Spitzenkörper, microtubules, and turgor pressure in fungal growth have been studied comprehensively—but only in nonconstraining environments. As the growth behavior of fungi differs considerably between nonconstraining and constraining environments, our present understanding requires refinement. To elucidate containment-induced intracellular processes in fungi, and particularly their role in directional memory and obstacle-induced branching, we used time-lapse laser-scanning confocal microscopy to image the growth of *N. crassa* and the dynamics of fluorescently labeled Spitzenkörper and microtubules in confining microfluidics networks. The results are potentially relevant to various environmental, industrial, and medical concerns, including fungal pathogenicity.

Results

Fungal Growth on Flat Agar Surfaces and in Closed Nonconstraining PDMS Geometries. Because the vast majority of reported fungal growth studies have been performed on open agar surfaces, the first step in our study was to establish that the "internal" control in our experiments (that is, using closed, but nonconstraining, large PDMS-made chambers) provided comparable growth conditions with those reported in the literature. Therefore, we performed experiments in closed PDMS microfluidic structures comprising separate chambers (Fig. 1 and *SI Appendix*, Fig. S1) (representative images of fungal growth are presented in *SI Appendix*, Fig. S2), as "internal" control, as well as on agar, as "external" control.

The comparison of fungal growth on agar (our external control, and published data) and in closed/nonconstraining conditions (our internal control) demonstrates that they elicit similar growth behavior (Fig. 2, Table 1, and *SI Appendix*) (comparison between agar and PDMS in *SI Appendix*, Table S1 and Fig. S3). First, the cross-sectional apical profiles of the hyphae were parabolic and symmetrical (Fig. 2*A* for internal; and *SI Appendix*, Fig. S4 for external control). Second, the Spitzenkörper was centered at the hyphal apex (*SI Appendix*, Fig. S5 and Movie S1), with small periodic oscillations perpendicular to the growth direction (Movie S2). Third, the microtubules were longer and less aligned with the hyphal axis when further away from the hyphal apex (Movies S3 and S4). This is seen as a broadening of the distribution of the deviations of microtubule angles from the hyphal axis (histograms in Fig. 2*B* representing $n = 852$ microtubules in 20 hyphae, for internal control; and *SI Appendix*, Figs. S4 and S6 for external control). Furthermore, the lateral distribution of microtubules indicated that, while they populated both cortical and central cytoplasmic regions (the entire width of the hypha), their density was higher in the cortical region (Fig. 2*C* for internal control; *SI Appendix*, Fig. S7 for external control) (*SI Appendix*, Table S2 and Fig. S8 present a statistical comparison between the controls). The microtubules extended into the apical dome, displaying a characteristic microtubule-depleted zone in the distal central region that colocalized with the Spitzenkörper (Movie S3). Long-term imaging (5 to 10 min) showed that microtubules occasionally traversed the Spitzenkörper position and frequently terminated at the apical cell wall. The estimated microtubule polymerization rate was 26.4 ± 8.6 μm·s^{-1} ($n = 412$ measurements from 98 microtubules). Finally, long-term imaging showed that this organization along the hyphal axis is interrupted when microtubules passed a septum (*SI Appendix*, Fig. S9 and Movie S5).

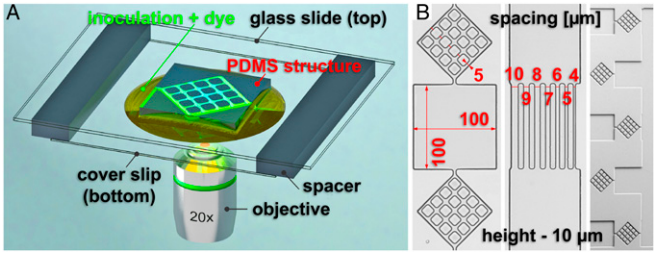

Fig. 1. (*A*) Experimental setup for live-cell imaging of fungal growth in microfluidics structures (not to scale). (*B*) PDMS microfluidics structures for confining fungal growth. (*Left*) Three interconnected chambers, of which the middle one was used to investigate nonconstrained growth, while the top and the bottom ones were used to probe lateral branching in constraining environments. (*Middle*) Channels of varying width for probing lateral branching by level of constraint. (*Right*) Overall image of the entry to the chip, probing the response to collisions at acute and near-orthogonal angles, as well as corner responses.

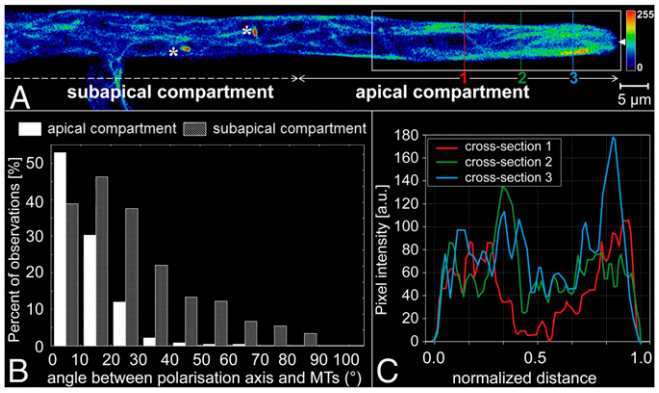

Fig. 2. Spatial distribution of microtubules in *Neurospora crassa GFP* in nonconstraining environments. (*A*) Single-plane fluorescence image of GFP-tagged microtubules within a branched hypha. The colors represent the relative spatial density of microtubules (see color map, arbitrary scale, *Right*). The asterisks indicate mitotic spindles, and the solid white arrowhead at the tip indicates the position of the Spitzenkörper. (*B*) Histogram of microtubule (MT) deviation angles from the hyphal polarization axis in the apical and subapical compartments. (*C*) Microtubule density profiles, plotted as fluorescence intensities along the vertical lines (1 to 3) drawn across the hypha in *A*. The hyphal diameter (~7 μm) was normalized to offset small variations at different sections through the apical compartment.

The lateral branching behavior (branching at ~45° with movement of microtubules into the daughter hypha) was also similar on agar and in closed/nonconstraining PDMS chambers (*SI Appendix*, Figs. S10 and S11 and Movie S6). The central positions and sizes of the Spitzenkörper were also similar (*SI Appendix*, Figs. S11–S13).

After establishing the experimental equivalence between the external control on agar and the internal control in large PDMS chambers, we investigated the effect of geometrical constrainment on hyphal growth using PDMS structures. The geometry of the microfluidic network (Fig. 1*B*) exposed the hyphae to a high density of various structural features (60, 61), such as corners, channels, and entrances and exits from the chambers. This variety of structural features allowed us to observe the intracellular mechanisms of hyphal growth and branching, grouped in three categories of events: Collision with obstacles at acute angles of approach, frontal collision with obstacles, and growth in tightly constraining geometries.

Collision with Obstacles at Acute Angles of Approach. At acute angles of approach, that is, lower than 35° relative to the fixed obstacle surface, hyphae closely followed the contour of the immobile obstacle, a process previously termed "nestling" (60, 61). To establish the underlying intramolecular mechanisms responsible for nestling, we imaged the growth of the hyphae (n = 26) when colliding with PDMS walls at acute angles. We found that nestling dynamics (Fig. 3 and Movie S7) present three phases:

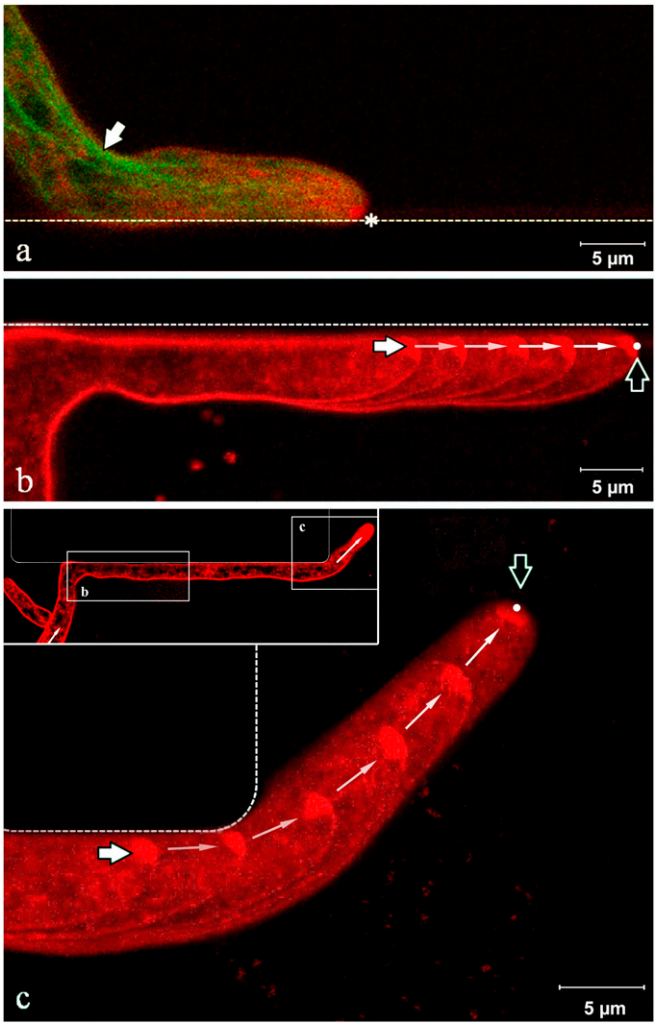

Fig. 3. Spitzenkörper and microtubules dynamics in somatic hyphae nestling against a wall. (*A*) Spitzenkörper (labeled with FM4-64, pseudocolored red) and microtubules (genetically tagged with GFP, pseudocolored green) in the apical hyphal region growing along a PDMS wall (dashed line). The parabolic apex profile is skewed toward the wall. The Spitzenkörper (asterisk) is displaced from its usual central position at the apex as growth is obstructed. The microtubules follow the shortest path toward the Spitzenkörper (white arrow) and are displaced from the central median of the hypha. (*B*) Trajectory of the Spitzenkörper along the wall during nestling. The image is an overlay of five snapshots taken over 4 min. The white and black arrows indicate the beginning and the end, respectively, of the Spitzenkörper trajectory. (*C*) Upon reaching the end of the wall, the hypha recovers its symmetrical parabolic profile, and the Spitzenkörper gradually returns to the apical center. The near-orthogonal angle of contact of the hypha with the horizontal wall is the result of shifting the base by the growth of the daughter hypha on the left. The image is an overlay of six snapshots taken over 7.5 min; the white and black arrows indicate the beginning and the end, respectively, of the Spitzenkörper trajectory. The images in *B* and *C* are from the same hypha at different times, as indicated in the *Inset* of *C*. The complete sequence of images is presented in Movie S7.

1) Before encountering the wall: Similarly to experiments in nonconstraining geometries, the hyphal profile was symmetrical, with the Spitzenkörper located centrally at the apex and the microtubules distributed symmetrically. We consistently observed the absence of any anticipatory change in behavior even before an imminent contact, suggesting the absence of any sensing mechanism.
2) Nestling: We observed four major changes in hyphal morphology upon encountering a wall. First, the growing hypha followed the constrained path imposed by the obstacle as it slid along the wall in the direction of least deviation (Fig. 3*A* and *SI Appendix*, Fig. S14, *Top*). Second, the longitudinal hyphal cross-section shape lost its symmetry and became considerably skewed toward the wall. The hypha continued its progress in close contact with the wall, maintaining this skewed tip profile. Third, the Spitzenkörper markedly shifted away from its previously central apical location, toward the wall. This displacement persisted over distances at least longer than several hyphal diameters (Fig. 3*B* and *SI Appendix*, Fig. S14, *Bottom*). Skewing of the apex during nestling was constant over time: That is, in nestling events in a sequence of up to 10 chambers. Fourth, microtubules tended to gather near the inside edge of the hyphal bend (white arrow in Fig. 3*A*) and toward the wall at the tip (Fig. 3*A* and *SI Appendix*, Fig. S15). The nestling behavior of the Spitzenkörper (that is, shifting away from the axis toward the wall opposing the initial direction of growth) also occurred when a hypha was able to circumnavigate a small immovable obstacle (*SI Appendix*, Fig. S16).
3) Return to nonconstrained growth: After overpassing the end of the wall, within a distance approximately equal to the hyphal diameter, the hypha quickly recovered its original growth direction. Additionally, the hypha resumed its symmetrical profile; the Spitzenkörper simultaneously returned to a central position (Fig. 3*C* and *SI Appendix*, Fig. S17) (Movie S7 presents the complete time series); and the microtubules recovered their symmetrical transversal distribution. Within the spatial range of observation (spanning 10 chambers, each with a length of 100 μm, and observing more than 100 events), the accuracy in the recovery of the direction of hyphal growth did not diminish over time, having negotiated successive bends through the device, or with increasing distance from the initial branching point of that hypha (*SI Appendix*, Fig. S18).

Frontal Collision with Obstacles. Frontal encounters with a wall, at angles of approach greater than 35° relative to the surface of the immovable obstacle, caused the apices of the hyphae to split, a process termed "hit & split." To establish the underlying intramolecular mechanisms responsible for the hit & split process, we imaged the growth of the hyphae colliding with PDMS walls at near orthogonal angles (*SI Appendix*, Fig. S19). Repeated imaging (n = 37 events) provided evidence for a three-phase intracellular process (Fig. 4, *SI Appendix*, Figs. S19–S22, and Movie S8):

1) Polarized approach, before encounter ("Approach" in Fig. 4 *A1*, *B1*, and *C1*): If a hypha approached a wall, similarly to the prenestling phase, microtubules were oriented longitudinally, terminating at the apical region of the cell (*SI Appendix*, Fig. S20*A*).
2) From the moment of encounter to branching ("Collision" in Fig. 4 *A2–A4*, *B2–B4*, and *C2–C4*) comprised three stages: In stage 1 (Fig. 4 *A2*, *B2*, and *C2*), the immovable obstacle blocked the hypha in the direction of growth, causing a small deformation in the elastic PDMS wall (*SI Appendix*, Figs. S19*C* and S21*A*). Hyphal growth then continued quasiorthogonally to the polarization axis, resulting in lateral bulging in the apical region. Simultaneously, the microtubules depolymerized, and the filament ends receded rapidly from the apex (Fig. 4*C2*

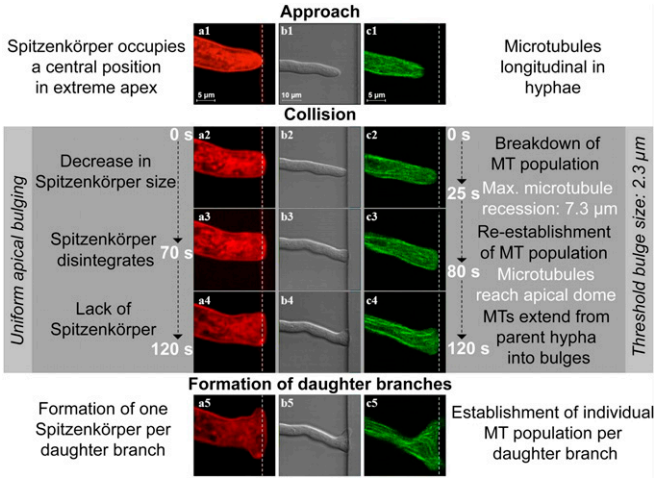

Fig. 4. Phases during frontal obstacle-induced nestling branching following collision with a PDMS wall (white dashed lines). Columns *A* and *C* show fluorescence images of the labeled Spitzenkörper (red) and microtubules (green), respectively, and column *B* shows differential interference contrast images of a hypha. The hypha deforms the elastic PDMS slightly from its original position (*B3* and *B4*). During the approach (*A1* and *A2*), the Spitzenkörper is located at the apical center, and the microtubules organize longitudinally (*C1* and *C2*). Following the encounter, the Spitzenkörper shrinks (*A2*) and ultimately disappears (*A3*), and the microtubules temporarily recede from the apical region (*C3* and *C4*). Concomitantly, the apex grows uniformly (*B3* and *B4*). Finally, two new Spitzenkörper structures form in the daughter branches (*A5*), and the microtubules resume their extension toward both apices (*C5*).

and *SI Appendix*, Fig. S20*B*). At 25 ± 13 s after the collision, the average distance between the obstacle and the microtubule receding end was 7.3 ± 3.7 µm. The Spitzenkörper shrank gradually but did not retract longitudinally from the apical dome (Fig. 4*A2* and *SI Appendix*, Fig. S21*B*). In stage 2 (Fig. 4 *A3*, *B3*, and *C3*), the hyphal profile continued to develop into two bulges. Total dissolution of the Spitzenkörper occurred toward the end of this stage: That is, 70 ± 40 s after the initial encounter (Fig. 4*A3* and *SI Appendix*, Fig. S21*C*). Importantly, the disappearance of the Spitzenkörper also occurred if the hypha pressed and then penetrated a PDMS wall (Movie S9). The microtubules resumed their extension toward the apex, and, after 80 ± 36 s from the collision, their population appeared to be fully recovered in the hyphae (Fig. 4*C3* and *SI Appendix*, Fig. S20*C*). In stage 3, just before branching was initiated and when the hypha did not have a Spitzenkörper, the uniform apical extension continued laterally, following the constraining geometry. The microtubules again extended to the extreme apical cell walls and migrated from the parent hypha into the nascent bulges, ultimately resulting in an extension along the obstacle walls (Fig. 4*C4* and *SI Appendix*, Fig. S20*D*).

3) Branching ("Formation of daughter branches" in Fig. 4 *A5*, *B5*, and *C5*): Approximately 2 min after the encounter, the uniform extension changed to a bidirectional, polarized pattern, with the bulges reaching 2.3 ± 1.3 µm in length. The sizes of the bulges immediately before forming new branches correlated moderately ($r = 0.65$, $P < 0.05$) with the initial diameter of the parent hypha. The change in polarization pattern coincided with the nucleation of two smaller "daughter" Spitzenkörper structures—one for each new branch (Fig. 4*A5*) (*SI Appendix*, Figs. S21*D* and S22 present the overlap of Spitzenkörper trajectory during the process of hit & split). Independent microtubule populations developed within each branch to conclude the branching process (Fig. 4*C5* and *SI Appendix*, Fig. S20*D*).

Additional evidence of the intracellular processes during the hit & split in more complex geometries is presented in *SI Appendix*, Fig. S23, which shows a sequence of images showing the Spitzenkörper in the process of a hypha colliding with an obstacle, slightly larger than its diameter, which split it into two branches. *SI Appendix*, Figs. S24 and S25 and Movie S10 present the evolution of the microtubules when a hypha collided near orthogonally with a short obstacle that blocked the formation of a second branch. In this instance, once the branch is formed, the microtubules present the characteristic corner-cutting pattern (*SI Appendix*, Fig. S25). Finally, Movie S11 presents a similar lateral branching due to the collision of a hypha with a corner that does not allow the formation of two branches.

Growth and Branching in Tightly Constraining Geometries. To establish the underlying intramolecular mechanisms responsible for growth and branching in tightly constrained geometries, we imaged the evolution of the hyphae in channels with widths smaller than their diameter, without and with lateral opening, and in dead-end corners.

First, when *N. crassa* progressed in long, linear, tight channels without lateral exits ($n = 14$), the hyphae branched immediately upon cessation of the confinement: For example, at a channel opening into a larger volume (Movie S12), with both hyphae generating their own Spitzenkörper soon after exit (*SI Appendix*, Fig. S26). Importantly, the behavior manifested during nestling (that is, preservation of the initial direction of growth by the Spitzenkörper before entering the tight channel) was also present (*SI Appendix*, Fig. S27). Additionally, the microtubules exhibited the same pattern: That is, pressing against the wall opposite to the initial direction of growth (*SI Appendix*, Figs. S27 and S28).

Second, for hyphae growing in channels with lateral exits ($n = 25$), branching occurred almost immediately when passing this opening (Fig. 5 and *SI Appendix*, Fig. S29 for Spitzenkörper; *SI Appendix*, Fig. S30 for microtubules; and Movie S13).

The growth and branching into lateral openings proceeded in three phases ($n = 20$ hyphae):

1) Entry and apical growth in the channel ("Approach" in Fig. 5 *A1*, *B1*, and *C1*): Upon entering the confining channel (Fig. 5 *A1* and *B1*), the hypha grew along its initial direction, without turning into lateral channels. Similarly to nestling, the Spitzenkörper was closer to the walls opposite to the initial direction of growth (*SI Appendix*, Fig. S29). The microtubules were oriented longitudinally within the parent hypha (Fig. 5*C1* and *SI Appendix*, Fig. S30*A2*).
2) Formation of a proto-branch ("Lateral opening" in Fig. 5 *A2–A4*, *B2–B4*, and *C2–C4*): If the hypha encountered a lateral opening, the subapical region extended into it, producing a bulge (Fig. 5 *A2*, *B2*, and *C2* and *SI Appendix*, Fig. S30*A1*). The longitudinal orientation of the microtubules in the parent hypha was conserved (without moving toward the bulge, even after the hyphal apex passed the lateral opening), but eventually polarization occurred (Fig. 5*C3* and *SI Appendix*, Fig. S30*B*), followed by microtubule transfer from the parent into the developing branch (Fig. 5*C4* and *SI Appendix*, Fig. S30*C*). Approximately halfway through this process (~70 s) (Fig. 5 *A3*, *B3*, and *C3*), the emerging branch formed its own Spitzenkörper, and the microtubule populated the branch (*SI Appendix*, Fig. S30*D*).
3) Development of a stand-alone branch (Fig. 5 *A5*, *B5*, and *C5*): Subsequent development was characterized by the formation of a separate population of microtubules and an independent daughter hypha (Fig. 5*C5* and *SI Appendix*, Fig. S30 *E* and *F1*). Interestingly, features associated with directional memory appeared early: For example, the ability of microtubules to cut corners (Fig. 5*C5*). This process occurred within a few minutes of the initial crossing by the parent apex.

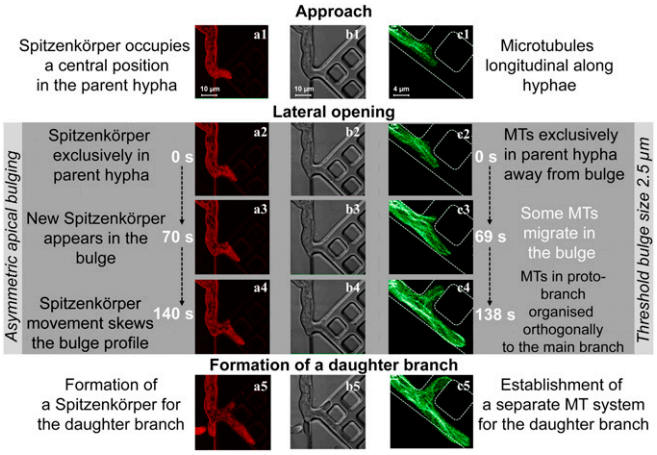

Fig. 5. Phases of hyphal branching into a lateral channel (white dashed lines). Columns *A* and *C* show fluorescence images of the labeled Spitzenkörper (red) and microtubules (green), and column *B* shows differential interference contrast images of a hypha. The parent branch preserves its Spitzenkörper throughout. Upon entering the channel (*A1*, *B1*, and *C1*), the Spitzenkörper preserves the initial growth direction (*Top Left* in *A1*), being positioned along the wall. The parent hypha in images (*C1* and *C2*) passes the intersection while the daughter branch forms orthogonally. Whereas the cell wall partially follows the lateral gap (*A2*, *B2*, and *C2*), the formation of the daughter hyphae is delayed by the formation of the Spitzenkörper–microtubule system. Eventually, the daughter hypha forms its Spitzenkörper and microtubule population approximately simultaneously (*A3*, *B3*, and *C3*). Microtubules are initially distributed longitudinally in the parent hypha and do not extend into the bulge. Between frames *C3* and *C4*, the microtubules start to extend from the parent hypha into the bulge, indicating the formation of the daughter hypha. The development of this branch is completed by the formation of an independent microtubule population (*C5*).

Aside from observing the mechanisms involved in branching, the visualization of hyphae growing in tightly constraining channels offered additional evidence regarding the structuring of the microtubule cytoskeleton following changes of the direction of growth, now obligated by the meandering geometries. Similarly to nestling, the pattern of microtubules preferentially distributed toward the wall opposing the direction of growth ("cutting corners" patterns) was also observed when hyphae navigated meandering channels with widths of 5 µm (Fig. 6, *SI Appendix*, Figs. S31 and S32, and Movies S14 and S15), despite the necessity of passing through centrally located septa (*SI Appendix*, Fig. S33).

Discussion

Studies describing the intracellular processes involved in fungal hyphal extension and branching predominantly used flat, nonconstraining agar surfaces. Advanced microscopy dictates the use of transparent substrates on which the hyphae grow. However, these experimental frameworks (that is, flat surfaces and transparent media) are dissimilar to the natural habitats of filamentous fungi, environments that comprise constraining geometries, which are expected to interfere with the mechanisms of fungal growth being studied. Our previous studies on the growth of the filamentous fungi *P. cinnabarinus* (60) and *N. crassa* (61, 62) in PDMS microfluidic structures identified two efficient space-searching strategies—directional memory and obstacle-induced branching. Summarizing the results of the fluorescence live imaging of the growth of *N. crassa* in microfluidic networks, presented above, when a hypha was deflected by an immovable obstacle, the Spitzenkörper shifted from its central position in the hyphal apex toward the obstacle opposing the growth and returned to its central position when the mechanical constraint ceased. In these instances, the microtubules followed the trajectory of the Spitzenkörper, resulting in cutting corners patterns. Finally, when the immovable obstacle could not be circumnavigated, the Spitzenkörper–microtubules system in the parent hypha disintegrated, followed by branching which allowed the growth to proceed, and concluded with the creation of independent Spitzenkörper–microtubules systems in the daughter hyphae.

Intracellular Mechanisms of Growth in Nonconstraining PSMS-Made Environments. We observed that the behavior of *N. crassa* in nonconstraining PDMS-made environments was similar to that on agar, both observed by us and as reported in the literature. First, in our experiments, the hyphal profile was parabolic and symmetrical (Fig. 2*A* and *SI Appendix*, Fig. S4), as also previously demonstrated and comprehensively described mathematically (64–66). Second, the Spitzenkörper was located centrally at the hyphal apex (*SI Appendix*, Fig. S5 and Movie S1) as described in early classical studies (67). Also, the observed oscillations orthogonal to the growth direction (Movie S2) were consistent with a previous report (8). Third, the microtubules were generally orientated parallel to the longitudinal hyphal axis (Fig. 2*A* and *SI Appendix*, Figs. S6–S8 and Table S2), and their accumulation toward the apical region correlates well with previous observations (25, 27, 28). The observed microtubule polymerization rate (26.4 ± 8.6 µm·s^{-1}) was consistent with previously reported results obtained for hyphal growth on agar (25).

In conclusion, a high degree of similarity exists between the growth behavior and relevant intracellular processes in closed/nonconstraining PSMS-made microfluidic chambers, and those observed during experiments made on agar, as reported here and in the literature. Therefore, the experiments in large microfluidic

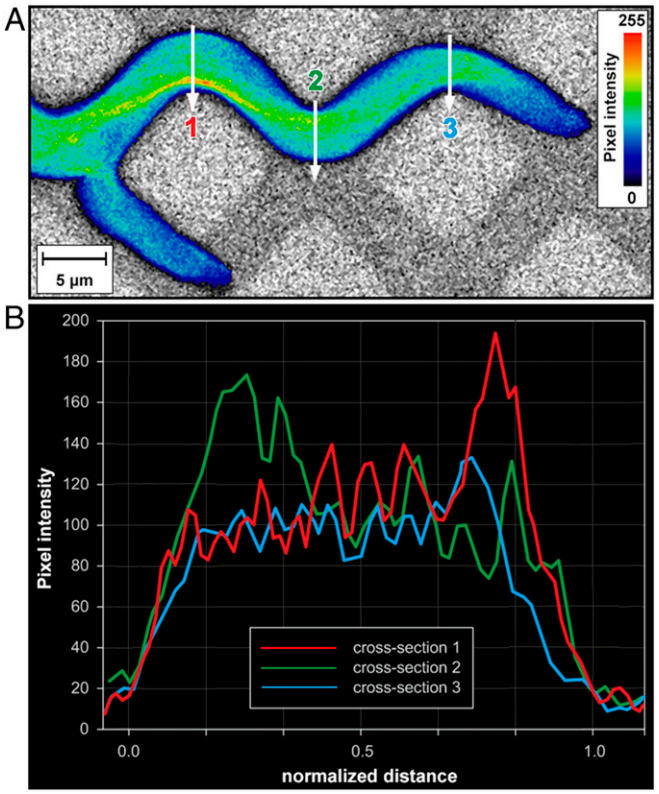

Fig. 6. Spatial distribution of microtubules in *Neurospora crassa GFP* in constraining meandered channels. (*A*) Single-plane fluorescence image of GFP-tagged microtubules. The microtubule alignment largely follows the initial direction of growth at the entry into the constraining channel. The colors represent the relative spatial density of microtubules (see color map, *Right*). (*B*) Microtubule density profiles, plotted as the fluorescence intensities along the vertical lines (1 to 3) drawn across the hyphal cross-section in *A*.

chambers are valid benchmarks for assessing the impact of constraint on fungal growth.

Intracellular Mechanisms Responsible for Directional Memory During Nestling. In general, the extension of a hypha over a flat surface followed a direction determined at the initial branching point, usually at an angle of ∼45° from the parent hypha. We have previously shown (60, 61) that, in constraining geometries, the growth is forced to change direction due to an immovable obstacle, but, once the hyphae circumnavigate it, they recover their initial direction of growth to within an ∼20° error. This directional memory persists even over distances greater than 10 times the hyphal diameter, regardless of the number of encountered collisions. Interestingly, the directional memory has been demonstrated in both *P. cinnabarinus* (60) and *N. crassa* (61), but not in a cytoskeleton-defective *N. crassa* ro-1 mutant (61). This observation suggests that the cytoskeleton plays a key role in maintaining directional memory in constraining geometries.

Our results in nonconstraining environments (presented here, both on agar and in large PDMS chambers lacking internal obstacles) confirmed previous observations that hyphal growth follows the positions adopted by the Spitzenkörper (8). However, although this observation remains valid if hyphae circumnavigate immobile obstacles by nestling, it requires important qualification. Indeed, if a hypha slid past an immovable barrier at an acute angle of contact, the Spitzenkörper functioned like a gyroscope, maintaining the growth direction that the hypha had before the encounter (Fig. 3, *SI Appendix*, Fig. S14, and Movie S7). One possible explanation for this hitherto unknown phenomenon is that the pressure applied to the hyphal wall due to the mechanical contact with the obstacle results in an intracellular signal that triggers consolidation of the hyphal wall at the zone of contact. This process would require the off-axis positioning of the Spitzenkörper and pressure on the contact point between the hyphal wall and the obstacle (as confirmed by additional experiments, in different settings) (*SI Appendix*, Figs. S16, S17, S27, and S29). Furthermore, the off-axis position of the Spitzenkörper creates a skewed microtubule cytoskeleton, which leads to the characteristic pattern of "cutting corners" (Fig. 3*A*)—especially when the directional memory causes hyphae to negotiate corners in various geometries (*SI Appendix*, Figs. S15, S24, S25, S27, S28, S31, and S32 and Movies S12 and S13). This effect is even more remarkable when considering that the microtubules must pass through narrow septa, which are centrally located on the median line of the hypha (*SI Appendix*, Figs. S9 and S33 and Movie S5) (68, 69). The functional synergy between the gyroscope-like Spitzenkörper and the subsequent preferential positioning of the microtubules along a line approximating the initial direction of hyphal growth appears to constitute the underlying intracellular mechanism for directional memory, which was observed for distances at least one magnitude longer than hyphal diameters (the hyphal trajectories in Movie S7 are longer than 100 μm; and the distances in *SI Appendix*, Fig. S18 are several hundred micrometers).

More detailed experiments regarding the role of F-actin structures—actin rings, patches, and cables (33)—which are more difficult to visualize than microtubules (33, 34), might reveal their potential role in directional memory. However, because actin cables are colocalized near the Spitzenkörper and behind actin rings, it is expected that the role of actin is limited, at least in relation to the long range of directional memory.

Intracellular Mechanisms Involved in Obstacle-Induced Branching During Hit & Split. Our previous experiments with *N. crassa* (61) showed that containment in various microfluidic structures, comprising channels with widths similar in size with hyphal diameters, results in a shortened distance between hyphal branching points by a factor of 5 to 10 (the growth rate also decreases 10-fold). We also observed (61) that, immediately after the contact between a hypha and a constraining structure at a near-orthogonal angle, branching occurs at the apex of the hypha. This hit & split branching contrasts the behavior presented by *P. cinnabarinus* (60), which branches at a considerable distance behind the hyphal apex.

Similarities and differences between the Spitzenkörper dynamics in collision-triggered hit & split and collision-independent apical branching. The intracellular mechanisms responsible for the collision-induced behavior mentioned above, as revealed by our experiments, present some similarities with the processes previously shown to take place during collision-free apical branching of *N. crassa* on agar (27, 70). For instance, both the disappearance of the parent Spitzenkörper that we observed after microtubule contraction from the apex region and the nucleation of the two daughter Spitzenkörper centers were also observed in the apical branching of *N. crassa* on agar (70). More specifically, in internally triggered apical branching on agar, the Spitzenkörper retracts 12 s after cytoplasmic contraction from the apex which precedes the branching and disappears after another 47 s; later, 45 s after the start of isotropic, uniform, and slower growth of the parental and daughter hyphae, one Spitzenkörper nucleates, followed by a second ∼7 s later, leading to the establishment of two new branches (70). By comparison, in our observations of hit & split branching (Fig. 4 and *SI Appendix*, Figs. S21 and S22), the Spitzenkörper was not visible until 50 s after hitting the obstacle. Moreover, the decrease we observed in Spitzenkörper size, its subsequent disappearance, and the assembly of two new daughter Spitzenkörper centers away from the parent represent a typical sequence of events that also occurs naturally in apically branching fungi: For example, *Sclerotinia sclerotiorum* (21).

Conversely, our experiments regarding the intracellular mechanisms responsible for the collision-induced behavior also show important differences with respect to the processes during collision-free apical branching of *N. crassa* on agar (70). First, on homogeneous agar substrates, the branching of *N. crassa* hyphae occurs predominantly laterally, not apically (70). In contrast, in hit & split branching in constraining environments, we observed that apical branching was the prevalent process. Second, in the absence of a Spitzenkörper, the apical extension stalls in *S. sclerotiorum* (21) and is notably reduced in *N. crassa* branching apically on agar (70). In contrast, this delay in apical extension was not observed in our experiments with *N. crassa* colliding frontally with a wall. We attribute this difference between hit & split branching and the apical branching in nonconstraining environments to different trigger mechanisms. For example, an apical split can occur on agar a few minutes after the induction of an intracellular process free of external stimuli, whereas the immediate response of *N. crassa* following a frontal collision with an obstacle, as observed in the present study, can be the result of a highly localized in time and space contact-induced signal.

Similarities and differences between microtubule dynamics in collision-triggered hit & split and collision-independent apical and lateral branching. The behaviors of the microtubules in apical and lateral branching on agar are similar (27), but we found that they are markedly different during the hit & split response. In unconstrained apical or lateral branching on agar, the microtubule population is relatively unchanged throughout the branching process whereas a hit & split response appeared to trigger the depolymerization of the microtubules (Fig. 4*C2* and *SI Appendix*, Figs. S20 and S21). Furthermore, if a hypha encountered a corner (Movie S11), the resulting budding branch was not initially populated with microtubules, suggesting that the association of microtubules with the apical cell wall is not a prerequisite for selecting a branching site, as has been observed for lateral branching in nonconstraining environments (27), but which could be alternatively explained by cell wall deformation driven by isotropic turgor pressure.

The role of actin in hit & split branching, as with nestling, is yet to be established. However, as it was shown for two species of yeast (71) and for *N. crassa* (72), actin is not present at the tip of invasive hyphae: That is, those pressing against agar in conditions similar to our experiments (Movies S8, S9, and S11). Consequently, it is reasonable to assume that the contribution of actin to hit & split branching is minimal.

Overlap of Intracellular Mechanisms of Directional Memory and Obstacle-Induced Branching During Lateral Branching. We found that the lateral branching that occurs in tightly constraining microfluidic channels was only partly similar to lateral branching in nonconstraining conditions. At the beginning of lateral branching in nonconstraining geometries, we observed the association of cortical microtubules with the cell wall at the location of the developing lateral branch. Upon further extension, the microtubules gathered and bent considerably. The severed ends of microtubules then migrated into the branch and resumed polymerization. These observations are consistent with other studies of lateral branching on flat agar surfaces (27). Importantly, though, in our tightly constraining channels, the original Spitzenkörper remained intact in the parent hypha during lateral branching, and a new Spitzenkörper appeared independently within the daughter branch. This has also been observed in lateral branching in nonconstraining conditions (70).

The most obvious difference between lateral branching in tightly constrained geometries and that on flat surfaces was in the place and frequency of branching. These appeared to be dictated by the availability of lateral space, rather than triggered by internal processes, as appears to be the case in nonconstraining conditions. Moreover, in tight channels, there was a close temporal correlation between the presence of the constraining geometry and the lateral branching, enforced by the axis of the available space (e.g., orthogonal in Fig. 6; also *SI Appendix*, Figs. S29 and S30). Also *N. crassa* branched typically and almost immediately after an exit from a bottleneck (Movie S12) (61). These observations suggest that the isotropic turgor pressure is essential for initiating lateral branching events in tightly constrained environments.

Finally, the branching we observed in constraining environments differed from that on open, flat agar surfaces, involving the same genetically tagged *N. crassa* strain (25). In our study, no cortical microtubules were observed to bend or shatter. Cell wall deformation preceded microtubule extension from the parent hypha into the nascent bud, making it appear the dominant event in the chain leading to branch formation. The bulging of the cell wall into an intersection of channels also preceded the formation of a daughter Spitzenkörper (*SI Appendix*, Fig. S23), suggesting that the nucleation of the Spitzenkörper occurs after the initiation of branching, as opposed to lateral branching on open surfaces (25).

Lateral branching in tightly constraining channels appears to be the result of coupling of the Spitzenkörper–microtubules-controlled directional memory for the growth of the parental hypha, simultaneously with turgor pressure-controlled obstacle-induced branching of the daughter hypha.

Intracellular Mechanisms of Directional Memory and Obstacle-Induced Branching. By using time-lapse confocal fluorescence microscopy to observe growth of *N. crassa* in constraining microfluidic environments, we revealed substantial differences in the intracellular processes involved in the fungal search for space for hyphal growth, compared with those manifested in nonconstraining conditions. These differences are presented in Table 1.

Our study shows that the intracellular processes involved in the growth of *N. crassa* in constraining geometries are triggered and modulated by the type of obstacles encountered by hyphae. Of the two important behavioral traits of *N. crassa* in growth-constraining environments (61), directional memory appears to arise from the Spitzenkörper "remembering" the initial direction of growth, pressing against opposing obstacles encountered at an acute angle of attack, and then returning to the initial direction when the blocking obstacle is left behind and contact with the hypha ceases. This gyroscope-like dynamic memory is further stabilized by the structuring of the microtubules in the wake of the trajectory of the Spitzenkörper, resulting in the characteristic corner-cutting feature of the microtubule cytoskeleton in meandering channels. Directional memory, described as a behavioral trait of some fungal species (60, 61), may provide biological advantages for filamentous fungi growing and foraging in geometrically heterogeneous environments. Indeed, stochastic simulations showed that suppressing directional memory in *P. cinnabarinus* (60) increases the probability of hyphae being trapped in a network. Furthermore, an *N. crassa* ro-1 mutant that did not display directional memory presented a considerably lower capacity for exiting complex geometries than the wild-type *N. crassa* (61).

In contrast to the intracellular processes involved in directional memory, the Spitzenkörper–microtubules system does not appear to determine the direction of obstacle-induced branching. Indeed, in hit & split events, both the Spitzenkörper and microtubules are absent at the critical point of apical splitting. The obstacle-induced branching observed in species exhibiting directional memory (60–62) suggests that this behavioral trait also affords biological advantages. Indeed, stochastic simulations (60) have demonstrated that obstacle-induced branching leads to a higher capacity for exiting complex networks, but with a lesser benefit than directional memory. Consequently, it appears that *N. crassa* has evolved intracellular processes responsible for directional memory and obstacle-induced branching, with the former being the main driver for the negotiation of complex networks, and the latter a fallback mechanism when directional memory is turned off during near-orthogonal collisions, or when it cannot operate due to the constraints imposed by tight geometries.

Perspectives and Further Work. Aside from revealing fundamental intracellular mechanisms involved in fungal growth, this study may have further impact, or suggest further research, as follows:

- Our PDMS microfluidic devices, in conjunction with advanced microscopy imaging, could be used in fundamental microbiology studies to trigger spatiotemporally precise biomolecular events which are modulated by the cellular interaction with the solid environment—for example, to investigate other elements controlling the fungal growth in confined spaces. Two aspects appear to ask for special attention: The mechanisms responsible for the dissolution of the Spitzenkörper and the associated depolymerization of microtubules in the initial stages of hit & split; and the role of actin structures in the hyphal growth in constrained geometries, in particular when the Spitzenkörper/microtubule system is not present or observable.
- Our devices could be designed more closely to mimic fungal environments, to bring about environmental, industrial, and medical applications, including fungal pathogenicity, which is controlled by the successful negotiation of meandering geometries made of multicellular constructs in animals and plants. For instance, the mechanical strength of PDMS could be adjusted to allow the estimation of the forces applied by fungi in various environments, by the measurement of resultant deformations, as already demonstrated (73, 74). Alternatively, the design of the PDMS structures could mimic the structure of the walls of plant or animal tissue in studies on fungal invasion.
- The confinement imposed on the growth of filamentous fungi could be applicable to biologically driven computation. For instance, it was shown (62) that a genetically engineered, cytoskeleton-defective mutant of *N. crassa* that produces short branches preferentially at 90° can solve orthogonal mazes better than the wild-type strain, which overwhelmingly branch at 45°. Furthermore, as the natural space-searching strategies used by fungi have been demonstrated to be more efficient than some artificial algorithms (63), it is possible to use either wild-type or genetically engineered fungi to attempt solving complex physical networks encoding combinatorial mathematical problems, as proposed (75), and recently demonstrated (76). Alternatively, the nuclear dynamics in *N. crassa* (77) could be "streamlined" in networks mimicking real, complex, transportation webs, thus allowing studies on traffic optimization (77–79). A conceptual framework for doing so has been demonstrated for *Physarum polycephalum* (80).

Table 1. Comparison of intracellular processes involved in the growth and branching of *N. crassa* in open and constraining environments

Growth	Hypha	Spitzenkörper	Microtubules
		Nonconstraining geometries	
Single hypha	Profile: Parabolic, laterally symmetrical	Location and dynamics: Central, at the hyphal apex; permanently present	Orientation: Parallel to axis Distribution: Axially symmetrical Dynamics: Population relatively constant
	Source: Agar (65–67)* and CNC*	Source: Agar (68)* and CNC*	Source: Agar (43–45)* and CNC*
Lateral branching	Occurrence: Statistically regular Angle: ∼45° Profiles: Parabolic for parental, daughter hyphae Apical extension: Reduced during branching	Location and dynamics: Central, at the hyphal apices; permanently present in parental hypha; early appearance in the daughter hypha	Orientation: Parallel to hyphal axes Distribution: Axially symmetrical Dynamics: Population relatively constant
	Source: Agar (21)* and CNC*	Source: Agar (21) and CNC*	Source: Agar (21) and CNC*
Apical branching	Occurrence: Regular, but rare Angle: V-shaped, ∼45° Profiles: Initial round-up for the twin hyphae Apical extension: Reduced during branching	Location and dynamics: It retracts from the apex and disappears; then, two Spitzenkörper centers emerge at the centers of hyphal apices	Orientation: Parallel to hyphal axes Distribution: Axially symmetrical Dynamics: Population relatively constant
	Source: Agar (21)	Source: Agar (21)	Source: Agar (44, 74)
		Constraining geometries	
Nestling	Occurrence: Triggered by contact at acute angles Angle: Change of direction as dictated by the wall Profiles: Skewed off-axis, toward the wall Apical extension: Unchanged	Location and dynamics: Off-axis location, pressing against the obstacle; return to central position after passing the obstacle	Orientation: Aligned off-axis Distribution: Axially asymmetrical, "cutting corners" Dynamics: Population relatively constant
Hit & split	Occurrence: Triggered by near-orthogonal collisions Angle: T-shaped, at ∼180° Profiles: Triangular; then, progressively parabolic Apical extension: Constant during splitting	Location and dynamics: It disappears during splitting of parental hypha; then, two Spitzenkörper centers form centrally at the apex of twin branches	Orientation: Random close to the splitting Distribution: Random close to the splitting Dynamics: Substantial dissolution; then, formation in twin hyphae
Branching in/after tightly constraining channels	Occurrence: Triggered by free space for branching Angle: Dictated by geometry Profiles: Parabolic for parental hypha; circular, then increasingly parabolic for daughter hypha Apical extension: Constant during branching	Location and dynamics: Parental Spitzenkörper progresses unchanged; the daughter hypha forms its own Spitzenkörper early and centrally	Orientation: Parallel to the hyphal axes Distribution: Axially symmetrical Dynamics: Populations relatively constant

CNC, confined, but nonconstraining.
*Present study.

Conclusions

Our study of the response of *N. crassa* growth to the geometrical constraints imposed by a PDMS-based microfluidic structure has revealed how the Spitzenkörper–microtubule system is closely linked to directional memory when hyphae encounter obstacles at acute angles of contact. Conversely, if the hyphae collide near-orthogonally with fixed obstacles that block their growth, the temporary absence of the Spitzenkörper–microtubule system results in the loss of directional memory, and growth continues due to ever-present isotropic turgor pressure. Finally, if free space becomes available laterally from tightly constraining channels, the directional memory cannot operate, again leaving turgor pressure responsible for hyphal lateral branching.

These findings can accelerate further studies on the intracellular processes driving fungal growth in confined environments and may have impact on a range of environmental, industrial, and medical applications, from fungal pathogenicity in plants and animals to biologically driven computation.

Methods

Microfabrication and Experimental Setup. The microfluidic network (Fig. 1 and *SI Appendix*, Fig. S1) presents various levels of containment to fungal

growth, from tight-constraining in channels with widths smaller than the hyphal diameter (5 to 7 μm) to confined, but nonconstraining chambers (100 × 100 × 10 μm). The design of the microfluidic network allowed the investigation of fungal behavior as influenced by various levels of confinement and constraint (detailed in *SI Appendix*, Fig. S34).

Fungal Species, Growth Media, and Staining. *N. crassa* was selected as the model organism because we could benchmark our results regarding growth and branching in microenvironments with a large body knowledge related to open spaces and because many mutants are available for experimental studies. *Neurospora crassa rid (RIP4) mat a his-3+::Pccg-1-Bml+sgfp+* mutant strain (henceforth "*Neurospora crassa GFP*") [Fungal Genetics Stock Center (FGSC) no. 9519] was used for the study. The high level of nutrients was necessary to ensure the canceling of the (possible) chemotaxis-driven growth directionality. The FM4-64 dye (Invitrogen Ltd.) was used as a marker for Spitzenkörper.

Time-Lapse Microscopy and Image Analysis. Live-cell imaging used an inverted laser-scanning microscope (Zeiss Axio Observer Z1 with LSM 5 Exciter RGB, Carl Zeiss) with photomultiplier detectors. Fluorescence and bright-field time-lapse images were captured simultaneously and analyzed using image processing software (Zen 2008, Carl Zeiss).

Growth Experiments on Agar and Microfluidic Structures. Control measurements for fungal growth in nonconstraining environments were performed on 1% wt/vol malt extract media using somatic hyphae at the edges of the colony. Hyphal growth rates were measured by tracking the position of the extreme hyphal apices in subsequent frames. Fungal growth was recorded for the period needed to observe hyphal behavior from the entry in, to the exit from, the microfluidic network of interest, which require ∼20 min for a straight 100-μm channel. Due to the more convoluted geometries and the presence of multiple hyphae, in many instances, the image recording lasted more than 1 h. To measure the rates of microtubule polymerization within the apical compartment and to distinguish this from motility, the positions of individual filament ends were tracked frame-by-frame, following a methodology reported previously (25).

Statistical Analysis. Statistica 7.1 (Statsoft Inc.) and GraphPad Prism 6.01 (GraphPad Software Inc.) were used for statistical analysis and correlation tests. Statistical analyses included calculating the mean and SD values of parameters measured: i.e., position, alignment with the hyphal axis, polymerization rate for microtubules, times before reappearance of the Spitzenkörper, and hyphal bulge dimensions, over the total number *n* data points, reported for each instance. Statistical analyses included all accumulated data from at least 20 separate experiments (unless otherwise stated).

A full account of the methods is presented in *SI Appendix*.

ACKNOWLEDGMENTS. This work was financially supported by the European Union Seventh Framework Programme (FP7/2007-2011) under Grant Agreement 228971 [Molecular Nano Devices (MONAD)]; by a Research Project Grant from Leverhulme Trust; and by grants from the Defense Advanced Research Projects Agency under Grant Agreements N66001-03-1-8913 and HR0011-16-2-0028. We thank Dr. Adam Hendricks (McGill University) for insightful suggestions; and Drs. Abraham P. Lee and Lisen Wang (University of California, Irvine) for the fabrication of the microfluidic masters.

1. G. Fischer, Opportunistic filamentous fungi–Species spectrum and abundance in the human environment. *Umweltmed. Forsch. Prax.* **15**, 84–91 (2010).
2. M. C. Fisher *et al*., Emerging fungal threats to animal, plant and ecosystem health. *Nature* **484**, 186–194 (2012).
3. P. Baldrian, V. Valásková, Degradation of cellulose by basidiomycetous fungi. *FEMS Microbiol. Rev.* **32**, 501–521 (2008).
4. W. Purahong, K. D. Hyde, Effects of fungal endophytes on grass and non-grass litter decomposition rates. *Fungal Divers.* **47**, 1–7 (2011).
5. M. D. Fricker, N. S. White, G. Obermeyer, pH gradients are not associated with tip growth in pollen tubes of Lilium longiflorum. *J. Cell Sci.* **110**, 1729–1740 (1997).
6. A. Brand, N. A. R. Gow, Mechanisms of hypha orientation of fungi. *Curr. Opin. Microbiol.* **12**, 350–357 (2009).
7. P. Molin, P. Gervais, J. P. Lemière, T. Davet, Direction of hyphal growth: A relevant parameter in the development of filamentous fungi. *Res. Microbiol.* **143**, 777–784 (1992).
8. M. Riquelme, C. G. Reynaga-Peña, G. Gierz, S. Bartnicki-García, What determines growth direction in fungal hyphae? *Fungal Genet. Biol.* **24**, 101–109 (1998).
9. N. P. Money, Insights on the mechanics of hyphal growth. *Fungal Biol. Rev.* **22**, 71–76 (2008).
10. G. Steinberg, Hyphal growth: A tale of motors, lipids, and the Spitzenkörper. *Eukaryot. Cell* **6**, 351–360 (2007).
11. J. G. H. Wessels, Fungi in their own right. *Fungal Genet. Biol.* **27**, 134–145 (1999).
12. J. I. Prosser, A. P. J. Trinci, A model for hyphal growth and branching. *J. Gen. Microbiol.* **111**, 153–164 (1979).
13. A. P. J. Trinci, A study of the kinetics of hyphal extension and branch initiation of fungal mycelia. *J. Gen. Microbiol.* **81**, 225–236 (1974).
14. S. D. Harris, Branching of fungal hyphae: Regulation, mechanisms and comparison with other branching systems. *Mycologia* **100**, 823–832 (2008).
15. E. J. Bottone, N. Nagarsheth, K. Chiu, Evidence of self-inhibition by filamentous fungi accounts for unidirectional hyphal growth in colonies. *Can. J. Microbiol.* **44**, 390–393 (1998).
16. C. Indermitte, M. Liebling, H. Clémençon, Culture analysis and external interaction models of mycelial growth. *Bull. Math. Biol.* **56**, 633–664 (1994).
17. R. R. Lew, How does a hypha grow? The biophysics of pressurized growth in fungi. *Nat. Rev. Microbiol.* **9**, 509–518 (2011).
18. M. Riquelme *et al*., Architecture and development of the Neurospora crassa hypha–A model cell for polarized growth. *Fungal Biol.* **115**, 446–474 (2011).
19. S. Bartnicki-Garcia, D. D. Bartnicki, G. Gierz, R. López-Franco, C. E. Bracker, Evidence that Spitzenkörper behavior determines the shape of a fungal hypha: A test of the hyphoid model. *Exp. Mycol.* **19**, 153–159 (1995).
20. C. E. Bracker, D. J. Murphy, R. Lopez-Franco, "Laser microbeam manipulation of cell morphogenesis growing in fungal hyphae" in *Functional Imaging and Optical Manipulation of Living Cells* (SPIE, Bellingham, WA, 1997), pp. 67–80.
21. S. Fischer-Parton *et al*., Confocal microscopy of FM4-64 as a tool for analysing endocytosis and vesicle trafficking in living fungal hyphae. *J. Microsc.* **198**, 246–259 (2000).
22. M. Girbardt, Die Ultrastruktur der Apikalregion von Pilzhyphen. *Protoplasma* **67**, 413–441 (1969).
23. S. D. Harris *et al*., Polarisome meets spitzenkörper: Microscopy, genetics, and genomics converge. *Eukaryot. Cell* **4**, 225–229 (2005).
24. J. Verdín, S. Bartnicki-Garcia, M. Riquelme, Functional stratification of the Spitzenkörper of Neurospora crassa. *Mol. Microbiol.* **74**, 1044–1053 (2009).
25. M. Uchida, R. R. Mouriño-Pérez, M. Freitag, S. Bartnicki-García, R. W. Roberson, Microtubule dynamics and the role of molecular motors in Neurospora crassa. *Fungal Genet. Biol.* **45**, 683–692 (2008).
26. T. Horio, Role of microtubules in tip growth of fungi. *J. Plant Res.* **120**, 53–60 (2007).
27. R. R. Mouriño-Pérez, R. W. Roberson, S. Bartnicki-García, Microtubule dynamics and organization during hyphal growth and branching in Neurospora crassa. *Fungal Genet. Biol.* **43**, 389–400 (2006).
28. M. Freitag, P. C. Hickey, N. B. Raju, E. U. Selker, N. D. Read, GFP as a tool to analyze the organization, dynamics and function of nuclei and microtubules in Neurospora crassa. *Fungal Genet. Biol.* **41**, 897–910 (2004).
29. G. J. Hyde, D. Davies, L. Perasso, L. Cole, A. E. Ashford, Microtubules, but not actin microfilaments, regulate vacuole motility and morphology in hyphae of Pisolithus tinctorius. *Cell Motil. Cytoskeleton* **42**, 114–124 (1999).
30. L. Cassimeris, N. K. Pryer, E. D. Salmon, Real-time observations of microtubule dynamic instability in living cells. *J. Cell Biol.* **107**, 2223–2231 (1988).
31. Z. Schultzhaus, L. Quintanilla, A. Hilton, B. D. Shaw, Live cell imaging of actin dynamics in the filamentous fungus Aspergillus nidulans. *Microsc. Microanal.* **22**, 264–274 (2016).
32. A. Bergs, Y. Ishitsuka, M. Evangelinos, G. U. Nienhaus, N. Takeshita, Dynamics of actin cables in polarized growth of the filamentous fungus Aspergillus nidulans. *Front. Microbiol.* **7**, 682 (2016).
33. N. Takeshita, R. Manck, N. Grün, S. H. de Vega, R. Fischer, Interdependence of the actin and the microtubule cytoskeleton during fungal growth. *Curr. Opin. Microbiol.* **20**, 34–41 (2014).
34. A. Berepiki, A. Lichius, N. D. Read, Actin organization and dynamics in filamentous fungi. *Nat. Rev. Microbiol.* **9**, 876–887 (2011).
35. M. Kopecká, S. Kawamoto, M. Yamaguchi, A new F-actin structure in fungi: Actin ring formation around the cell nucleus of Cryptococcus neoformans. *Microscopy (Oxf.)* **62**, 295–301 (2013).
36. S. K. Walker, A. Garrill, Actin microfilaments in fungi. *Mycologist* **20**, 26–31 (2006).
37. A. Berepiki, A. Lichius, J.-Y. Shoji, J. Tilsner, N. D. Read, F-actin dynamics in Neurospora crassa. *Eukaryot. Cell* **9**, 547–557 (2010).
38. A. Lichius, A. Berepiki, N. D. Read, Form follows function–The versatile fungal cytoskeleton. *Fungal Biol.* **115**, 518–540 (2011).
39. S. Seiler, M. Plamann, The genetic basis of cellular morphogenesis in the filamentous fungus Neurospora crassa. *Mol. Biol. Cell* **14**, 4352–4364 (2003).
40. G. Steinberg, M. Schuster, The dynamic fungal cell. *Fungal Biol. Rev.* **25**, 14–37 (2011).
41. N. P. Money, Wishful thinking of turgor revisited: The mechanics of fungal growth. *Fungal Genet. Biol.* **21**, 173–187 (1997).
42. L. Y. Chen *et al*., The Arabidopsis alkaline ceramidase TOD1 is a key turgor pressure regulator in plant cells. *Nat. Commun.* **6**, 6030 (2015).
43. R. J. Howard, M. A. Ferrari, D. H. Roach, N. P. Money, Penetration of hard substrates by a fungus employing enormous turgor pressures. *Proc. Natl. Acad. Sci. U.S.A.* **88**, 11281–11284 (1991).
44. N. P. Money, R. J. Howard, Confirmation of a link between fungal pigmentation, turgor pressure, and pathogenicity using a new method of turgor measurement. *Fungal Genet. Biol.* **20**, 217–227 (1996).

45. J. K. E. Ortega, C. M. Munoz, S. E. Blakley, J. T. Truong, E. L. Ortega, Stiff mutant genes of phycomyces affect turgor pressure and wall mechanical properties to regulate elongation growth rate. *Front. Plant Sci.* **3**, 99 (2012).
46. R. R. Lew, N. N. Levina, S. K. Walker, A. Garrill, Turgor regulation in hyphal organisms. *Fungal Genet. Biol.* **41**, 1007–1015 (2004).
47. S. N. Shabala, R. R. Lew, Turgor regulation in osmotically stressed Arabidopsis epidermal root cells. Direct support for the role of inorganic ion uptake as revealed by concurrent flux and cell turgor measurements. *Plant Physiol.* **129**, 290–299 (2002).
48. P. C. Blainey, The future is now: Single-cell genomics of bacteria and archaea. *FEMS Microbiol. Rev.* **37**, 407–427 (2013).
49. F. J. H. Hol, C. Dekker, Zooming in to see the bigger picture: Microfluidic and nanofabrication tools to study bacteria. *Science* **346**, 1251821 (2014).
50. B. Libberton, M. Binz, H. van Zalinge, D. V. Nicolau, Efficiency of the flagellar propulsion of Escherichia coli in confined microfluidic geometries. *Phys. Rev. E* **99**, 012408 (2019).
51. K. Gupta *et al*., Lab-on-a-chip devices as an emerging platform for stem cell biology. *Lab Chip* **10**, 2019–2031 (2010).
52. G. Vunjak-Novakovic, D. T. Scadden, Biomimetic platforms for human stem cell research. *Cell Stem Cell* **8**, 252–261 (2011).
53. C. Agudelo, M. Packirisamy, A. Geitmann, Influence of electric fields and conductivity on pollen tube growth assessed via electrical lab-on-chip. *Sci. Rep.* **6**, 19812 (2016).
54. C. G. Agudelo *et al*., TipChip: A modular, MEMS-based platform for experimentation and phenotyping of tip-growing cells. *Plant J.* **73**, 1057–1068 (2013).
55. T. Geng *et al*., Compartmentalized microchannel array for high-throughput analysis of single cell polarized growth and dynamics. *Sci. Rep.* **5**, 16111 (2015).
56. M. Mirzaei *et al*., Microfluidic perfusion system for culturing, imaging yeast cell microarrays and rapidly exchanging media. *Lab Chip* **10**, 2449–2457 (2010).
57. A. Tayagui, Y. Sun, D. A. Collings, A. Garrill, V. Nock, An elastomeric micropillar platform for the study of protrusive forces in hyphal invasion. *Lab Chip* **17**, 3643–3653 (2017).
58. L. Xu, H. Lee, D. Jetta, K. W. Oh, Vacuum-driven power-free microfluidics utilizing the gas solubility or permeability of polydimethylsiloxane (PDMS). *Lab Chip* **15**, 3962–3979 (2015).
59. C. E. Stanley, G. Grossmann, X. CasadevallI Solvas, A. J. DeMello, Soil-on-a-chip: Microfluidic platforms for environmental organismal studies. *Lab Chip* **16**, 228–241 (2016).
60. K. L. Hanson *et al*., Fungi use efficient algorithms for the exploration of microfluidic networks. *Small* **2**, 1212–1220 (2006).
61. M. Held, C. Edwards, D. V. Nicolau, Probing the growth dynamics of Neurospora crassa with microfluidic structures. *Fungal Biol.* **115**, 493–505 (2011).
62. M. Held, A. P. Lee, C. Edwards, D. V. Nicolau, Microfluidics structures for probing the dynamic behaviour of filamentous fungi. *Microelectron. Eng.* **87**, 786–789 (2010).
63. E. Asenova, H. Y. Lin, E. Fu, D. V. Nicolau, Jr, D. V. Nicolau, Optimal fungal space searching algorithms. *IEEE Trans. Nanobioscience* **15**, 613–618 (2016).
64. S. Bartnicki-Garcia, C. E. Bracker, G. Gierz, R. López-Franco, H. Lu, Mapping the growth of fungal hyphae: Orthogonal cell wall expansion during tip growth and the role of turgor. *Biophys. J.* **79**, 2382–2390 (2000).
65. G. Gierz, S. Bartnicki-Garcia, A three-dimensional model of fungal morphogenesis based on the vesicle supply center concept. *J. Theor. Biol.* **208**, 151–164 (2001).
66. C. G. Reynaga-Peña, G. Gierz, S. Bartnicki-Garcia, Analysis of the role of the Spitzenkörper in fungal morphogenesis by computer simulation of apical branching in Aspergillus niger. *Proc. Natl. Acad. Sci. U.S.A.* **94**, 9096–9101 (1997).
67. R. Löpez-Franco, C. Bracker, Diversity and dynamics of the Spitzenkörper in growing hyphal tips of higher fungi. *Protoplasma* **195**, 90–111 (1996).
68. L. Pieuchot *et al*., Cellular subcompartments through cytoplasmic streaming. *Dev. Cell* **34**, 410–420 (2015).
69. M. Held, C. Edwards, D. V. Nicolau, "Temporal and spatial in vivo optical analysis of microtubules in Neurospora crassa" in *Progress in Biomedical Optics and Imaging–Proceedings of SPIE* (SPIE, Bellingham, WA, 2010), 75680V.
70. M. Riquelme, S. Bartnicki-Garcia, Key differences between lateral and apical branching in hyphae of Neurospora crassa. *Fungal Genet. Biol.* **41**, 842–851 (2004).
71. S. K. Walker, K. Chitcholtan, Y. Yu, G. M. Christenhusz, A. Garrill, Invasive hyphal growth: An F-actin depleted zone is associated with invasive hyphae of the oomycetes Achlya bisexualis and Phytophthora cinnamomi. *Fungal Genet. Biol.* **43**, 357–365 (2006).
72. S. Suei, A. Garrill, An F-actin-depleted zone is present at the hyphal tip of invasive hyphae of Neurospora crassa. *Protoplasma* **232**, 165–172 (2008).
73. N. Minc, A. Boudaoud, F. Chang, Mechanical forces of fission yeast growth. *Curr. Biol.* **19**, 1096–1101 (2009).
74. N. P. Money, Measurement of hyphal turgor. *Exp. Mycol.* **14**, 416–425 (1990).
75. D. V. Nicolau *et al*., Molecular motors-based micro- and nano-biocomputation devices. *Microelectron. Eng.* **83**, 1582–1588 (2006).
76. D. V. Nicolau, Jr, *et al*., Parallel computation with molecular-motor-propelled agents in nanofabricated networks. *Proc. Natl. Acad. Sci. U.S.A.* **113**, 2591–2596 (2016).
77. M. Roper, A. Simonin, P. C. Hickey, A. Leeder, N. L. Glass, Nuclear dynamics in a fungal chimera. *Proc. Natl. Acad. Sci. U.S.A.* **110**, 12875–12880 (2013).
78. L. Heaton *et al*., Analysis of fungal networks. *Fungal Biol. Rev.* **26**, 12–29 (2012).
79. D. P. Bebber, J. Hynes, P. R. Darrah, L. Boddy, M. D. Fricker, Biological solutions to transport network design. *Proc. Biol. Sci.* **274**, 2307–2315 (2007).
80. A. Tero *et al*., Rules for biologically inspired adaptive network design. *Science* **327**, 439–442 (2010).

SUPPLEMENTARY INFORMATION

Intracellular mechanisms of fungal space searching in microenvironments

Marie Held, Ondrej Kaspar, Clive Edwards, Dan V. Nicolau

1. SUPPLEMENTARY TEXT AND FIGURES

1.1. Fungal growth on flat agar surfaces, and in closed non-constraining PDMS geometries

1.1.1. Experimental system

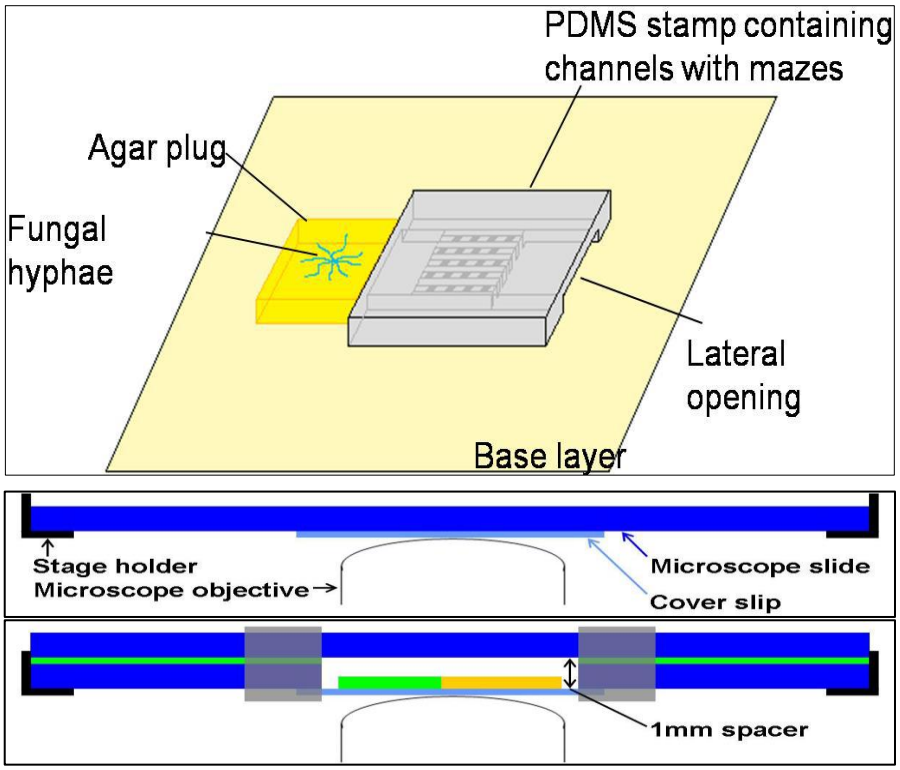

Figure S1. Top panel: top view of the overall experimental setup (optical imaging system not shown). Bottom panel: side view of the experimental implementation for fluorescence studies (not to scale). Top: Normal implementation requirements. Bottom: Experimental assembly used in this study.

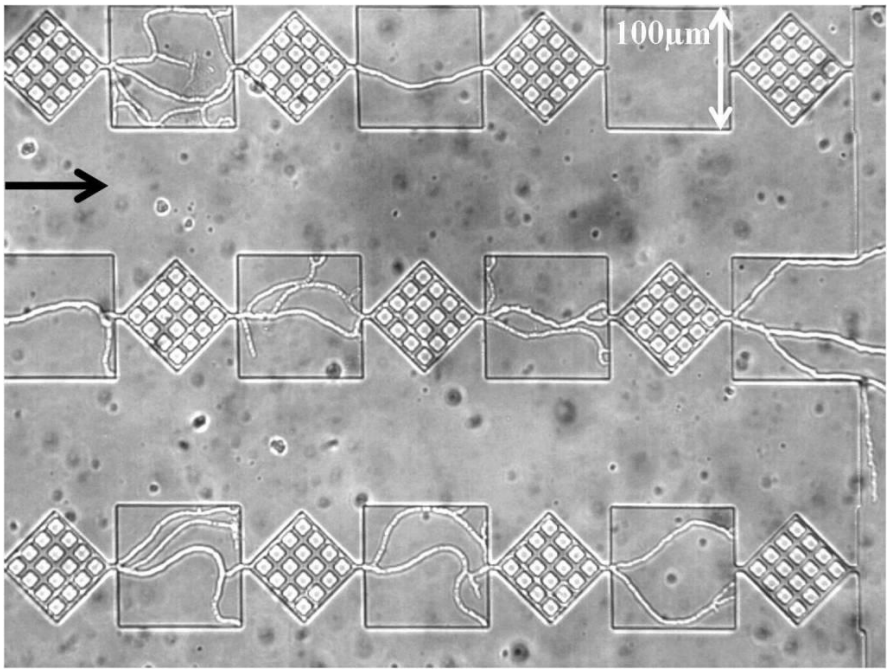

Figure S2. *Neurospora crassa* exploring in parallel a series of 100 µm-wide chambers. The black arrow indicates the direction the exploration of the set of networks. The overall trajectories of the exploring hyphae present with a trend from left to right, which is induced by the layout of the individual microfluidic networks and connecting chambers.

www.pnas.org/cgi/doi/10.1073/pnas.1816423116

1.1.2. Calculations for the design and operation of microfluidics chambers

Oxygen diffusivity. The diffusion coefficient of molecular oxygen in water can be estimated using the Stokes-Einstein equation. Assuming that water and oxygen molecules are ideally spherical and that the channel is filled arbitrarily slowly, the diffusion coefficient D of oxygen in water is

$$D = \frac{k_B T}{6\pi\eta R_0} \quad \text{Eq. 1}$$

where k_B is the Boltzmann constant, T is the absolute temperature, η is the dynamic viscosity of the solvent, and R_0 is the hydrodynamic radius of the diffusing particles. R_0 is the effective radius of the particle that experiences resistance from the viscous solution:

$$R_{0-Oxygen} = 1.21 \cdot 10^{-10} m \quad \text{Eq. 2}$$

The temperature T = 296.15 K used in the calculation corresponds to the average room temperature of 21°C measured over the duration of the experiments. The dynamic (or absolute) viscosity of water depends on T according to Arrhenius-Andrade equation

$$\eta = \eta_0 \cdot e^{\frac{E_A}{RT}} \quad \text{Eq. 3}$$

where η_0 is the material viscosity under standard conditions, E_A is an activation (or transposition) energy, and R is the absolute gas constant. Adams et al. (1) measured the T-dependence over the range 274 K < T < 373 K, yielding a simplified empirical formulation

$$\eta = A \cdot 10^{\frac{B}{T-C}} \quad \text{Eq. 4}$$

with empirical constants A = $2.414 \cdot 10^{-5}$ kg·m^{-1}·s^{-1}, B = 247.8 K, and C = 140.0 K. Therefore, the viscosity of water at average room temperature during the experiments (23°C) is

$$\eta_{296.15} = 9.33 \cdot 10^{-4} Pa \cdot s \quad \text{Eq. 5}$$

Using this viscosity, the diffusion constant of an oxygen molecule in aqueous solution is

$$D = 1.92 \cdot 10^{-9} \frac{m^2}{s} \quad \text{Eq. 6}$$

This value is less than $3.4 \cdot 10^{-9}$ m^2/s, reported in PDMS (2), which is permeable to both oxygen and carbon dioxide.

Diffusivity of nutrients. By modelling maltose and oxygen molecules as ideally spherical molecules, and assuming that the channel is filled arbitrarily slowly, the diffusion of oxygen in water can be described using the Stokes-Einstein equation. Substituting a hydrodynamic radius for maltose of $R_{0\text{-Maltose}}$ = 5 Å (3) in Eq. 1., and assuming the previously quoted values for the other constants, yields the diffusion constant

$$D_{Maltose} = 4.65 \cdot 10^{-10} \frac{m^2}{s}$$

This value is approximately four times smaller than that for oxygen (~ 2×10^{-9} m^2/s). The time needed for the maltose to diffuse a distance x ~ 100 µm (the length between the test structure, e.g., diamond, and larger volumes of nutrients, e.g., opening or 100 µm x 100 µm 'plazas') can thus be calculated as

$$t = \frac{\langle x^2 \rangle}{2 \cdot D_{Maltose}} = \frac{100^2 \cdot 10^{-12}\, m^2}{2 \cdot 4.651 \cdot 10^{-10} \frac{m^2}{s}} = 10.75\, s$$

This time is three orders of magnitude shorter than the time taken by a typical apical extension of *Neurospora crassa* to traverse the test structure, assuming an average extension velocity of ~ 0.006 µm/s. In conclusion, the microfluidics structures provide rapid and high level of nutrients, thus not impacting on fungal growth.

Table S1. Relevant parameters for the operation of fungal confinement chips

Medium	Diffusivity of O_2 (m^2/s)	Diffusivity of sugars (m^2/s)
Air	$1.8 \cdot 10^{-5}$	-
Water	$1.9 \cdot 10^{-9}$	$4.7 \cdot 10^{-10}$ for maltose, cf. above
Agar	$2.4 \cdot 10^{-9}$, 2% agar (4)	$2.9 \cdot 10^{-10}$ for sucrose (5)
PDMS	$3.4 \cdot 10^{-9}$ (2)	-

1.1.3. Penetration depth of *Neurospora crassa* hyphae into an agar plate

The fungal growth on flat agar surfaces benefits from unencumbered access to oxygen. In contrast, the oxygen needs to diffuse through PDMS to the hyphae growing in closed, but non-constraining environments, or through the aqueous solutions in the microfluidics channels. It appears however that the lower oxygen content in closed but non-confining PDMS structures, compared with the open agar surfaces, does not affect hyphal growth. Indeed, the following images show vertical cross-sections of an agar plate, onto which a fungal colony has been inoculated. Fungal growth then occurs on, or at a shallow depth below the surface, but there is also some deeper penetration, beyond the accessible range of a confocal microscope.

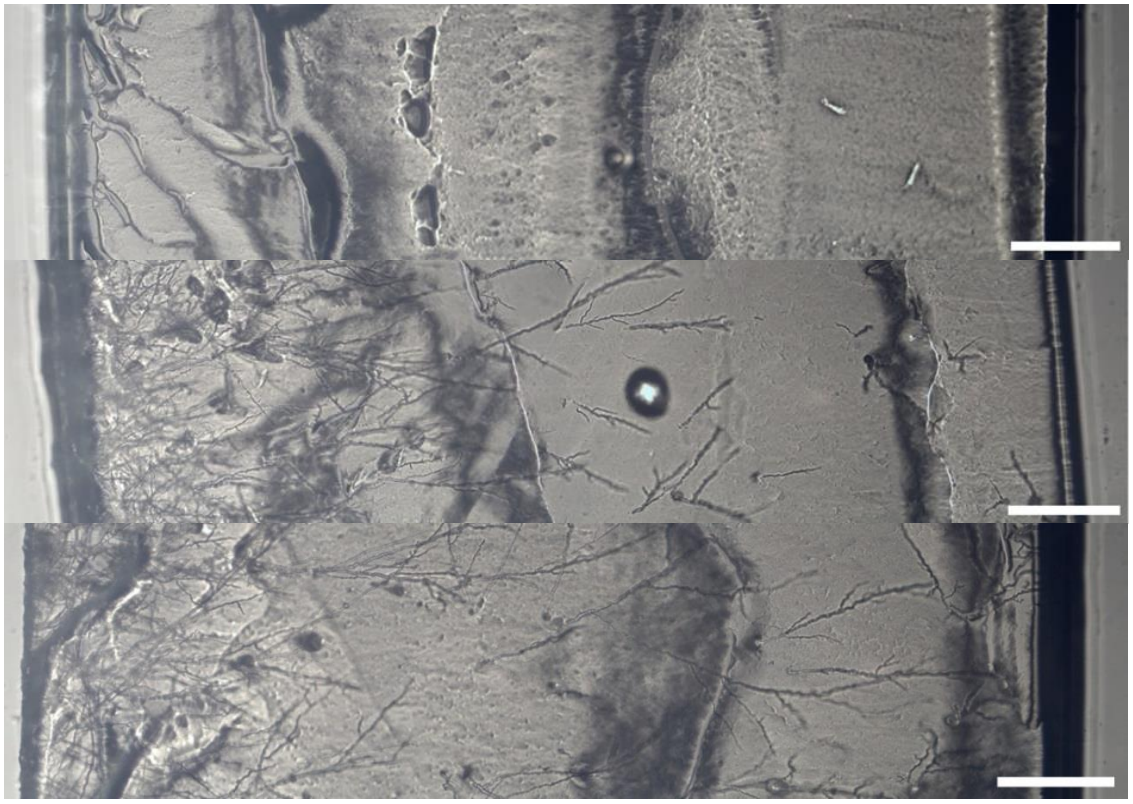

Figure S3. Micrographs of the hyphal vertical penetration in agar material. Sections away from the edge of the agar plug: top: at the edge (penetration depth of the bulk of hyphae ~80 μm); middle: 0.5 cm from the edge (penetration depth ~670 μm); and bottom: 1 cm from the edge (penetration depth ~approximately 2260 μm). In the middle of the agar plate, the fungus penetrates the entire depth of the agar plate, i.e., more than 2 mm. The scale bar = 500 μm.

1.1.4. Equivalence between conditions of growth on agar and in control PDMS chambers

The environments presented to hyphae by agar surfaces and PDMS structures are not geometrically similar, raising the possibility of differences in fungal growth. First, the hyphae growing on agar are not physically constrained, as they could even penetrate it for more than 2 mm. However, the PDMS structures used to study the intracellular mechanisms in quasi-

open conditions consist of chambers with widths of 100 µm and heights of 10 µm, which exceeds the diameters of a typical *Neurospora crassa* hypha, i.e., 4-7 µm, consequently excluding physical constraining. Second, on agar the hyphae are directly exposed to air, but in experiments in closed/non-confining environments, the oxygen reaches the hyphae through diffusion through microns-to-millimetres thick PDMS material. Although the diffusivity of oxygen in air ($1.8 \cdot 10^{-5}$ m^2 s^{-1}) is approximately four order of magnitude higher than in PDMS ($3.4 \cdot 10^{-9}$ m^2 s^{-1} (6)), the capacity of hyphae to penetrate agar, which has a lower diffusivity of oxygen ($2.4 \cdot 10^{-9}$ m^2 s^{-1}) than PDMS, suggests that oxygen is present at levels not impacting fungal growth. Third, the diffusivity of sugars in water (the carrier of nutrients for in closed/non-confining PDMS structures) is estimated at $4.7 \cdot 10^{-9}$ m^2 s^{-1}, which is more than an order of magnitude higher than for agar, i.e., $2.9 \cdot 10^{-10}$ m^2 s^{-1}, which suggests that nutrient levels will not negatively affect fungal growth.

1.1.5. Intracellular mechanisms for *Neurospora crassa* growth on external and internal control

Hyphal growth behaviour and related intracellular processes in PDMS non-constraining environments are similar with those observed on agar (Supplementary Figure S2). First, the cross-sectional apical profiles of Neurospora crassa hyphae are parabolic and symmetrical (Figure 2a for internal control; Supplementary Figure S4 for external control). Second, the Spitzenkörper is centred at the hyphal apex (Supplementary Movie S1, and Supplementary Figure S5), with small periodic oscillations orthogonal to the direction of growth (Supplementary Movie S2). Third, the microtubules are predominantly orientated parallel to the longitudinal hyphal axis (Figure 2a for internal control; Supplementary Figures S4 and S6 for external control). For instance, in the apical regions, a majority of microtubules (53%) deviate by less than 10° from the polarisation axis, and 84% deviate by less than 20°, with an overall mean deviation angle of 11.7° ± 9.5° (n = 453 microtubules measured in 20 hyphae, Figure 2b, Supplementary Movie S3). By contrast, in subapical compartments the angular deviations of microtubules are larger, i.e., 21% microtubules presenting a deviation of less than 10°, and 46% less than 20°, with an overall mean deviation angle of 26.8 ± 20.1° (n = 852 microtubules measured in 20 hyphae; Figure 2b and Supplementary Movie S4).

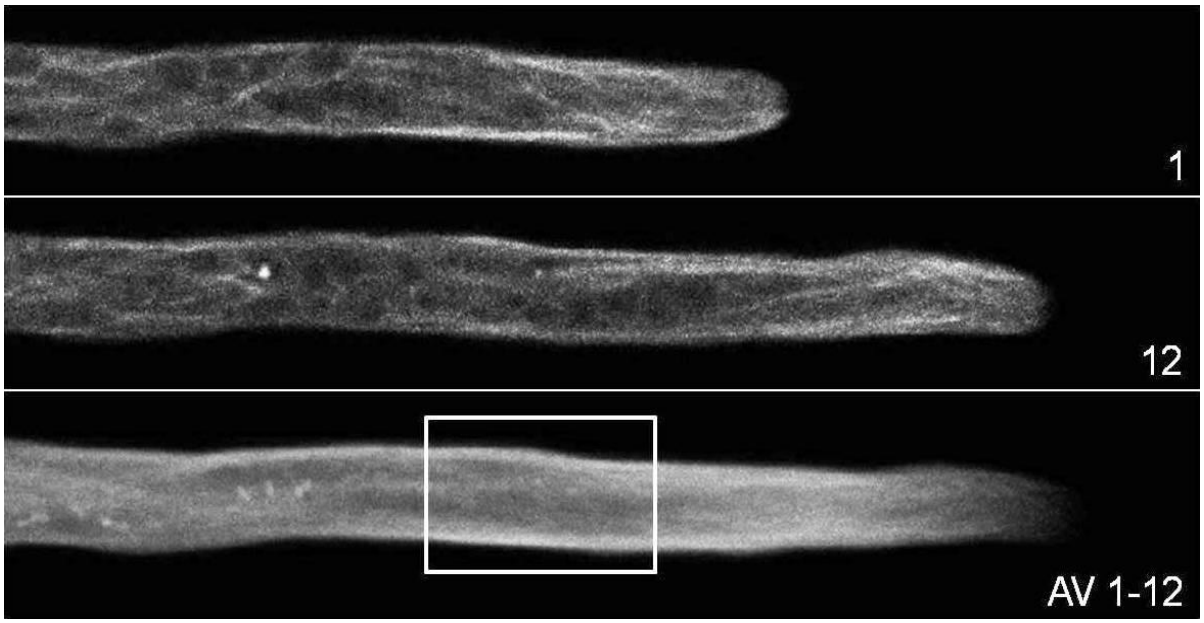

Figure S4. Hypha profile and distribution of the microtubules (fluorescently tagged) within growing hypha. Top: First and last frame and overlay of an image series of the fluorescence signal of *Neurospora crassa* GFP on agar. The spatial distribution of the microtubules (presented further in Figure S7) is quantified in the indicated rectangle.

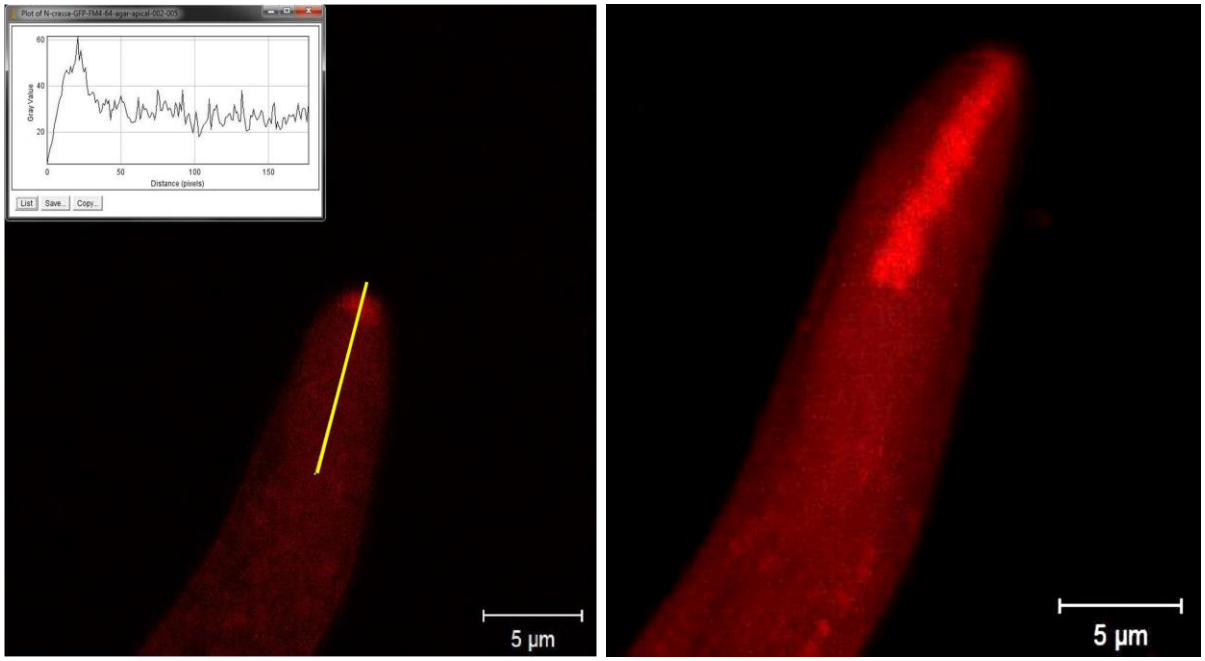

Figure S5. FM4-64 intensity profile and Spitzenkörper trajectory in the apical compartment of *Neurospora crassa* GFP on agar. Left: Apical compartment of a *Neurospora crassa* GFP hypha loaded with FM4-64 and grown on agar. The yellow line indicates the line along which the intensity profile (inset) was recorded. The abscissa correlates to the line starting at the top end, which lies outside the hypha. Following the profile, the intensity spikes at the location of the Spitzenkörper and then decreases rapidly to the constant moderate intensity level of the hyphal cytoplasm. Right: Overlay of the maximum intensities of 23 images of a time series showing the Spitzenkörper in the apical compartment. Images were recorded at intervals of 3.15 s. The overlay resulted in a pronounced trajectory of the Spitzenkörper. The intensity decrease of the trajectory was caused by photobleaching.

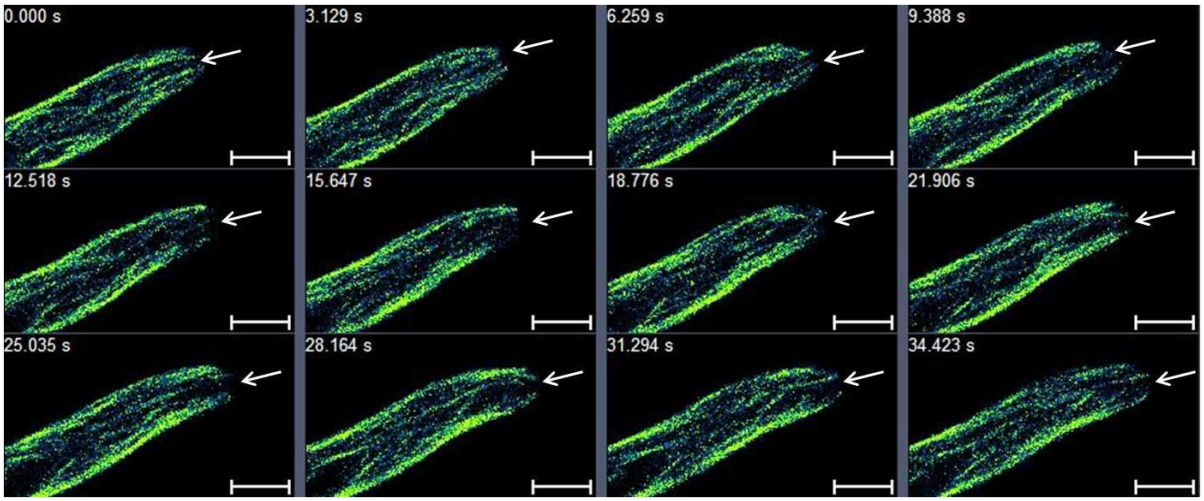

F**igure S6**. Time series of the microtubule distribution in a *Neuropsora crassa* GFP hypha growing on plain agar. The images were recorded in intervals of 3:1 s. The white arrows mark the 'voids' of the microtubule distributions near the apical cell wall correlating with the position of the Spitzenkörper (identified in simultaneously recorded bright field images). Scale bar: 5 µm

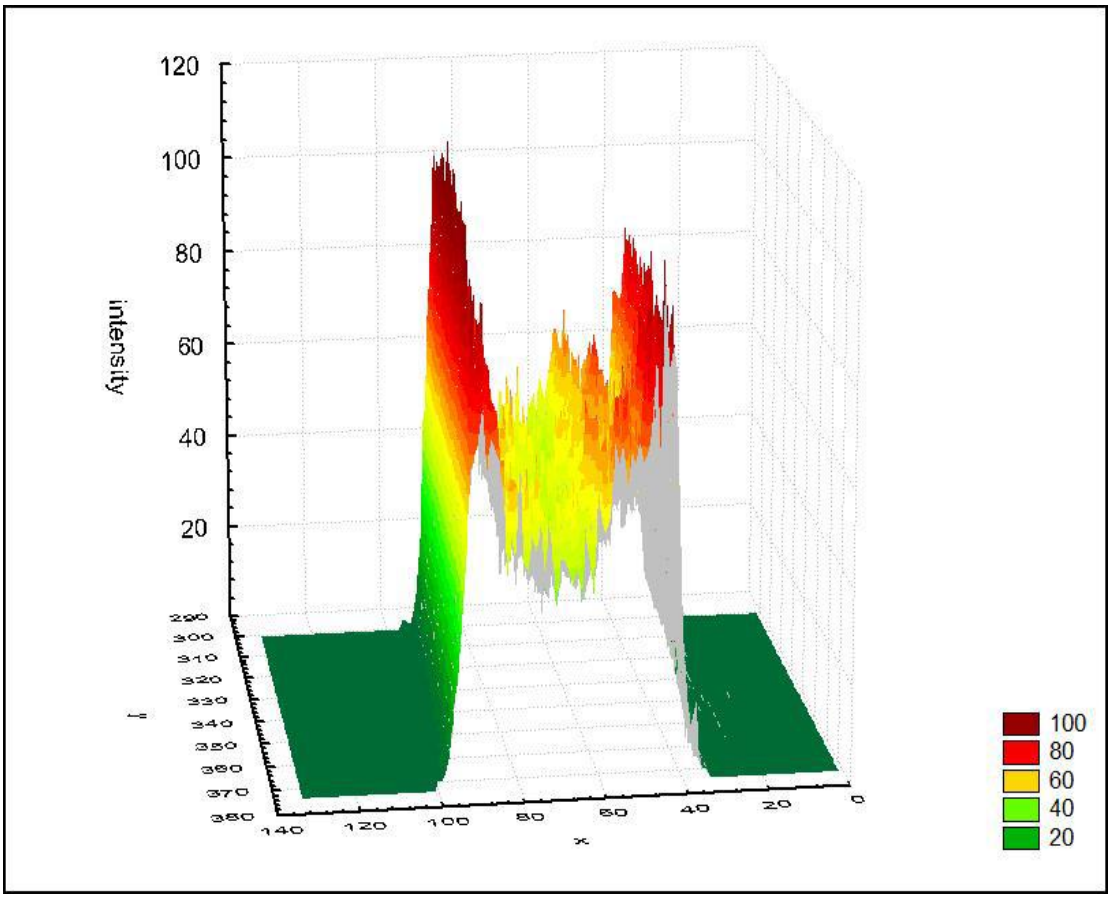

Figure S7. 3D representation of the average intensity values due to microtubules in the marked box in the overlay image in Figure S4. Both representations show that the microtubule distribution across the cross section of the hypha is inhomogeneous characterised by an accumulation of filaments close to the hyphal cell wall.

The following histograms present the spatial distributions of the microtubule relative to the hyphal polarisation axis, in the apical and sub-apical compartments; and in agar and microfluidic environments.

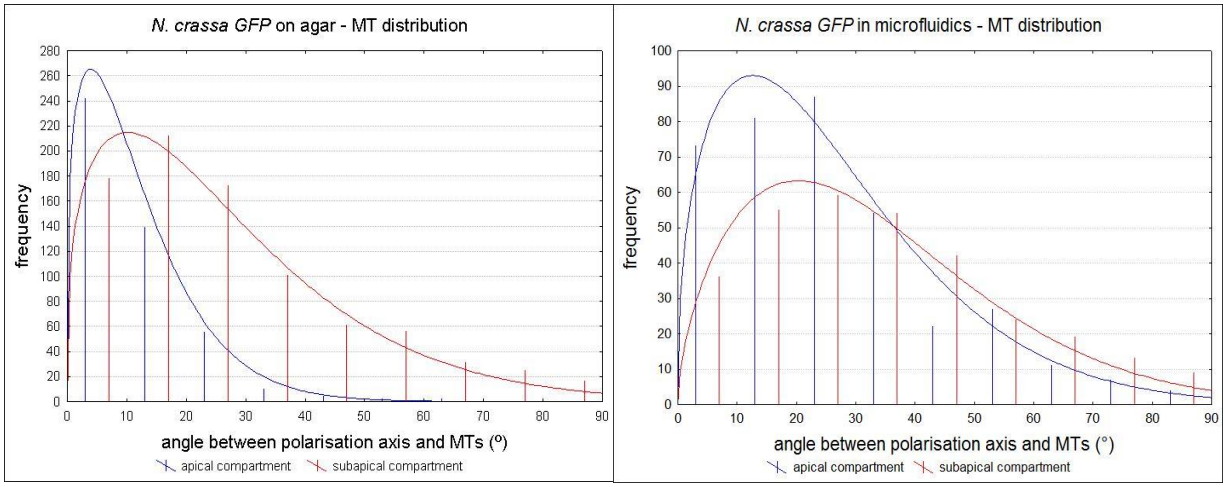

Figure S8. Statistical distributions of microtubules for hyphae growing on/in agar, and on PDMS microfluidics, respectively, in the apical, and subapical regions of the hyphae.

Table S2. Microtubule orientation on agar and in confined spaces

Interval	Agar		Microfluidics	
	Apical	Subapical	Apical	Subapical
0° to 10°	53%	21%	20%	12%
0° to 20°	84%	46%	69%	29%
0° to 80°	100%	98%	99%	97%
45° to 90°	1%	18%	16%	26%

This statistical analysis of the orientation of the microtubules shows that, aside from minor shifts of alignment versus the hyphal axis in closed/non-constraining environments compared with hyphae on agar (from ~5° to 12° in the apical compartment; and from 10° to 20° for subapical compartment), the distribution of microtubules has a clear propensity towards hyphal walls in both experimental conditions.

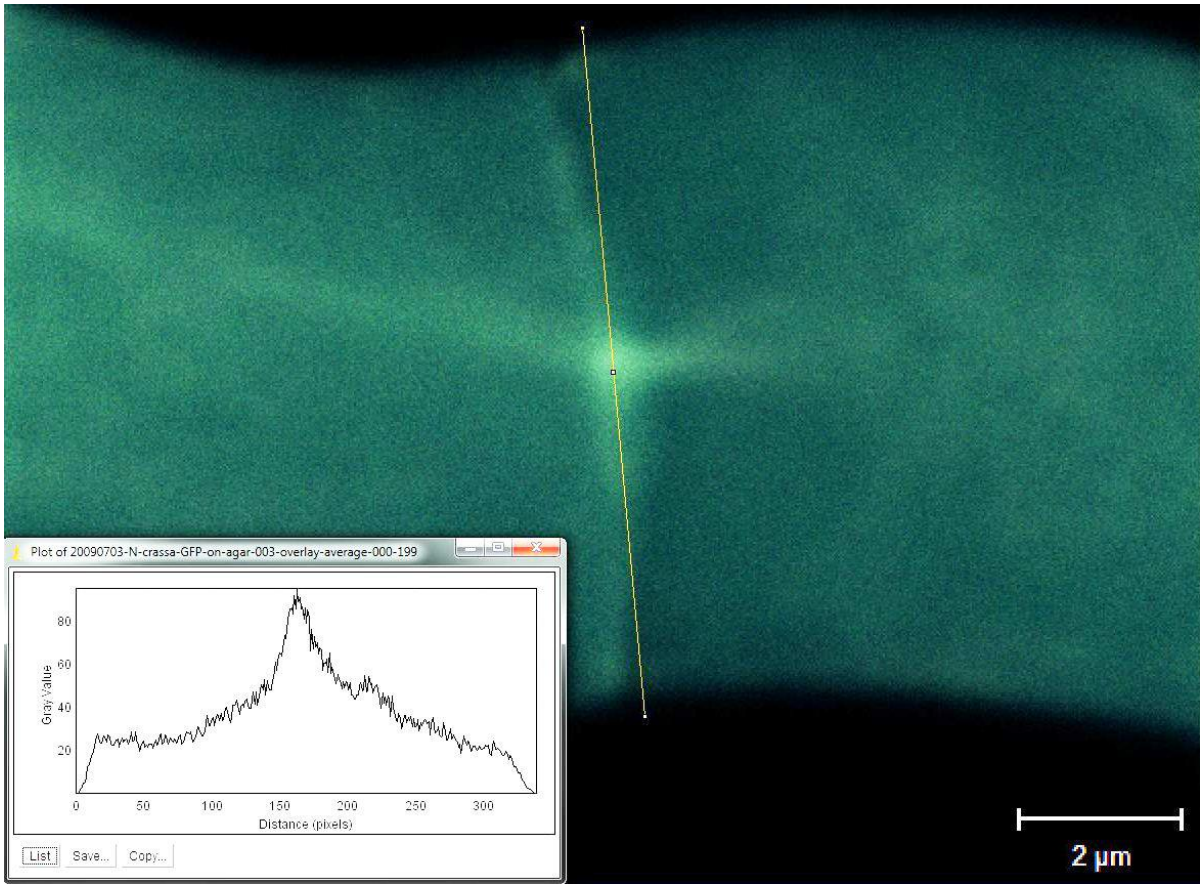

Figure S9. Microtubules passing through a septum placed centrally in the hypha (average over 200 images). The graph in the inset represents the profile of the intensity values along the indicated yellow line.

1.1.6. Intracellular mechanisms of branching for external and internal controls

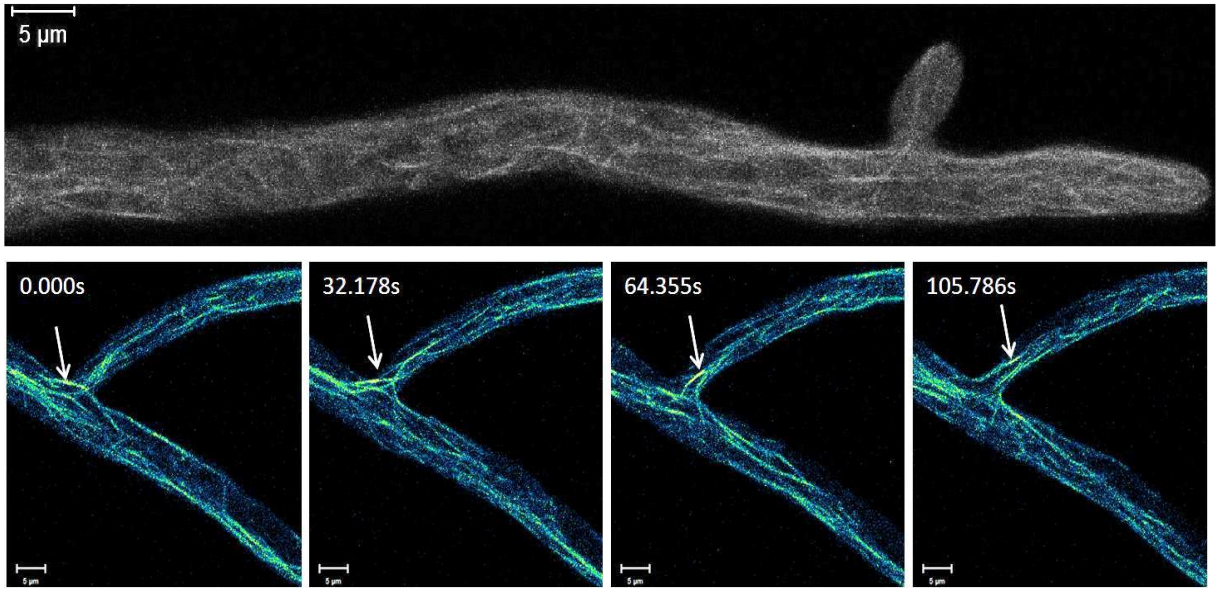

Figure S10. Top: Branching at 45° in *Neurospora crassa* GFP on agar. Bottom: Time series of the microtubule distribution at an established branching point in a *Neuropsora crassa* GFP hypha growing on agar. The white arrows mark the position of a microtubule moving from the parent hypha into the daughter hypha. Scale bar: 5 µm.

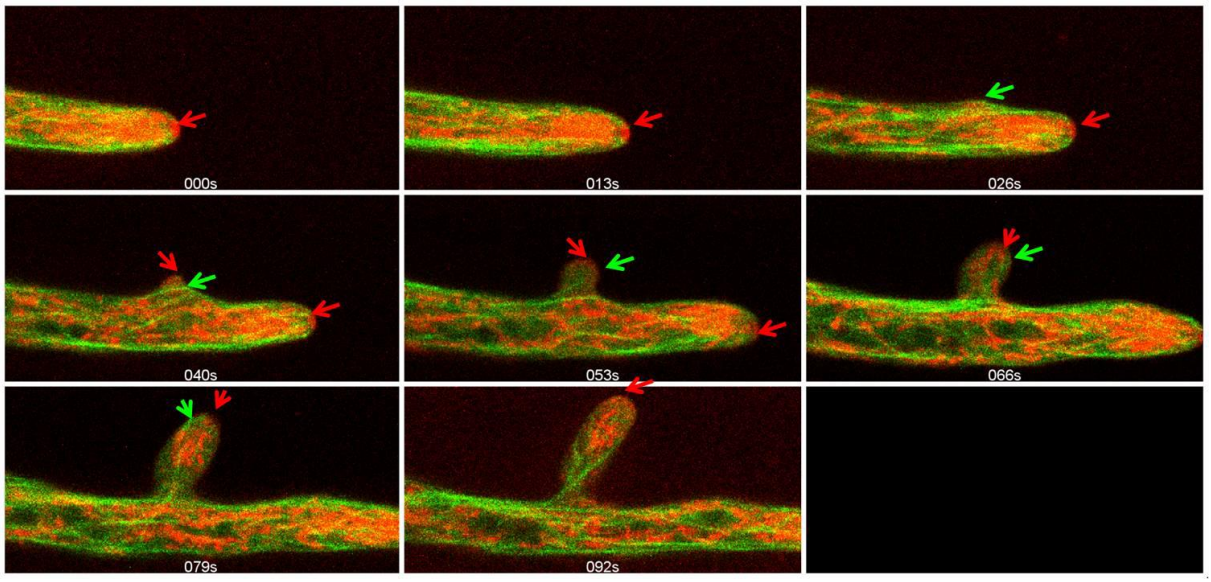

Figure S11. Formation of a lateral branch in non-constraining PDMS structures. Overlay of the fluorescence signal of the microtubules and Spitzenkörper during a branching event. The red arrows indicate the Spitzenkörper and the green arrows indicate the microtubules terminating at the point of hyphal formation (26s) and that extend from the parent into the forming branch (40s - 90s). The hyphal diameter is 4.9 µm.

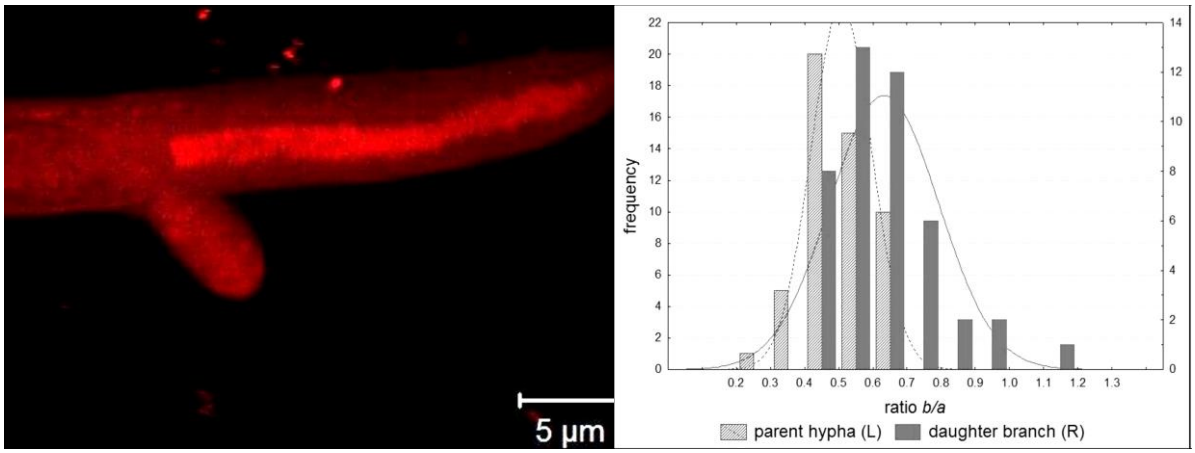

Figure S12. Branching event in a *Neurospora crassa* hypha on agar. Left: Overlay of the maximum intensities of 68 images of Spitzenkörper movement during branching (images were recorded at 5.76s intervals). Spitzenkörper trajectory in the daughter hypha is less clear than that for the parental hyphae due to its movement out of the focal plane, e.g., penetrating agar. Right: Distribution of the Spitzenkörper ellipsoid axis ratios in the parent and the daughter branch. The average ratios are 0.50 and 0.62.

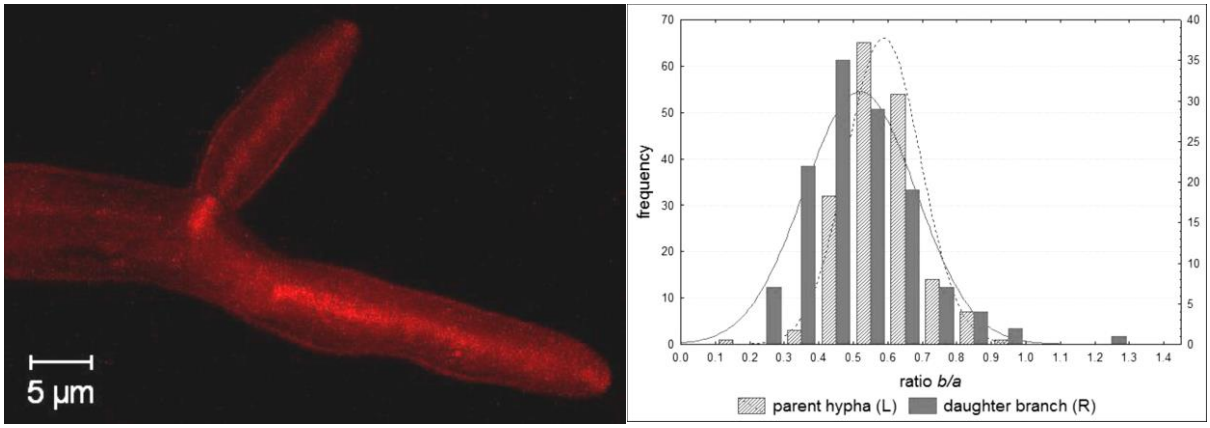

Figure S13. Branching events in FM4-64 loaded *Neurospora crassa* GFP hyphae in wide PDMS channels. Left: Overlay of the maximum intensities of 100 images of a time series depicting the Spitzenkörper motilities during the formation of a branch in a wide PDMS channel. The images were recorded at intervals of 3.9 s. Right: Distribution of the Spitzenkörper ellipsoid axes in the parent and the daughter branch. The average ratios of the short and the long axes are 0.57 for the parent hypha and 0.51 for the daughter hyphae.

1.2. Collision with obstacles at acute angles of approach

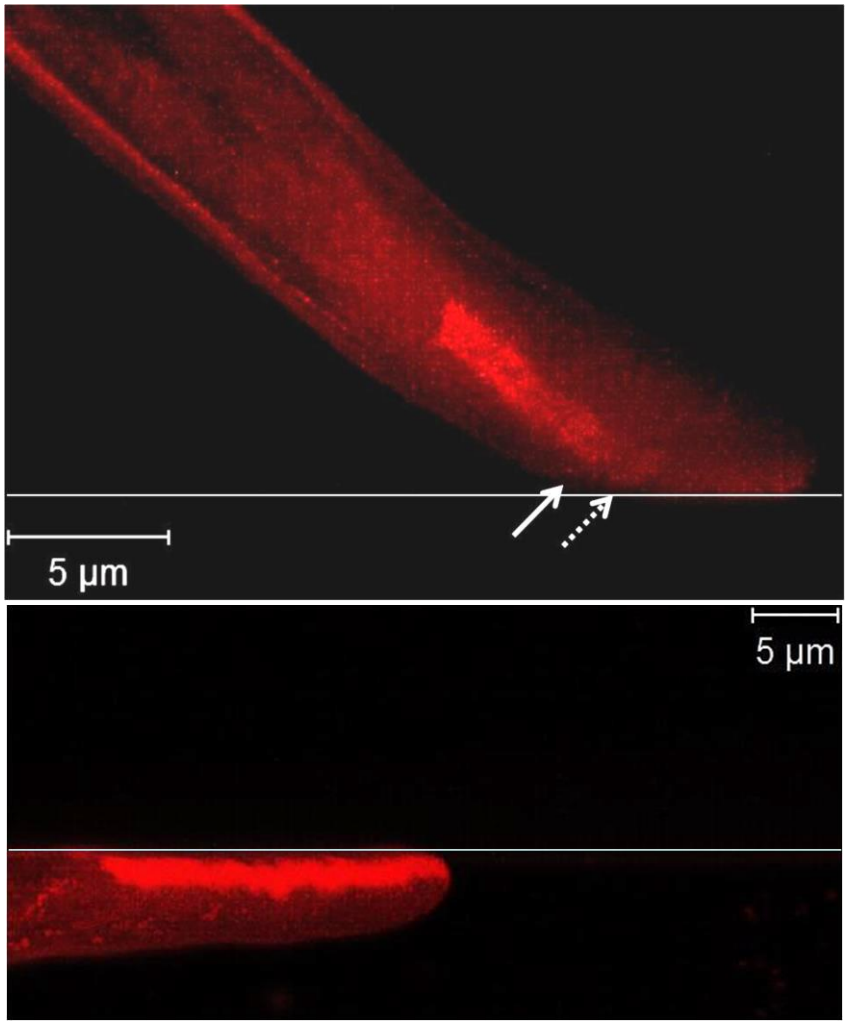

Figure S14. Spitzenkörper trajectories during adaptation and the 'nestling' processes. The solid line in both images indicates the impeding PDMS wall. The solid arrow in the top panel indicates the point where the Spitzenkörper trajectory starts to deviate from the hyphal polarisation axis and the dashed arrow indicates the point where the trajectory aligns parallel to the geometry. Top: Overlay of the maximum intensities of 67 images of a time series depicting the adaption of a hyphal apex to the geometry. The images were recorded at intervals of 4.3 s. The gradual decrease in intensity was caused by photobleaching. Bottom: Overlay of the maximum intensities of 144 images of a time series depicting continuous hyphal 'nestling' to the confining wall. The images were recorded at intervals of 7:4 s. The Spitzenkörper trajectory is permanently dislocated from the central axis of the hypha towards the geometry.

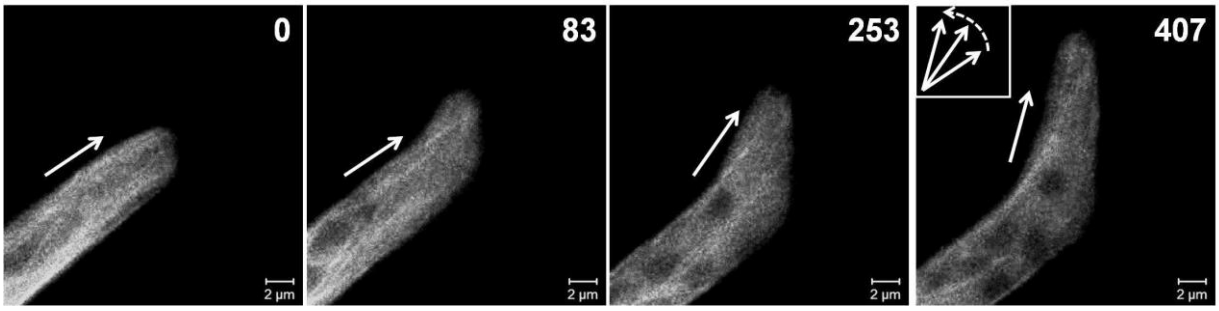

Figure S15. Microtubules in *Neurospora crassa* GFP during 'nestling'. The numbers indicate the elapsed time in seconds. The arrows indicate the direction of the leading microtubules in the apical region. The overlaid arrows in the inset at 407 s represent the change in the direction of the microtubules over the four depicted frames. The reduction in overall intensity was due to photo bleaching effects during the long-term observation.

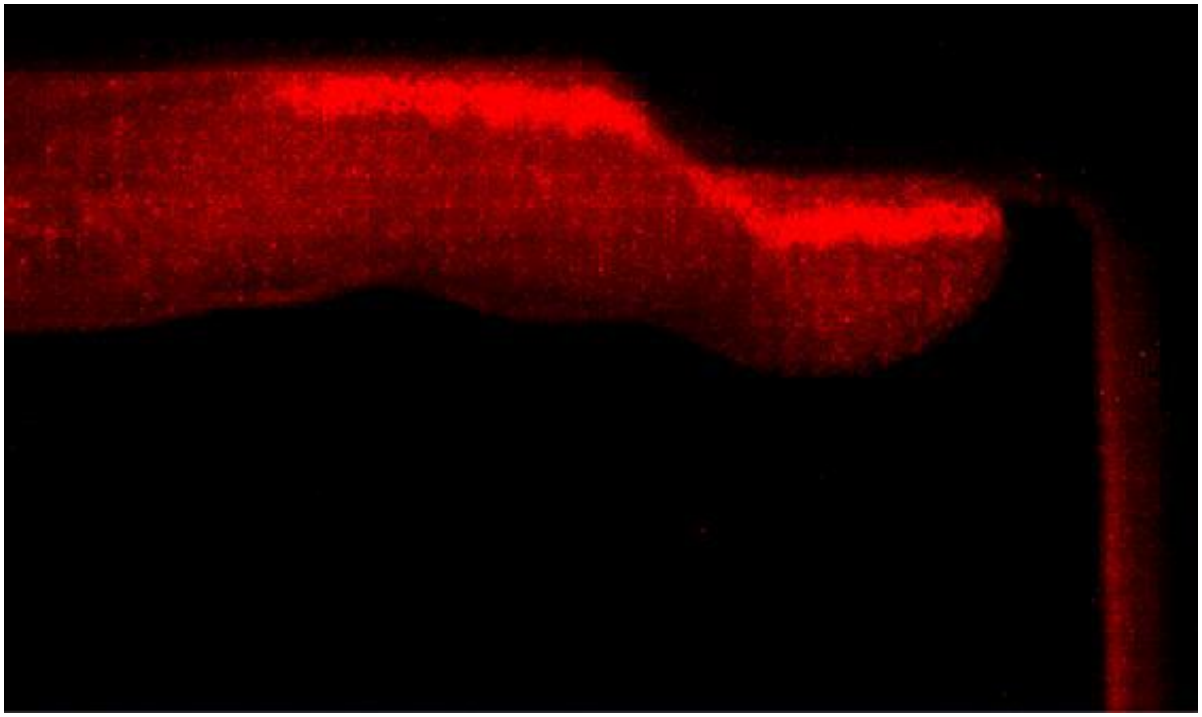

Figure S16. Spitzenkörper motility during 'nestling'. Overlay of the maximum intensities of 166 images of a time series depicting a successful corner turn. The images were recorded at intervals of 25.4 s. The Spitzenkörper remained located close to the confining geometry in the direction closest to the directional memory.

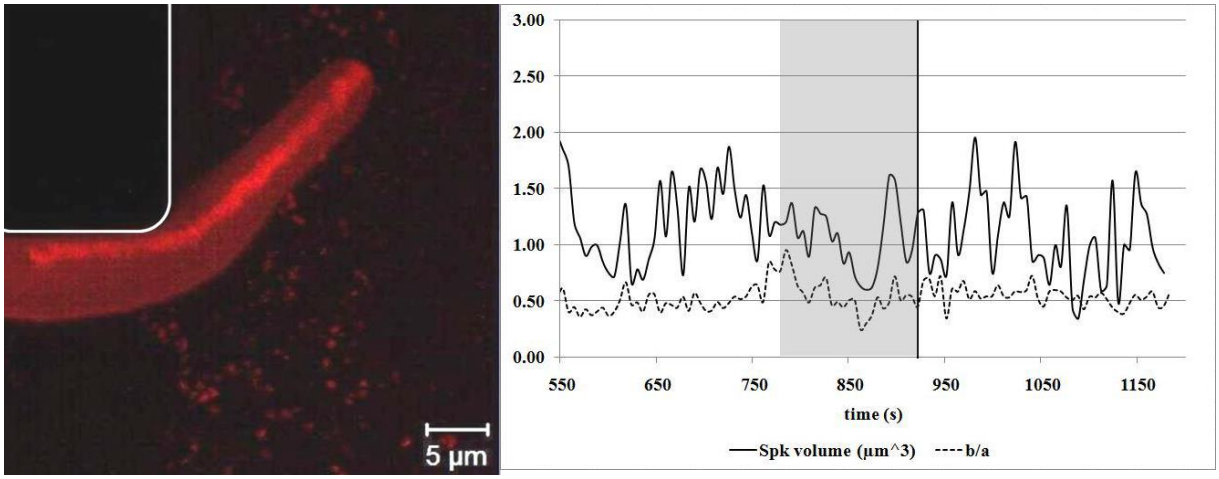

Figure S17. Spitzenkörper trajectory. Left: Overlay of the maximum intensities of 76 images of Spitzenkörper trajectory during the re-adaption to the initial growth direction after deviation by an obstacle (90 corner, white line). The images were recorded at 5.9 s intervals. Right: Time course of the Spitzenkörper volume and the ratio of the ellipsoid axes (b/a) from 550 s to 1200 s in the time series on the left. The grey highlighted area indicates the transition phase from attachment and adaptation to the geometry to the re-adaption of the initial growth direction. The solid black line indicates the time of detachment from the rounded corner.

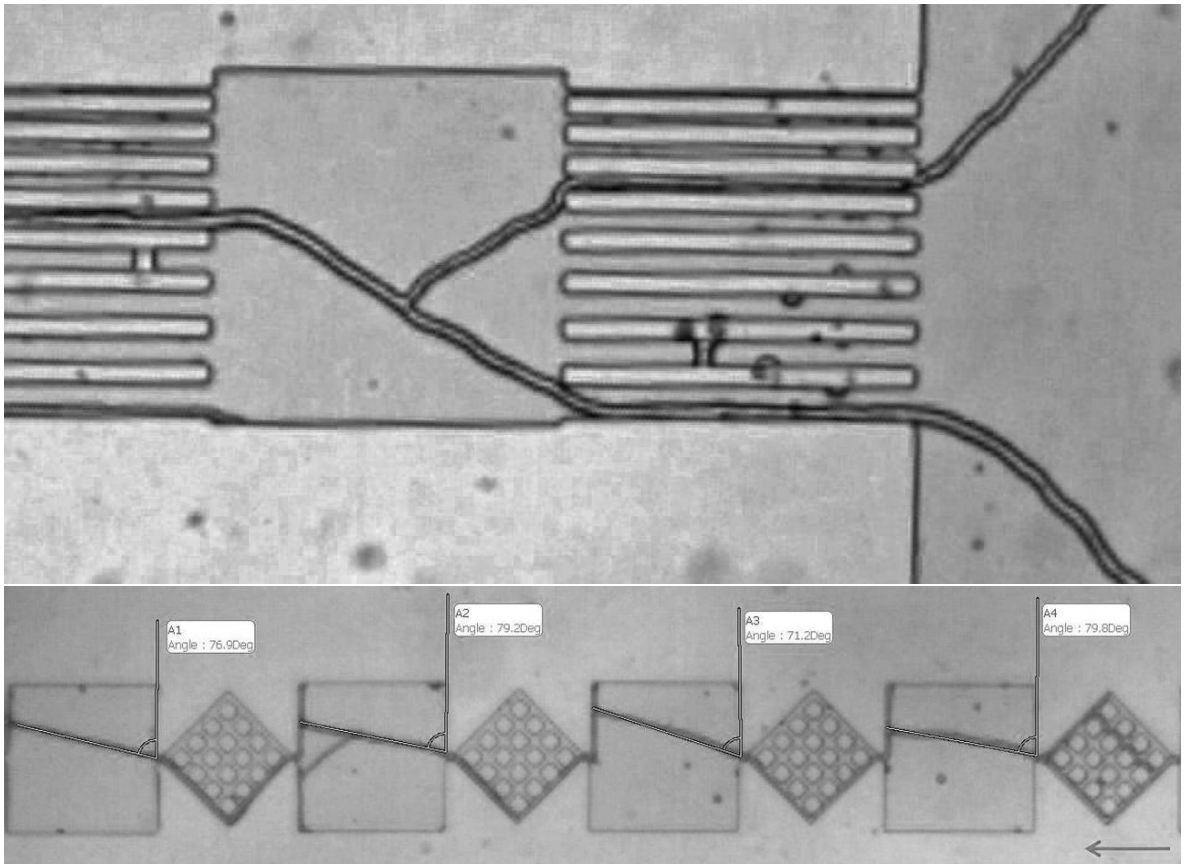

Figure S18. Several instances of the manifestation of directional memory. Top: Both parental (lower side of the image) and the daughter hypha (higher side of the image) preserve their initial direction when the geometry (straight narrow channels) allows it. Bottom: Initial direction of growth is preserved for approximately 800 µm during passage through four diamond and four plaza structures.

1.3. Frontal collision with obstacles

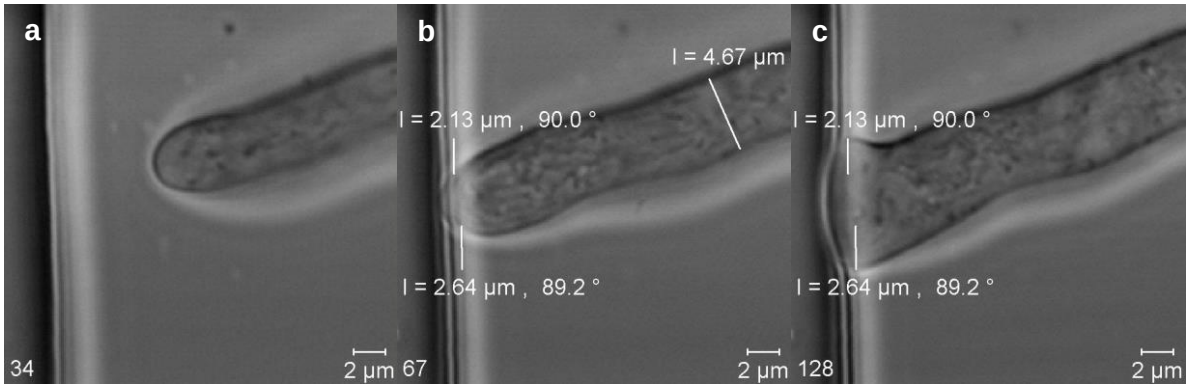

Figure S19. Parameters of the apical split indicated in selected images of a time series of a *Neurospora crassa* GFP hypha colliding head-on with a PDMS wall. The numbers in the bottom left corner indicate the number of the frame in the image series. Left: Frame 34 of an apical split image series. The hypha approaches the PDMS wall on the left head-on. Middle: Frame 67 of an apical split image series. This frame marks the beginning of the collision incident because the hypha is the closest to the wall without any distortions in the apical cell wall. The hyphal diameter is measured in the beginning frame for all collision events. The two distances measured parallel to the wall at the apex indicate the difference of the cell wall position in this beginning and the end frame. Right: Frame 128 of an apical split image series. This frame marks the end of the collision incident because this is the last frame in which the hyphal extension is characterised by uniform bulging. In the succeeding frames, the extension is characterised by the directed extension of the two initiated daughter branches away from the collision point. The two distances measured parallel to the wall at the apex indicate the difference of the cell wall position in this end and the beginning frame of the image series.

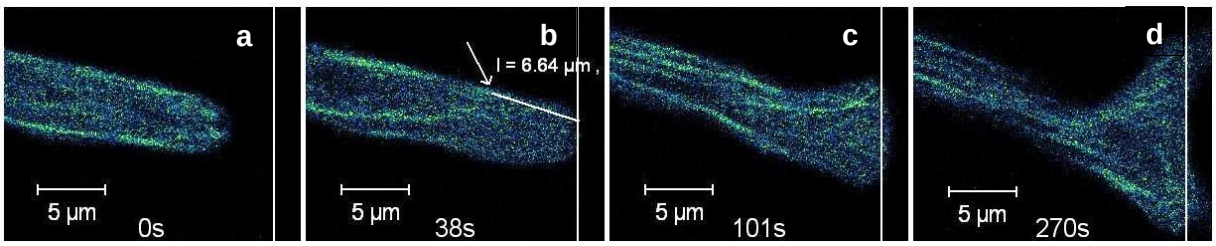

Figure S20. Microtubules in *Neurospora crassa* GFP during 'hit & split'. The white vertical line indicates the PDMS wall the hypha collided with. At 0 s, the microtubules extended up to the cell wall of the apical dome and were aligned mostly parallel to the growth axis. The second image was recorded 19 s after the collision, which represents the maximum retraction of microtubules of 6.6 µm from the collision point, indicated by the arrow. The frame at 101 s represents the snapshot with the maximum extension of the bulges, which marks the transition to polarised growth of the forming daughter hyphae. The microtubules resumed extension to the apical dome. The frame at 270 s represents an example of the established microtubule distributions in the daughter hyphae.

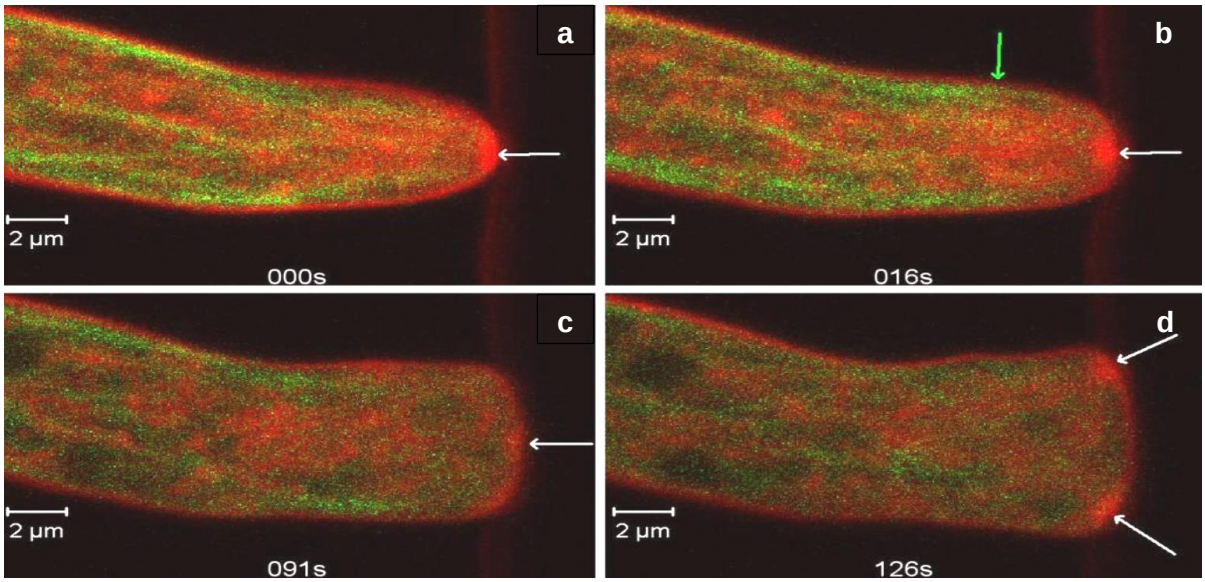

Figure S21. Motility of microtubules and Spitzenkörper during apical hit & split. Four frames of a time series taken during an apical split showing the overlay of the GFP and FM4-64 signals. The selected frames depict the times of collision, maximum distance of the receding microtubules, Spitzenkörper disintegration and establishment of daughter polarisation axes. The white arrows indicate the Spitzenkörper in the individual frames and the green arrow indicates the maximum distance the microtubules receded to. Unfortunately, the GFP signal underwent significant photobleaching and differentiation of features decreased.

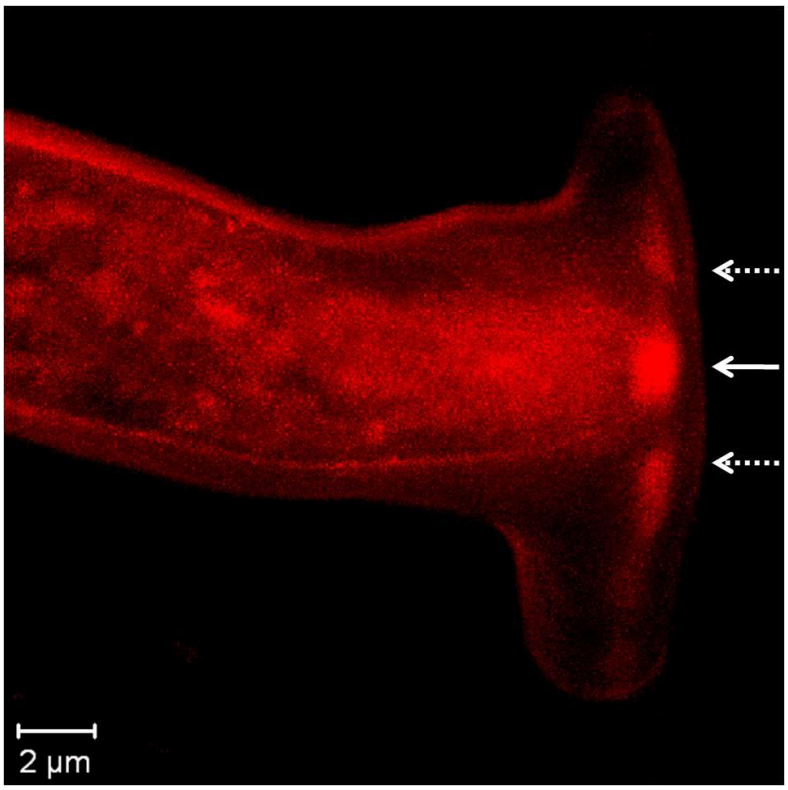

Figure S22. Spitzenkörper trajectories during an apical 'hit & split' *in Neurospora crassa*. Overlay of the maximum intensities of 135 images of a time series depicting the Spitzenkörper motility during collision-induced apical splitting process. The images were recorded at intervals of 4 s. The solid arrows indicate the trajectories of the parent Spitzenkörper and the dashed arrows indicate the trajectories of the daughter Spitzenkörper.

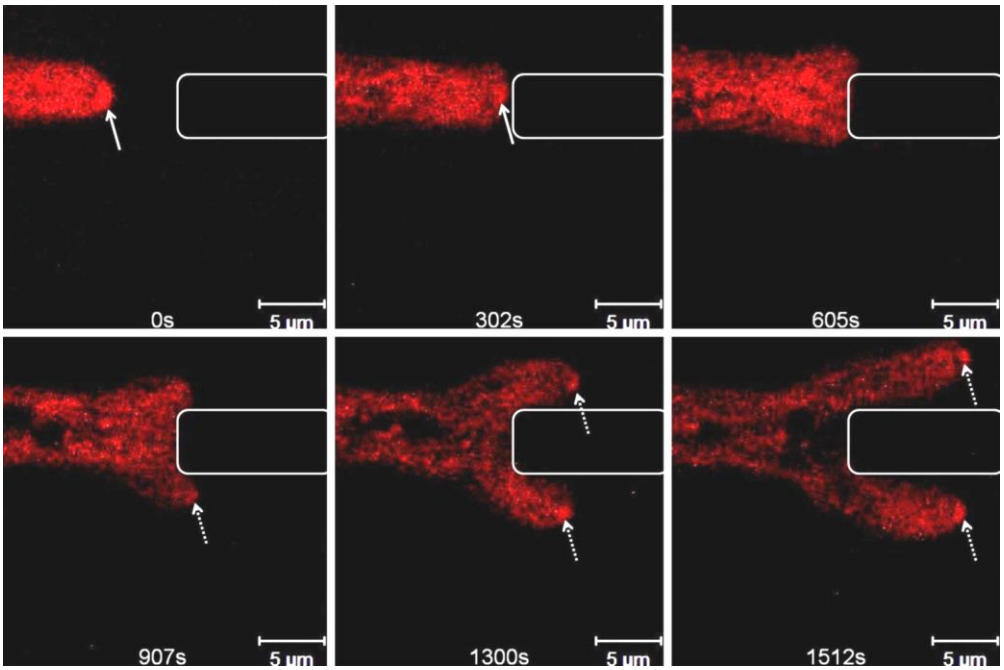

Figure S23. Apical split caused by a head-on collision of a hypha with a PDMS wall dividing individual channels. The solid arrows indicate the parent Spitzenkörper and the dashed arrows indicate the daughter Spitzenkörper.

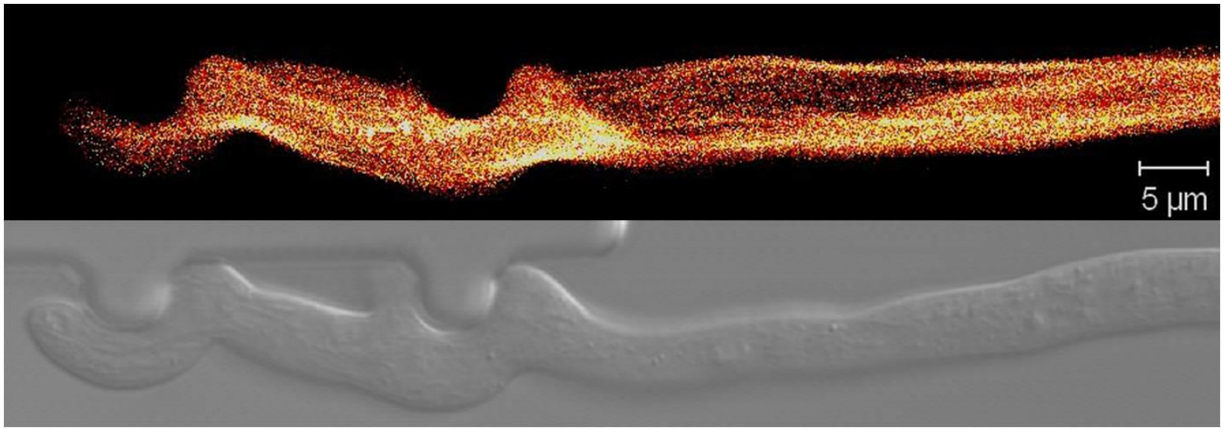

Figure S24. Top: Microtubules in *Neurospora crassa* GFP passing a string of lateral obstacles. Average calculated from 63 images recorded at 11:6 s intervals. Bottom: final snapshot. The microtubule distribution is asymmetric with peaks along the shortest path.

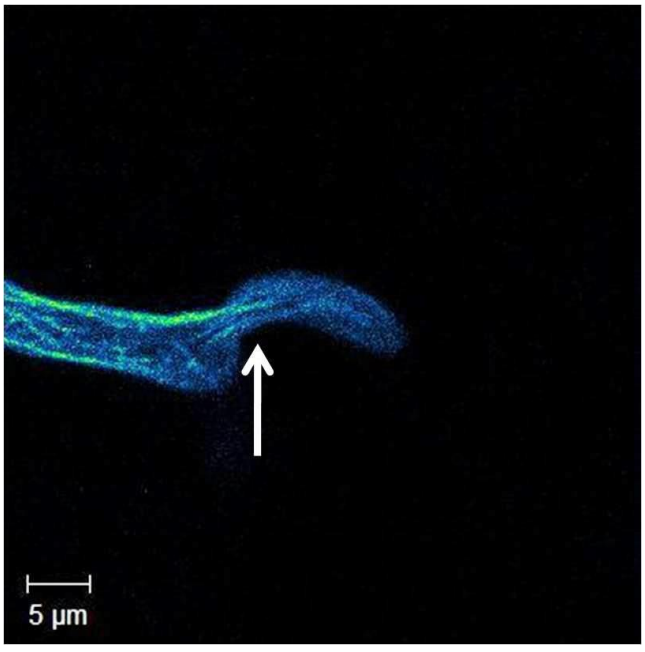

Figure S25. Detail of the distribution of microtubules distribution and intensity drop in the apical compartment of *Neurospora crassa* GFP when a hypha collided with an obstacle at near-orthogonal angle, but able to circumvent it, similarly with the above Fig. S24. The contact with the obstacle is indicated by the white arrow.

1.4. Growth and branching in tightly constraining geometries

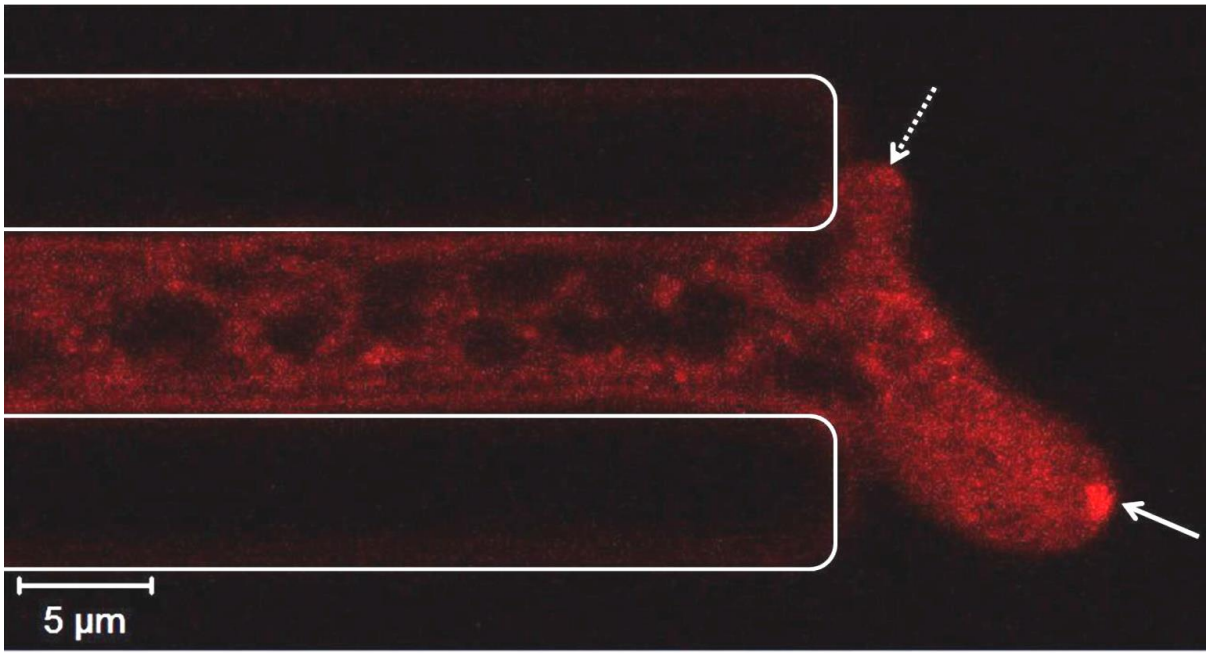

Figure S26. Spitzenkörper mobility and location during branching into channel openings and after bottlenecks. Single focal plane image of a hypha branching after exiting a 5 µm wide channel. The location of the confining PDMS walls is indicated by white outlines.

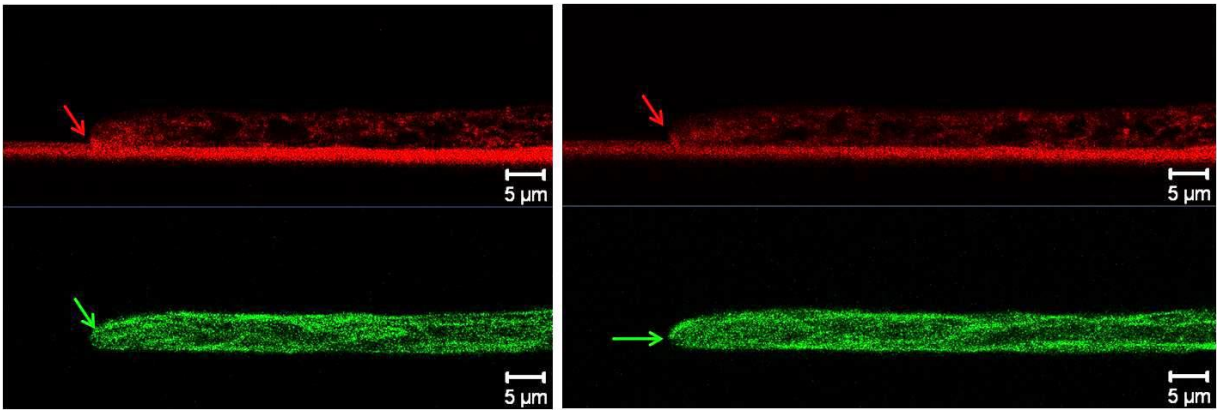

Figure S27. Microtubule distribution (green) and Spitzenkörper (red) locations during 'nestling' in tightly-constraining channels. The hyphae entered the channel from the "North", thus pressing on the "South" edge of the channels. The red arrows indicate the Spitzenkörper in both frames. The green arrows indicate the foremost microtubules in the apical dome.

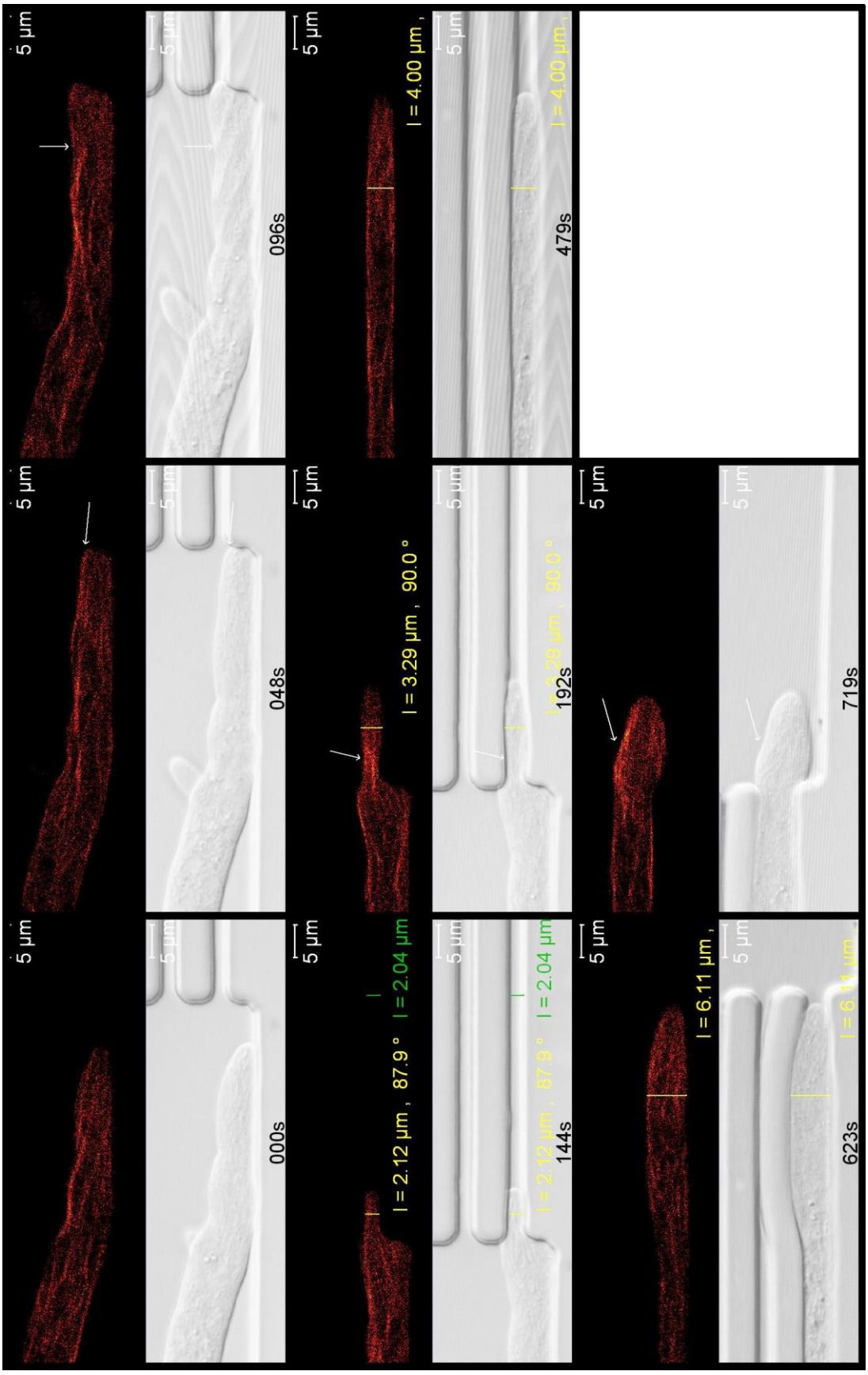

Figure S28. Microtubules in *Neurospora crassa* GFP during the penetration of a 2µm wide channel. The yellow lines indicate the hyphal widths and the green lines indicate the channel width. The arrows indicate specific locations and accumulations of microtubules.

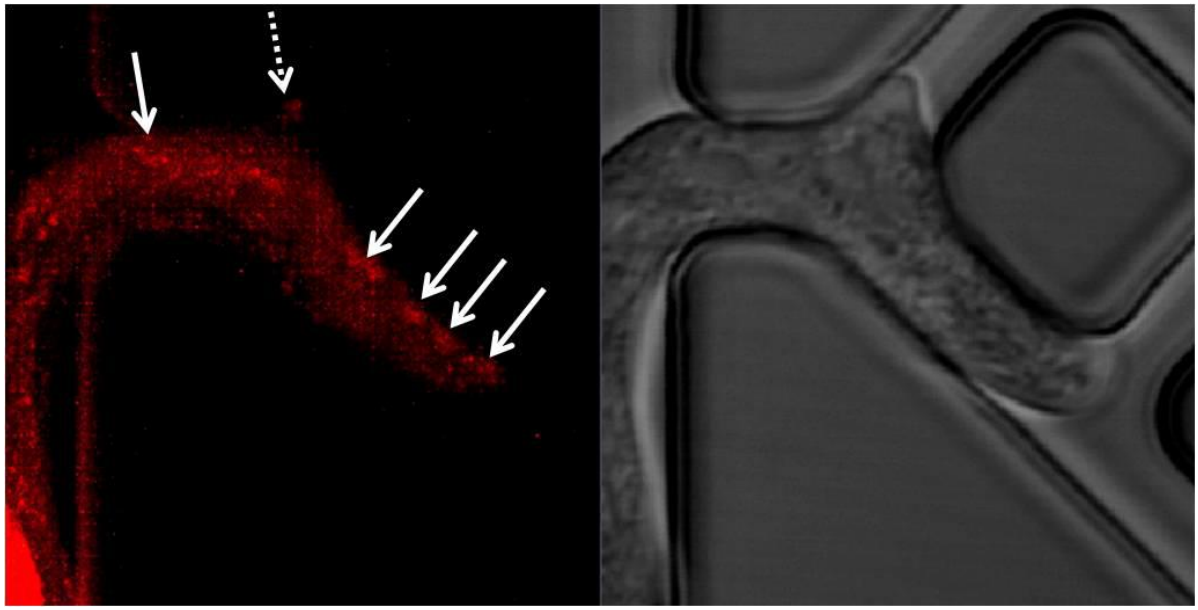

Figure S29. Spitzenkörper mobility and location during branching into channel openings and after bottlenecks. Overlay of the maximum intensities of 121 images of a time series depicting a hypha passing a bottleneck and branching into a channel opening, which was accompanied by the de novo formation of a daughter Spitzenkörper. The images were recorded at intervals of 12.6 s. The parent Spitzenkörper was frequently located close to the confining geometry in the direction closest to the directional memory. The discontinuity appeared to be caused by its motility in the z-direction, which caused it to repeatedly move out of the focal plane. The bright field image represents the hyphal morphology in the last frame of the image series.

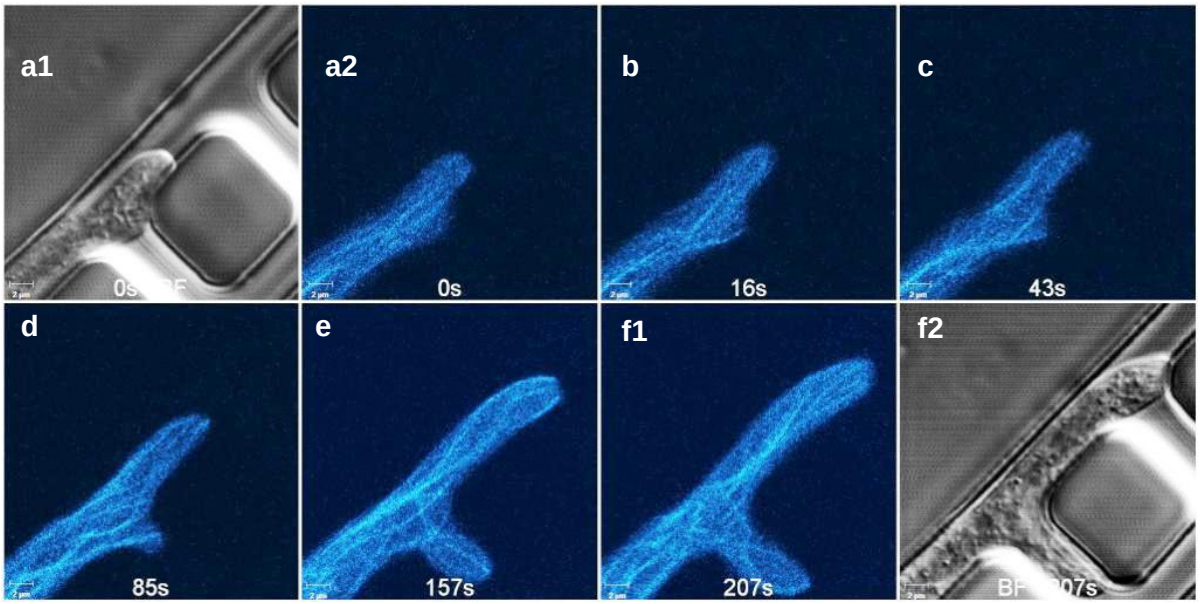

Figure S30. Microtubules in *Neurospora crassa* GFP during branching in a channel with lateral opening. The first and last images represent the simultaneously recorded bright field images of the first and last fluorescence image. The first frame demonstrates the lack of microtubules in the forming bulge. In the following frames, the microtubules penetrated further into the forming daughter branch. Frames a1 and a2, and f1 and f2 represent the same instances.

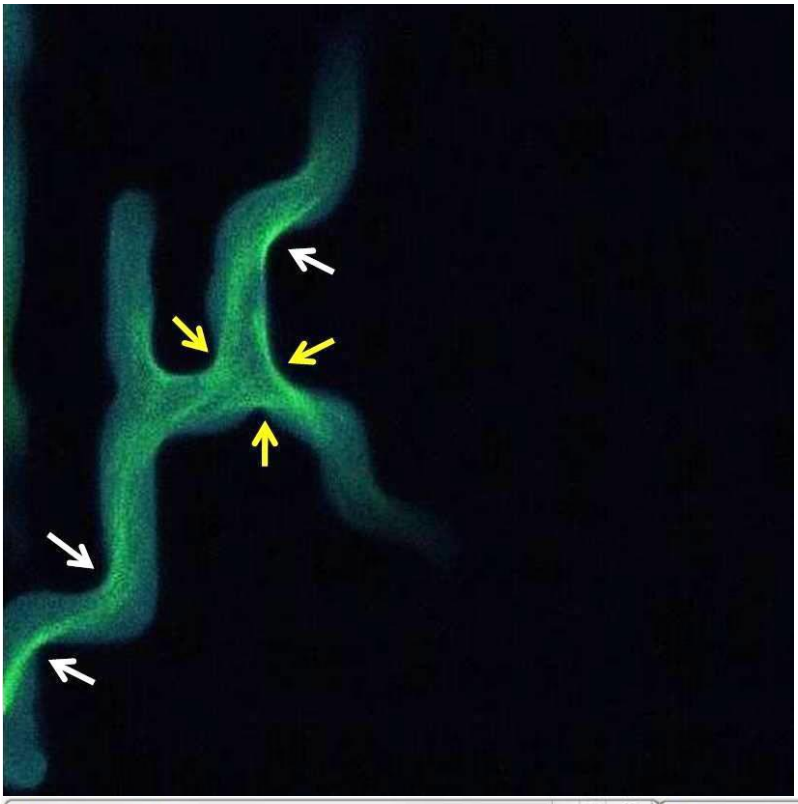

Figure S31. Microtubules in *Neurospora crassa* GFP in meandering channels. The image was created as an average of 51 images in a series recorded at intervals of 15.8 s. The arrows indicate the microtubules that principally aligned along the shortest paths through the hyphae. The yellow arrows indicate a triangle formed by microtubules in the hyphal cross section.

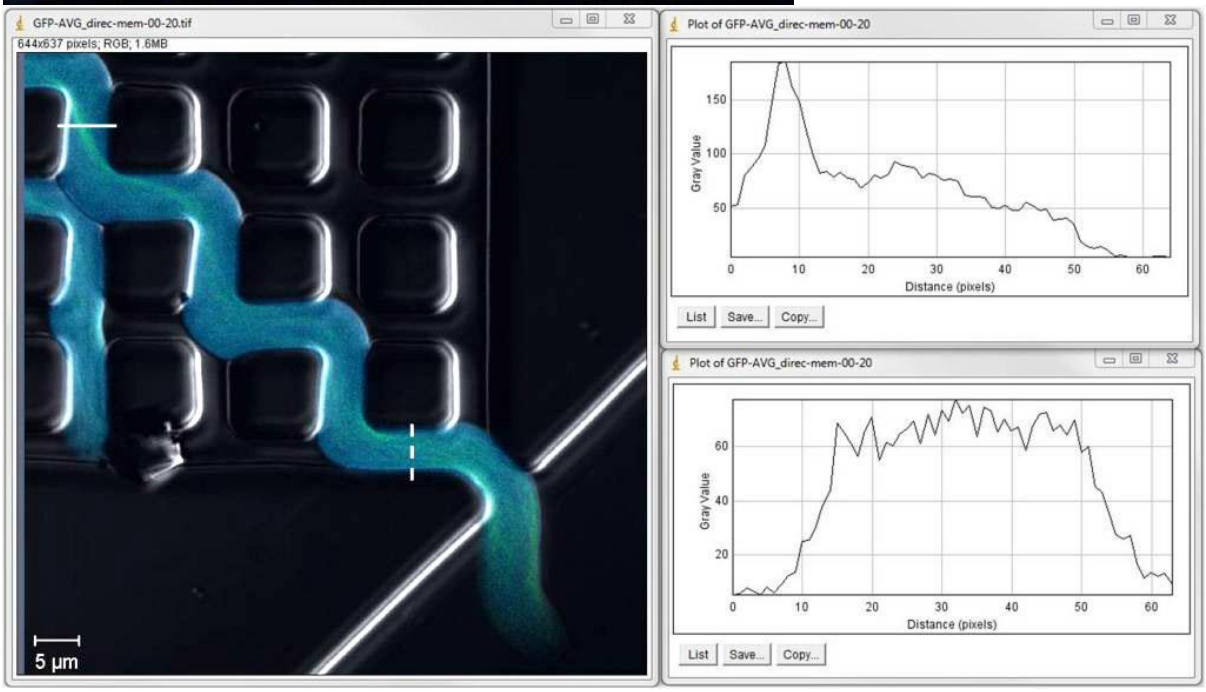

Figure S32. *Neurospora crassa* microtubules through the diamond structure. The average was taken of 21 time-lapse images. The insets represent the intensity profiles taken at the position of the solid white line (top inset) and at the dashed line (bottom inset).

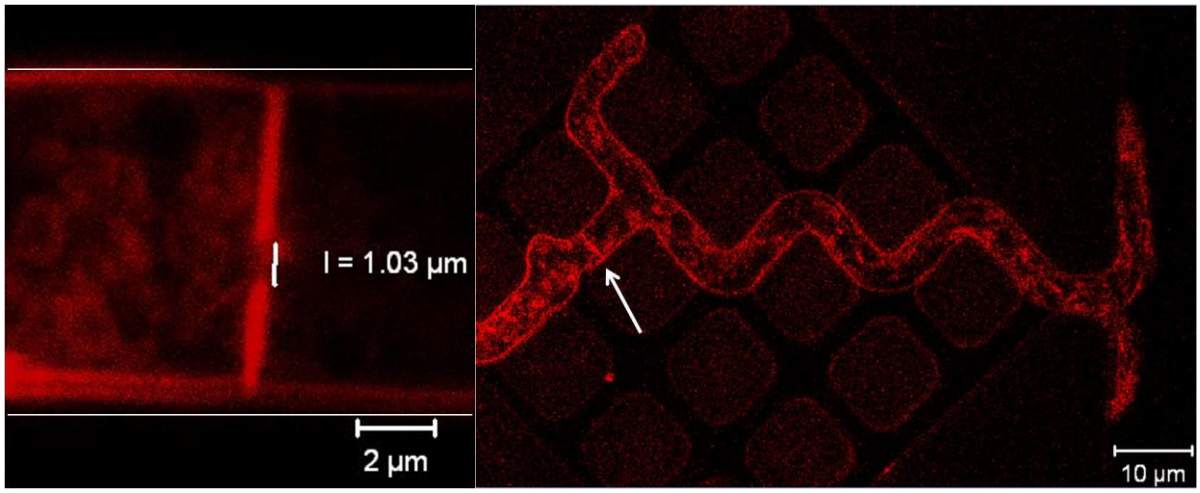

Figure S33. FM4-64 distribution in hyphal trunks confined in channels. Left: Hyphal septum stained with FM4-64 in a hypha confined in a 9 µm wide channel (indicated by white lines). Distribution of the FM4-64 signal in an undulated hyphal trunk in a diamond structure. The white arrow indicates a septum.

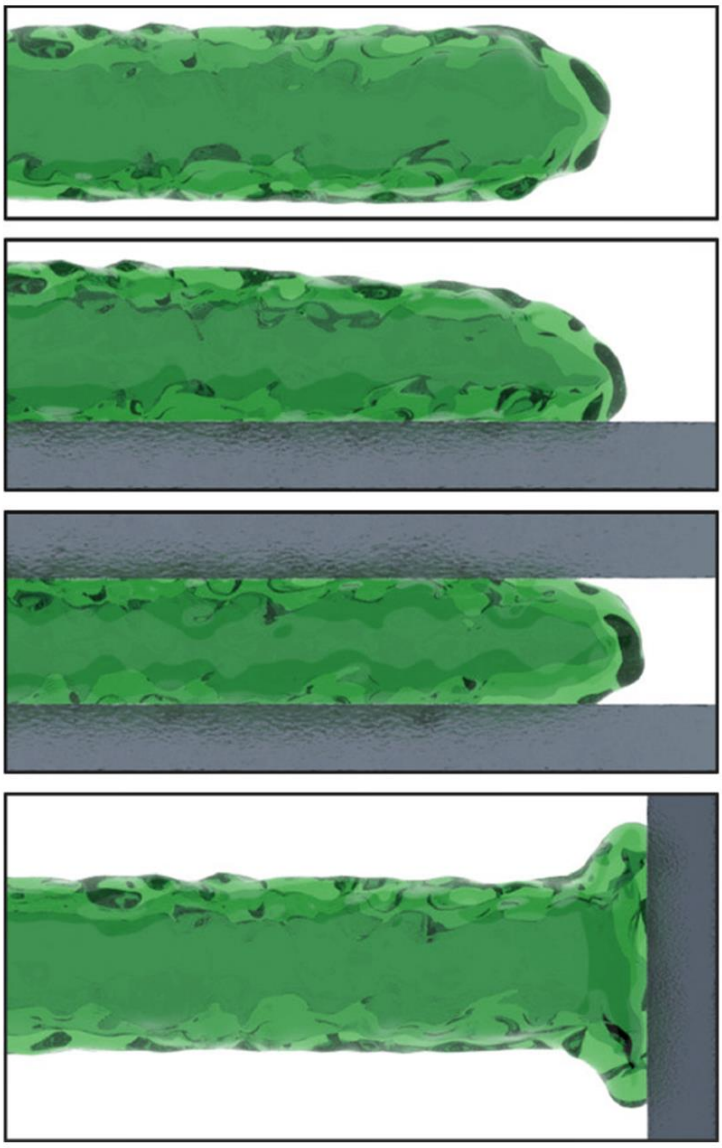

Figure S34. Levels of confinement for fungal growth in PDMS microfluidics structures. (a) *virtually no mechanical confinement:* hyphae with a diameter of 5-7 µm grow in the 10 µm gap between the glass coverslip and the PDMS 'ceiling'), similar to agar; (b) *parallel 1D confinement*: hyphae progress along a wall in the observation plane; (c) *2D confinement:* hyphae grow while being stretched between two walls that are perpendicular to the observation plane, (d) *orthogonal or angled 1D confinement:* hyphae encounter a wall at near-normal incidence.

1.5. Methods

1.5.1. Microfabrication and experimental setup

The microfluidic network is illustrated in Fig. 1 and see SI Appendix, Fig. S1. Its dimensions, i.e., height of 10 µm, and channel widths ranging from 2 to 100 µm were designed to present various level of containment to fungal growth, from tight-constraining in channels with widths smaller than the hyphal diameter, i.e., 5-7 µm, to confined, but non-constraining chambers, with dimensions of 100 x 100 x 10 µm. The artificial environments were fabricated using a two-component polymer, poly(dimethyldisiloxane) (PDMS, Sylgard 184, Dow Corning) using a well-established procedure.(7) Benefits of using PDMS include low fabrication costs, non-toxicity, good biocompatibility, chemical inertness, and optical transparency for wavelengths as low as 280 nm.(8-12) Briefly, the fabrication involved the moulding of a degassed PDMS mixture of the pre-polymer and curing agent (10:1, w/w) onto a microstructured silicon wafer, at 65°C for a duration in excess of 8 hours. After hydrophilization via exposure to UV/ozone, the PDMS stamps were irreversibly fixed onto a microscope cover slip. Lateral openings in the structure allowed the introduction of the growth medium, fungal hyphae, and fluorescent dyes. Fungal inoculation was achieved by placing an agar plug, extracted from a zone with young hyphae, e.g., the peripheral growth zone of a colony, upside down next to a lateral channel opening. The device was then attached to a microscope slide marked with spacers for accurate positioning on a microscope stage. Hyphal confinement within channels ensured that the hyphae remained within the working distance of the microscope objective, while enabling sufficient gas exchange over long periods of time, thus avoiding the need for perfusion with oxygenated nutrient broth, as required in agar.(13, 14)

The microfluidics network design allowed the investigation of fungal behavior in the following scenarios (see SI Appendix Fig. S33, from top to bottom): (a) *virtually no mechanical confinement*, wherein hyphae with a diameter of 5-7 µm grow in the 10 µm gap between the glass coverslip and the PDMS 'ceiling'), similar to agar; (b) *parallel 1D confinement*, wherein hyphae progress along a wall in the observation plane; (c) *2D confinement*, wherein hyphae grow while being constrained between two walls that are perpendicular to the observation plane; and (d) *orthogonal or angled 1D confinement*, wherein hyphae encounter a wall at near-normal incidence. In many instances, the hyphae encounter the wall at a more acute angle (e.g., 45° or less, relative to the surface), which results in a parallel 1D confinement. Additionally, in the case of 2D confinement, the channels can be given various widths and shapes (e.g., straight, zig-zagged, or bent at various angles).

1.5.2. Fungal species, growth media, staining

The *Neurospora crassa rid (RIP4) mat a his-3+::Pccg-1-Bml+sgfp+* mutant strain (henceforth "*Neurospora crassa GFP*"; FGSC #9519) was obtained from the Fungal Genetics Stock Center (School of Biological Sciences, University of Missouri, Kansas City, MO, USA). The *Neurospora crassa GFP* mutant was constructed(15) to express intrinsically GFP-labelled microtubules while maintaining a growth pattern similar to that of the wild type. The strain was cultured on 1% w/v malt extract agar (Merck), which was also used for medium filling the microfluidics structures. The high level of nutrients ensures the cancelling of the possible chemotaxis-driven directionality of growth. Prior to each experiment, the fungal strains were sub-cultured on fresh malt extract agar plates and incubated at 21°C ± 2°C.

The FM4-64 dye (Invitrogen Ltd. (Paisley, UK) was used as a marker for Spitzenkörper(16). A 20-µl droplet of an 8 µM FM4-64 solution was applied onto a microscope coverslip before placing an agar slab, excised from the margin of the growing colony, upside-down onto the droplet. To avoid an overlay of the dynamics of the dye loading and of the Spitzenkörper, imaging was performed at least one hour after loading the hyphae with the dye.

1.5.3. Time-lapse microscopy and image analysis

Live-cell imaging of hyphal growth was performed with an inverted laser-scanning microscope (Zeiss Axio Observer Z1 with LSM 5 Exciter RGB, Carl Zeiss, Göttingen, Germany) with photomultiplier detectors. Samples were excited with 488 nm and 543 nm lasers, and the emitted light was passed through a bandpass filter (505-530 nm) and a 650 nm long-pass filter. To reduce photobleaching and phototoxic effects, the laser intensity and laser scanning time were kept to a minimum (0.7 - 2.4 % laser energy, 0.75- to 23-second frame scans). Fluorescence and bright-field time-lapse images were captured simultaneously and analyzed using image processing software (Zen 2008, Carl Zeiss, Göttingen, Germany). Fiji software(17) was used for image overlay and quantitative image analysis. RETRAC 2.10.0.5 (from Dr. Nick Carter, University of Warwick, UK) was used for frame-by-frame tracking and calculating cytoskeletal and hyphal kinetics.

1.5.4. Growth experiments on agar and microfluidics structures

Control measurements for fungal growth in non-constraining environments were performed on 1% w/v malt extract media using somatic hyphae at the edges of the colony. The leading hyphae, i.e., wide hyphae showing rapid cytoplasmic flow,(18) rarely entered the microfluidic structures and were therefore omitted. For the somatic hyphae, 'subapical compartments' were characterized by an increased nuclear density approximately 60 µm from the extreme apex. Hyphal growth rates were measured by tracking the position of the extreme hyphal apices in subsequent frames. Fungal growth was recorded for the period needed to observe hyphal behavior from the entry in, to the exit from the microfluidics network of interest, which require approximately 20 minutes for a straight 100 µm channel. However, due to the more convoluted geometries of some microfluidics structures, and the presence of multiple hyphae, in many instances the image recording lasted more than one hour.

To measure the cytoskeletal alignment within hyphae, tangents were fitted manually to microtubules, and the respective local hyphal longitudinal (i.e., polarization) axes and intersection angles were measured. To measure the rates of microtubule polymerization within the apical compartment, and to distinguish this from motility, the positions of individual filament ends were tracked frame-by-frame, following a methodology reported previously.(19)

The parameters of the obstacle-induced apical 'hit & split' included the time elapsed from the impact to the establishment of the daughter hyphae and the maximum size of the formed bulges immediately before the re-establishment of polarized growth. The hyphal diameter was measured at the time of collision with the obstacle. The maximum bulge size was measured by overlaying the frame of collision with the frame in which the growth pattern of the daughter bulges changed to polarized extension and determining the difference in the apical cell wall location on both sides of the hypha.

1.5.5. Statistical analysis

Statistica 7.1 (Statsoft Inc., OK, USA) and GraphPad Prism 6.01 (GraphPad Software Inc., CA, USA) were used for statistical analysis and correlation tests. Statistical analyses included calculating the mean and standard deviation values of parameters measured, i.e., position, alignment with the hyphal axis, polymerization rate for microtubules, times before reappearance of the Spitzenkörper, and hyphal bulge dimensions, over the total number *n* data points, reported for each instance. Statistical analyses included all accumulated data from at least 20 separate experiments (unless otherwise stated). GraphPad prism was used to perform a Mann-Whitney test comparing the apical and subapical distributions of the microtubule polymerization rates and the microtubule alignments to the polarization axis respectively.

1.6. References for Supplementary Information

1. Adams PA, Sheppard JG, Ridler GM, Ridler PF. New three-parameter empirical extension of the arrhenius equation suitable for the precise evaluation of pseudo-thermodynamic activation parameters in chemical kinetics. Journal of the Chemical Society, Faraday Transactions 1: Physical Chemistry in Condensed Phases. 1978;74.
2. Merkel TC, Bondar VI, Nagai K, Freeman BD, Pinnau I. Gas sorption, diffusion, and permeation in poly(dimethylsiloxane). Journal of Polymer Science Part B: Polymer Physics. 2000;38(3):415-34.
3. Motawia MS, Damager I, Olsen CE, Møller BL, Engelsen SB, Hansen S, et al. Comparative Study of Small Linear and Branched α-Glucans Using Size Exclusion Chromatography and Static and Dynamic Light Scattering#. Biomacromolecules. 2005;6(1):143-51.
4. Hulst AC, Hens HJH, Buitelaar RM, Tramper J. Determination of the effective diffusion coefficient of oxygen in gel materials in relation to gel concentration. Biotechnology Techniques. 1989;3(3):199-204.
5. Warin F, Gekas V, Voirin A, Dejmek P. Sugar diffusivity in agar gel/milk bilayer systems. Journal of Food Science. 1997;62(3):454-6.
6. Merkel TC, Bondar VI, Nagai K, Freeman BD, Pinnau I. Gas sorption, diffusion, and permeation in poly(dimethylsiloxane). Journal of Polymer Science, Part B: Polymer Physics. 2000;38(3):415-34.
7. Held M, Edwards C, Nicolau DV. Probing the growth dynamics of Neurospora crassa with microfluidic structures. Fungal Biology. 2011;115(6):493-505.
8. Desai TA. Micro- and nanoscale structures for tissue engineering constructs. Medical Engineering and Physics. 2000;22:595-606.
9. DiLuzio WR, Turner L, Mayer M, Garstecki P, Weibel DB, Berg HC, et al. Escherichia coli swim on the right-hand side. Nature. 2005;435:1271-4.
10. Mondal S, Ahlawat S, Rau K, Venkataraman V, Koushika SP. Imaging in vivo Neuronal Transport in Genetic Model Organisms Using Microfluidic Devices. Traffic. 2011;12(4):372-85.
11. Park S, Wolanin PM, Yuzbashyan EA, Lin H, Darnton NC, Stock JB, et al. From the Cover: Influence of topology on bacterial social interaction. Proceedings of the National Academy of Sciences. 2003;100(24):13910-5.
12. Kim HJ, Huh D, Hamilton G, Ingber DE. Human gut-on-a-chip inhabited by microbial flora that experiences intestinal peristalsis-like motions and flow. Lab on a Chip. 2012;12(12):2165-74.
13. Löpez-Franco R, Bracker C. Diversity and dynamics of the Spitzenkörper in growing hyphal tips of higher fungi. Protoplasma. 1996;195(1-4):90-111.
14. Riquelme M, Bartnicki-Garcia S. Key differences between lateral and apical branching in hyphae of Neurospora crassa. Fungal Genetics and Biology. 2004;41(9):842-51.
15. Freitag M, Hickey PC, Raju NB, Selker EU, Read ND. GFP as a tool to analyze the organization, dynamics and function of nuclei and microtubules in Neurospora crassa. Fungal Genetics and Biology. 2004;41(10):897-910.
16. Araujo-Palomares CL, Riquelme M, Castro-Longoria E. The polarisome component SPA-2 localizes at the apex of Neurospora crassa and partially colocalizes with the Spitzenkörper. Fungal Genetics and Biology. 2009;46(8):551-63.
17. Schindelin J, Arganda-Carreras I, Frise E, Kaynig V, Longair M, Pietzsch T, et al. Fiji: An open-source platform for biological-image analysis. Nature Methods. 2012;9(7):676-82.
18. Steele GC, Trinci APJ. Morphology and Growth Kinetics of Hyphae of Differentiated and Undifferentiated Mycelia of Neurospora crassa. Journal of General Microbiology. 1975;91(2):362-8.
19. Uchida M, Mouriño-Pérez RR, Freitag M, Bartnicki-García S, Roberson RW. Microtubule dynamics and the role of molecular motors in Neurospora crassa. Fungal Genetics and Biology. 2008;45(5):683-92.

2. SUPPLEMENTARY MOVIES

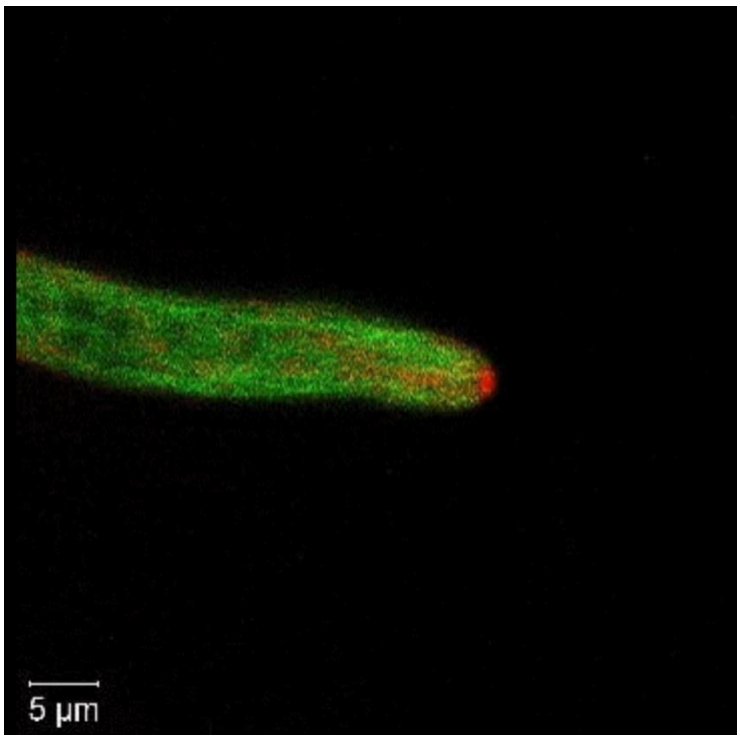

Supporting Information Movie S1. Unconstrained hyphal growth in a wide, 100x100x10 µm PDMS-made chamber. The microtubules were genetically GFP-tagged (pseudo-coloured green), and the hypha was loaded with the marker dye FM4-64 (pseudo-coloured red) labelling the Spitzenkörper as a bright red object within the extreme hyphal apex. The video shows that the Spitzenkörper maintains a central position with temporary side-ways deviations resulting in small changes in the growth direction. Frame rate = 12.6 s per frame.

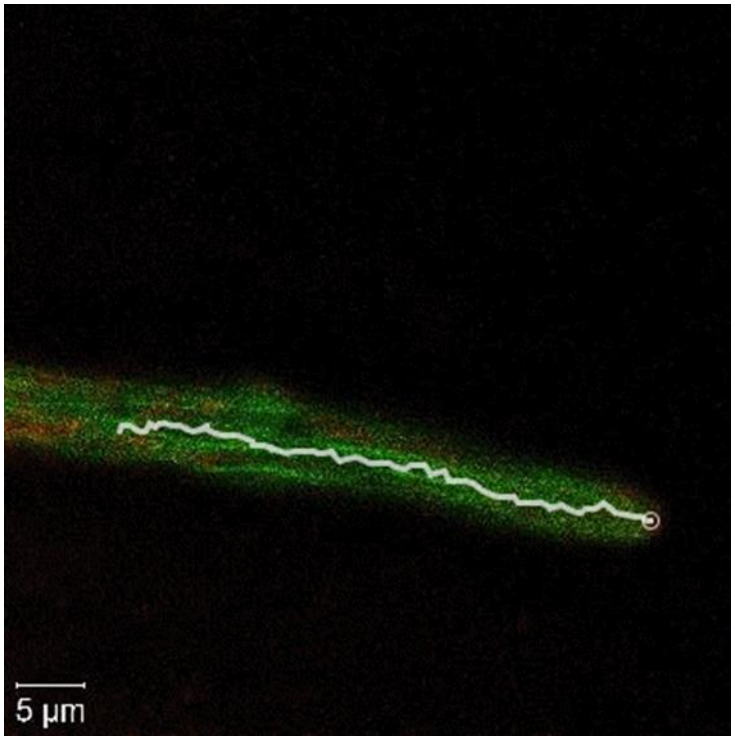

Supporting Information Movie S2: The same hypha as in S1, with tracking of the Spitzenkörper trajectory.

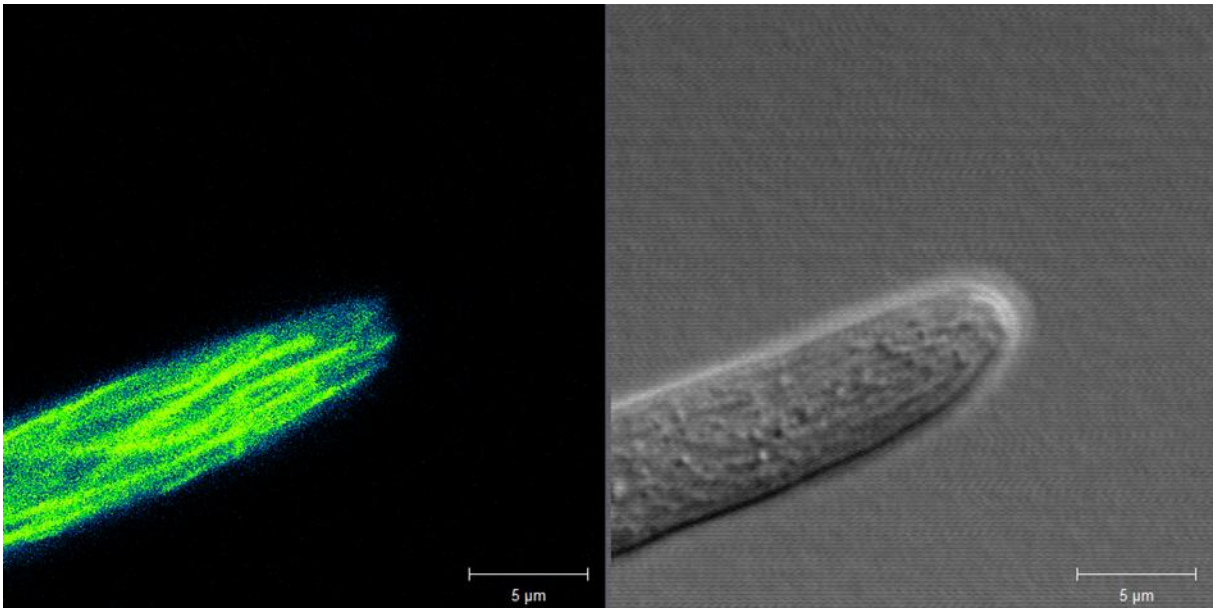

Supplementary Information Movie S3. Hyphal growth on an open agar surface, displaying the microtubules (green, left) and vesicle traffic (phase-contrast image, right).

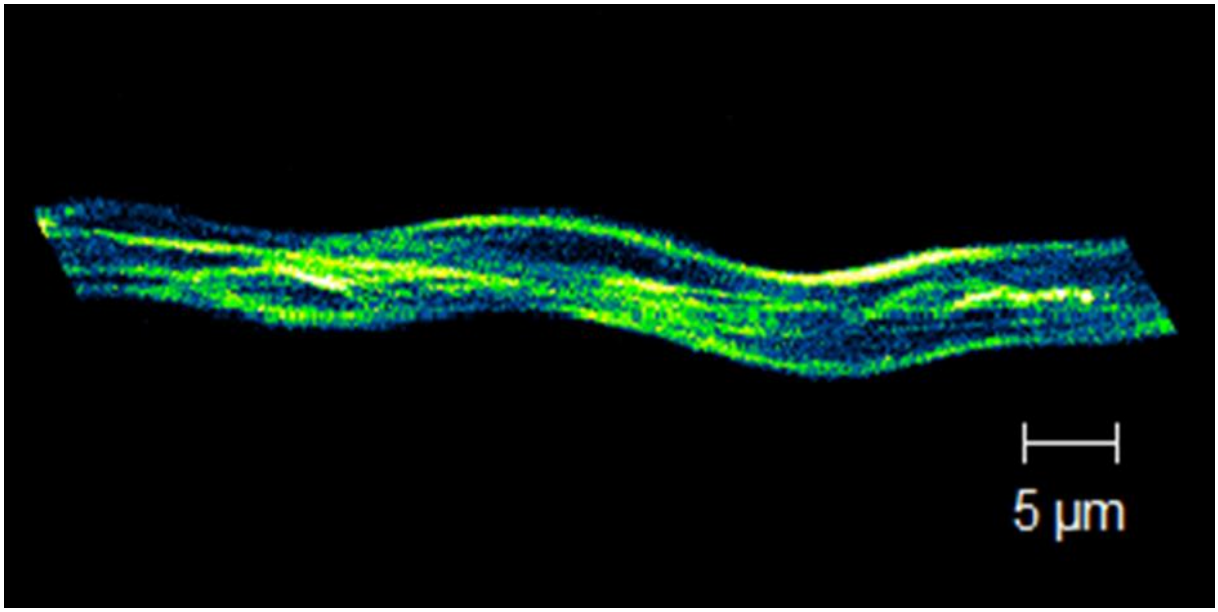

Supporting Information Movie S4: Microtubule distribution along a hypha growing in an unconfined environment.

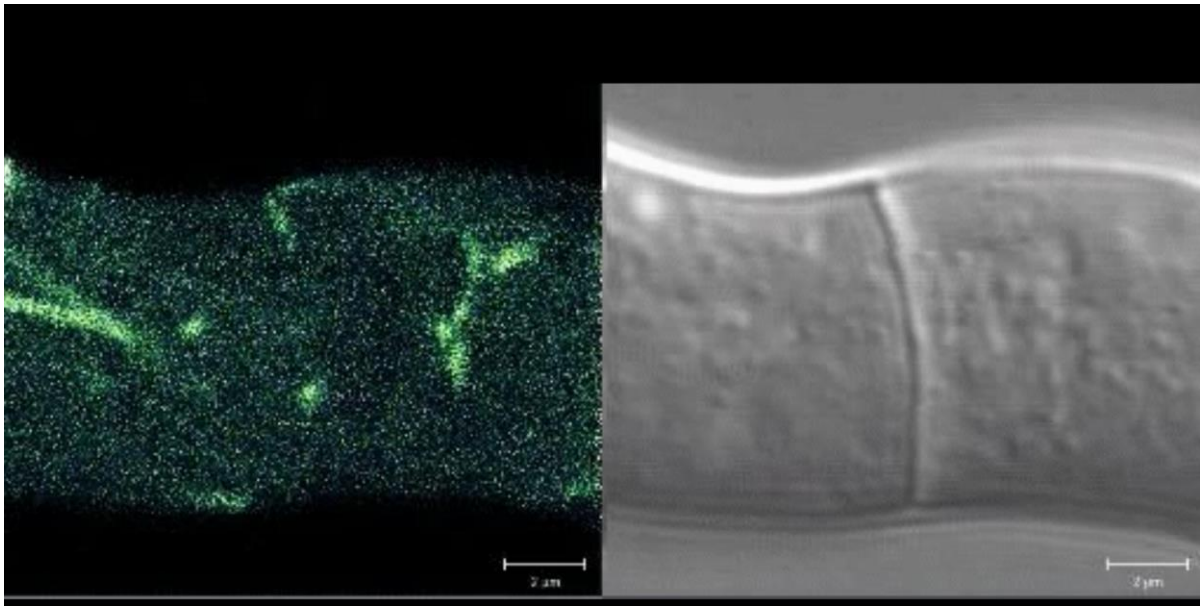

Supplementary Information Movie S5. Microtubule dynamics when passing a septum. Left: fluorescence imaging. Right: bright field imaging.

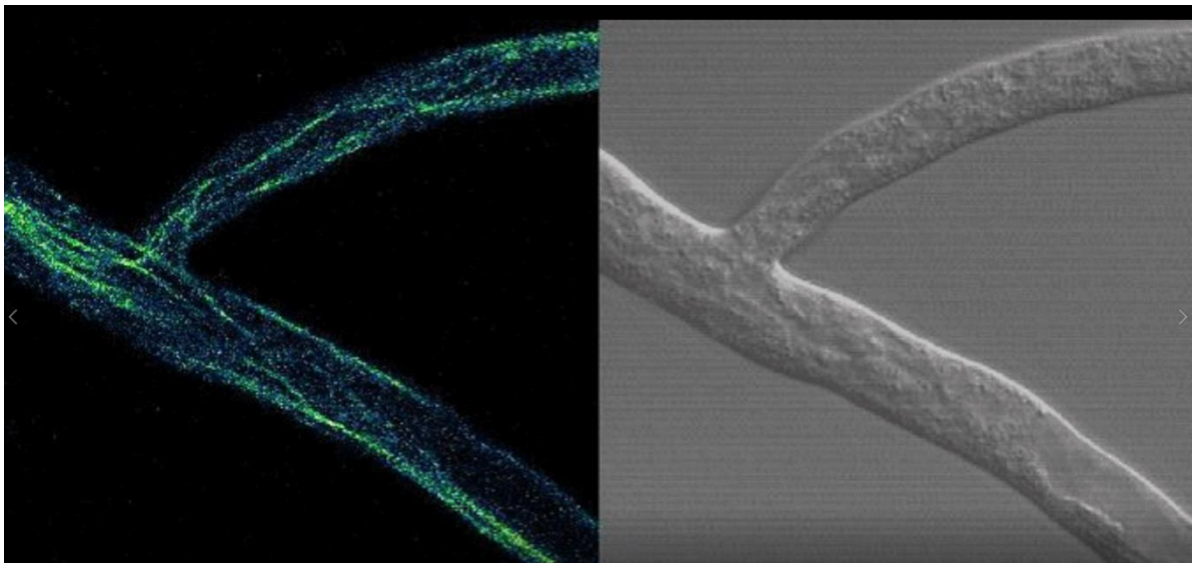

Supporting Information Movie S6: Microtubule dynamics during lateral branching on agar.

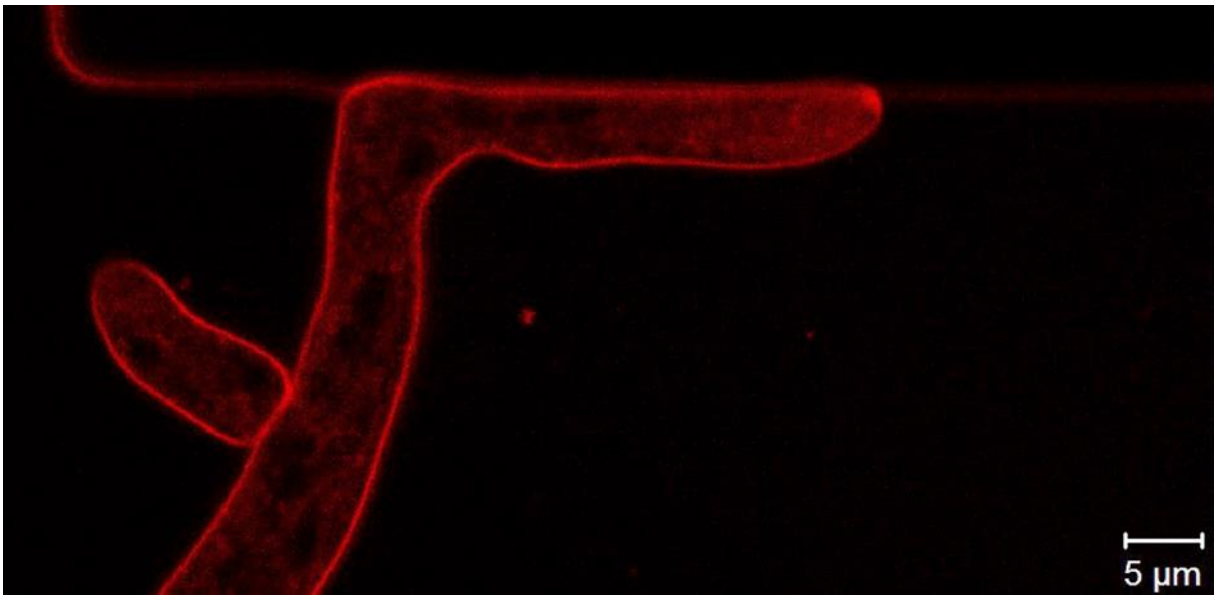

Supporting Information Movie S7. Directional memory, illustrated with a *Neurospora crassa* hypha loaded with the marker dye FM4-64 (pseudo-coloured red). The hypha initially encounters a wall at a steep angle and temporarily redirects its growth direction according to the constraining geometry. During the 'nestling' phase, the Spitzenkörper shifts from the apex centre toward the wall, and the apex shape becomes skewed also toward the wall. Upon reaching the corner, the hypha immediately recovers its initial growth direction. Frame rate = 17.9 s per frame; total real-time sequence duration = 20 min 44 s.

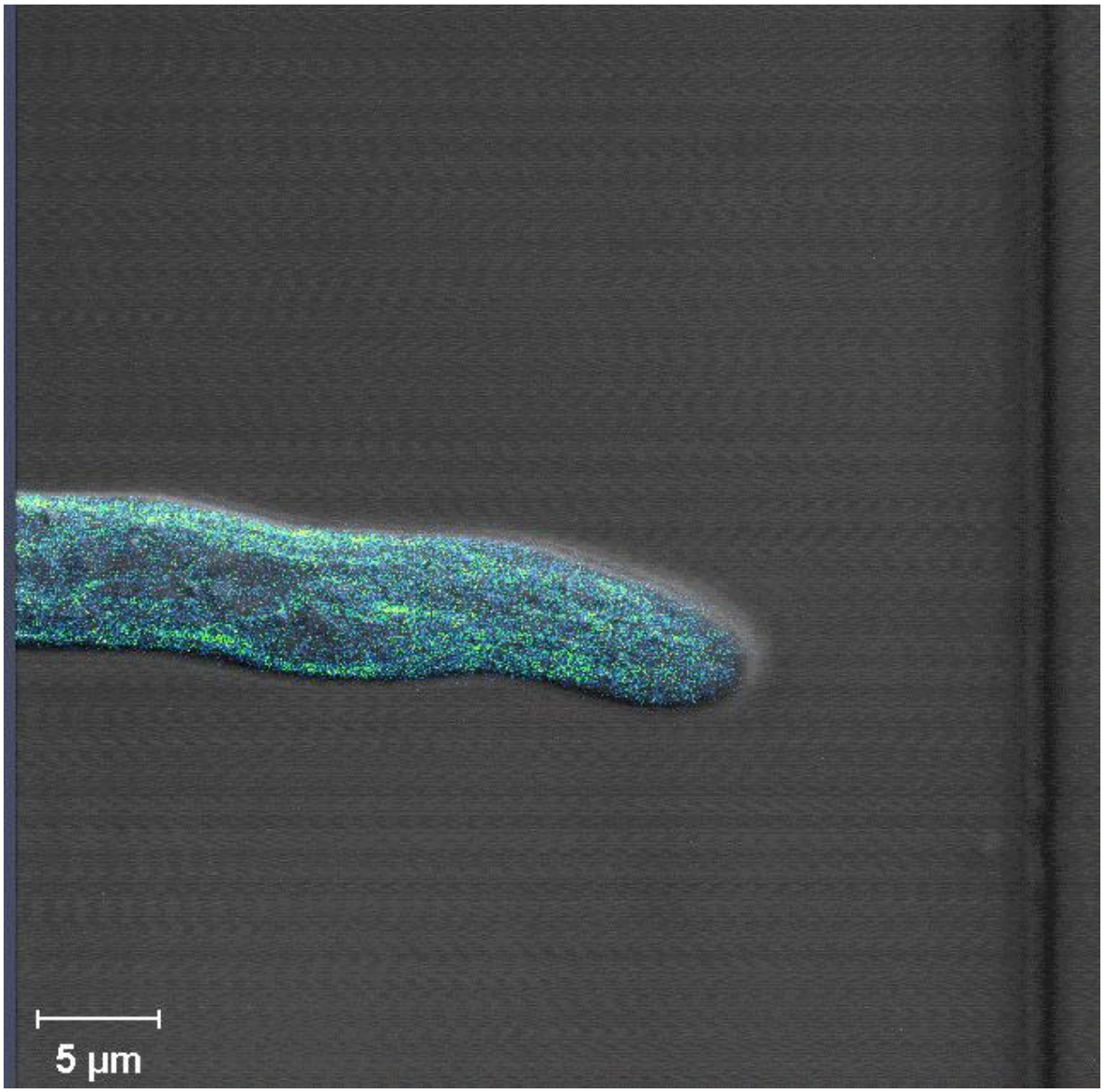

Supplementary Information Movie S8. Encounter of a hypha with a PDMS wall, followed by splitting into two daughter hyphae. After formation the two twin hyphae return to their parent directional memory and penetrate the soft PDMS wall.

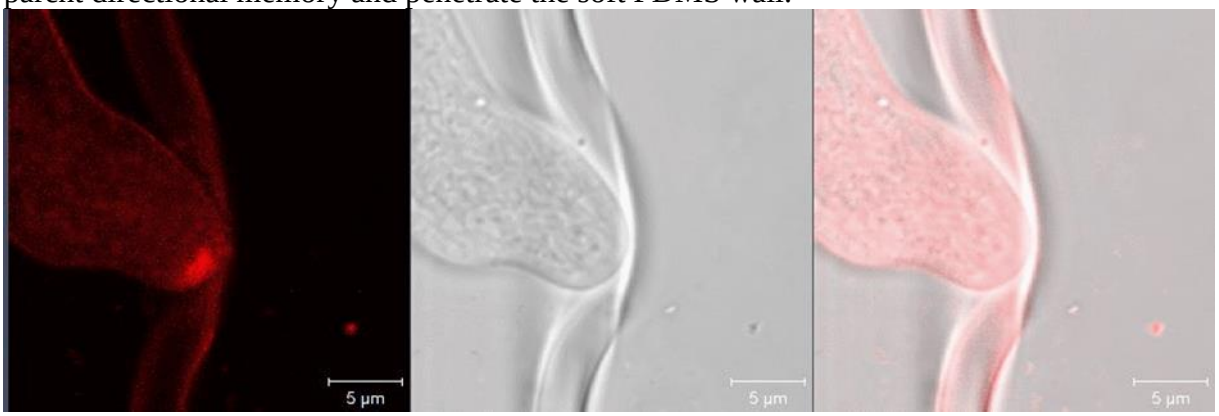

Supplementary Information Movie S9. Encounter of a hypha with a soft PDMS wall, followed by penetration. The Spitzenkörper disappears as the hypha tip exerts pressure on the PDMS wall, similarly with initial stages of the 'hit and split' process (Movie S8).

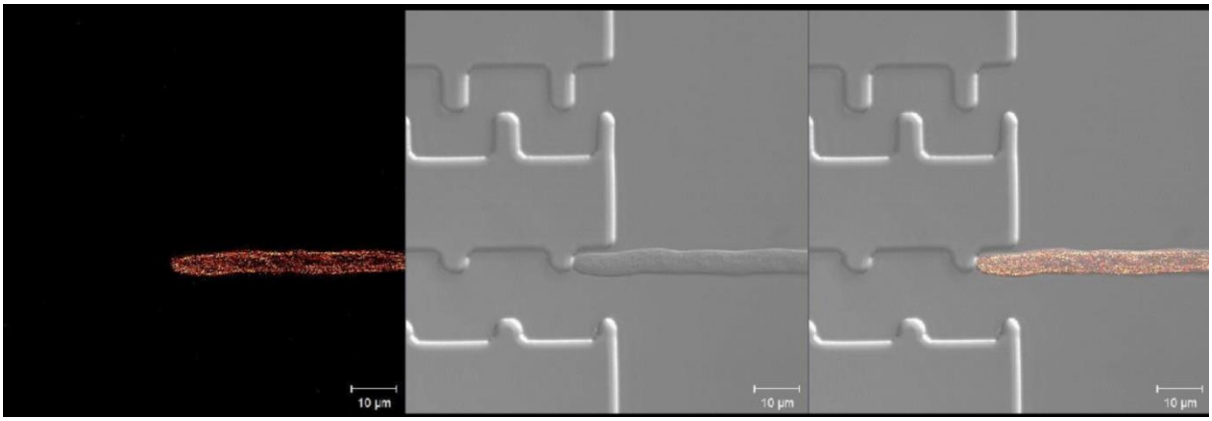

Supplementary Information Movie S10. Microtubule dynamics in a *Neurospora crassa* hypha growing through a string of lateral obstacles. Left: fluorescently labelled microtubules. Middle: differential contrast imaging of the hyphal growth. Right: overlap of the fluorescent and bright field images.

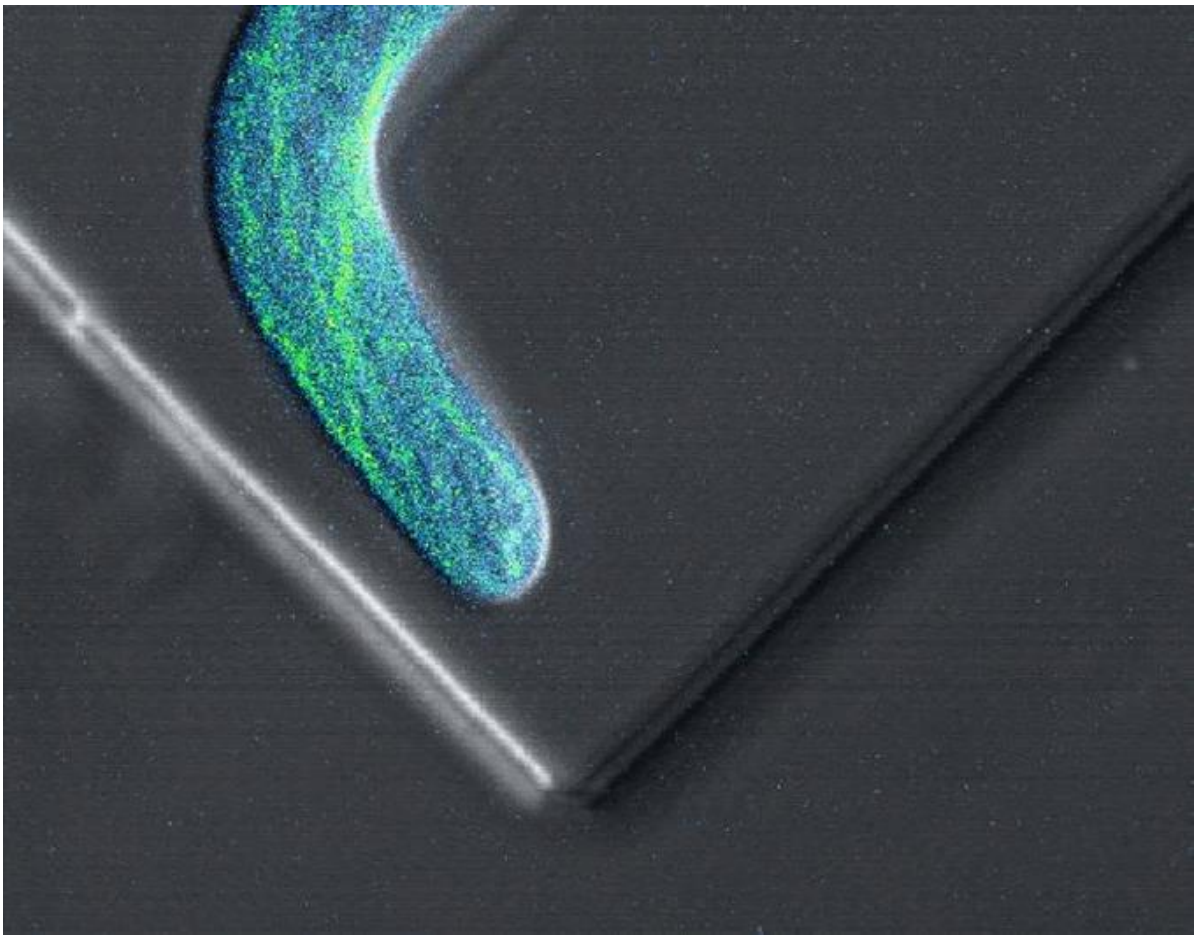

Supplementary Information Movie S11. Encounter of a hypha with a corner (microtubules labelled green). The directional memory opposes a change in growth direction; instead, an orthogonal branch emerges near the apex of the parent hypha.

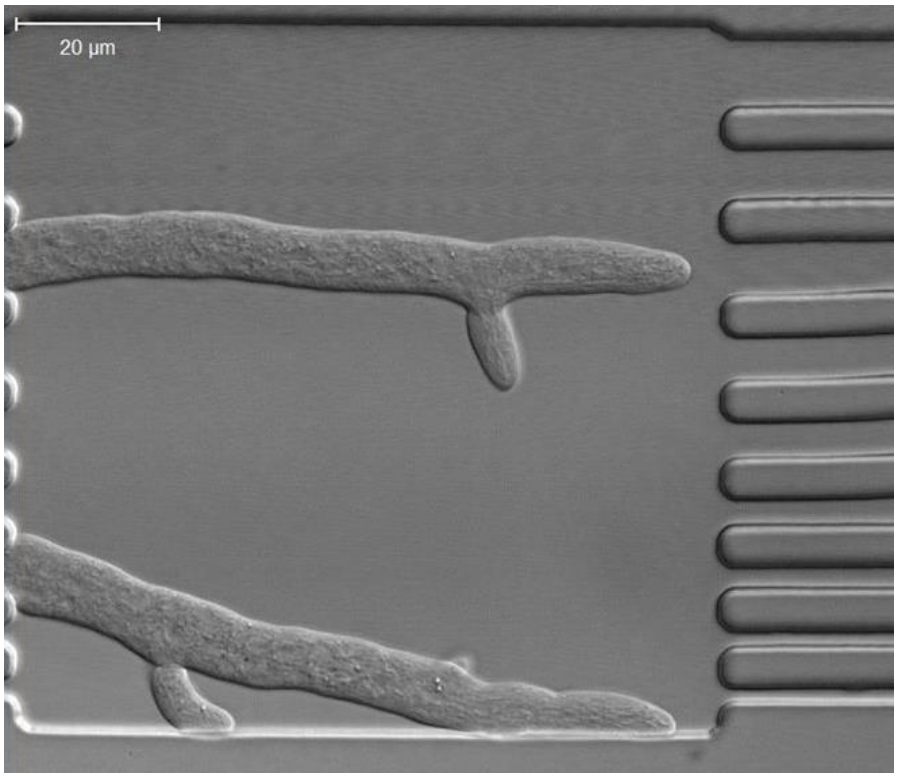

Supplementary Information Movie S12. Hyphae tightly-constrained in narrow channels. The absence of lateral openings precludes lateral branching, but branching resumes immediately upon leaving the channel.

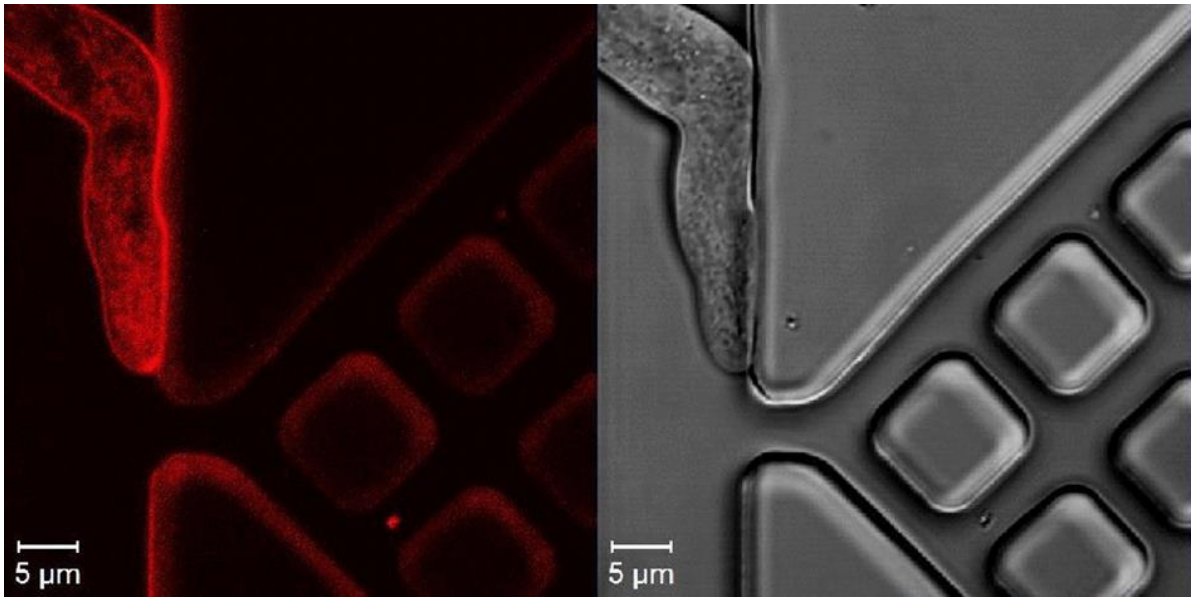

Supplementary Information Movie S13. Lateral branching of a *Neurospora crassa* hypha at a channel intersection, imaged with the fluorescent marker dye FM4-64 (left, pseudo-coloured red) and by bright-field imaging. The growth of the parent hypha is temporarily deflected by the vertical wall, but it subsequently realigns in a direction similar to that before the initial wall encounter (top left corner of the images). During this growth, the expanding subapical hyphal diameter eventually exceeds the channel width at the first intersection. The cell wall bulges, and the formation of a daughter Spitzenkörper precedes the establishment of an independent lateral daughter branch. The effect of directional memory is apparent in the movement of the primary hypha. Frame rate = 17.6 s per frame; total real-time duration 14 min 23 s.

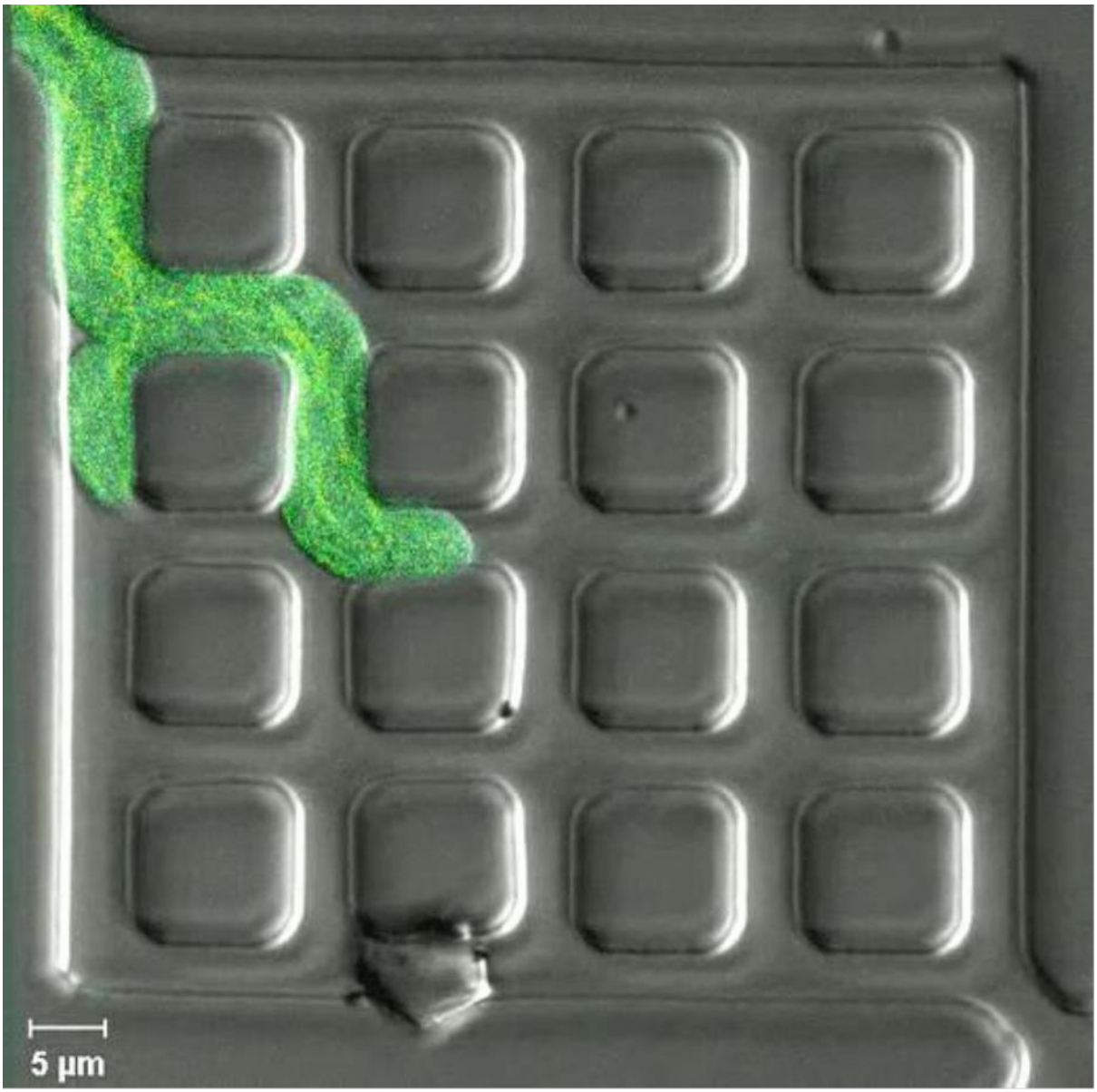

Supplementary Information Movie S14. Directional memory, displayed in the conservation of hyphal microtubule orientations throughout a 150-µm path.

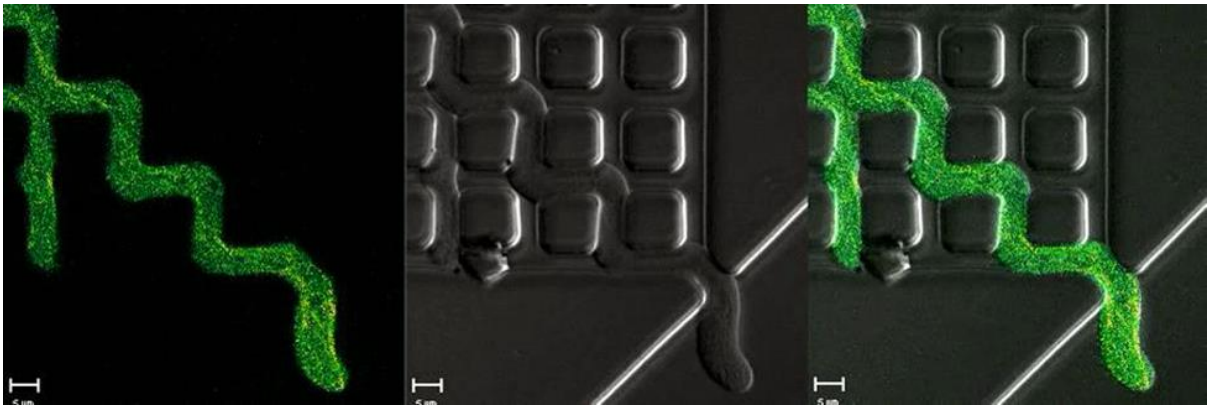

Supplementary Information Movie S15. The same sequence of events as in Movie S9 showing the microtubules only (green, left), a phase-contrast image (middle), and an overlay of the two imaging modes (right).